Journal of Molecular Cell Biology (2022), 14(11), mjac064 https://doi.org/10.1093/jmcb/mjac064
Published online December 2, 2022

Article

Decellularized extracellular matrix as scaffold for cancer organoid cultures of colorectal peritoneal metastases

Luca Varinelli[1,†], Marcello Guaglio[2,†], Silvia Brich[3,†], Susanna Zanutto[1], Antonino Belfiore[3], Federica Zanardi[4], Fabio Iannelli[4], Amanda Oldani[5], Elisa Costa[5], Matteo Chighizola[6], Ewelina Lorenc[6], Simone P. Minardi[7], Stefano Fortuzzi[7], Martina Filugelli[8], Giovanna Garzone[8], Federica Pisati[7], Manuela Vecchi[7], Giancarlo Pruneri[3], Shigeki Kusamura[2], Dario Baratti[2], Laura Cattaneo[8], Dario Parazzoli[5], Alessandro Podestà[6], Massimo Milione[8], Marcello Deraco[2], Marco A. Pierotti[7], and Manuela Gariboldi[1,*]

[1] Department of Research, Fondazione IRCCS Istituto Nazionale dei Tumori, via G. Venezian 1, 20133 Milan, Italy
[2] Peritoneal Surface Malignancies Unit, Colon and Rectal Surgery, Fondazione IRCCS Istituto Nazionale dei Tumori, via G. Venezian 1, 20133 Milan, Italy
[3] Department of Pathology and Laboratory Medicine, Clinical Research lABoratory (CRAB), Fondazione IRCCS Istituto Nazionale dei Tumori, via G. Venezian 1, 20133 Milan, Italy
[4] Bioinformatics Core Unit, IFOM ETS, The AIRC Institute of Molecular Oncology, via Adamello 16, 20139 Milan, Italy
[5] Imaging Technological Development Unit, IFOM ETS, The AIRC Institute of Molecular Oncology, via Adamello 16, 20139 Milan, Italy
[6] C.I.Ma.I.Na. and Dipartimento di Fisica 'Aldo Pontremoli', Università degli Studi di Milano, via G. Celoria 16, 20133 Milan, Italy
[7] Cogentech Ltd Benefit Corporation with a Sole Shareholder, via Adamello 16, 20139 Milan, Italy
[8] Pathology and Laboratory Medicine Department, Fondazione IRCCS Istituto Nazionale dei Tumori, via G. Venezian 1, 20133 Milan, Italy
[†] These authors contributed equally to this work.
* Correspondence to: Manuela Gariboldi, E-mail: manuela.gariboldi@istitutotumori.mi.it

Edited by Xuebiao Yao

Peritoneal metastases (PM) from colorectal cancer (CRC) are associated with poor survival. The extracellular matrix (ECM) plays a fundamental role in modulating the homing of CRC metastases to the peritoneum. The mechanisms underlying the interactions between metastatic cells and the ECM, however, remain poorly understood, and the number of *in vitro* models available for the study of the peritoneal metastatic process is limited. Here, we show that decellularized ECM of the peritoneal cavity allows the growth of organoids obtained from PM, favoring the development of three-dimensional (3D) nodules that maintain the characteristics of *in vivo* PM. Organoids preferentially grow on scaffolds obtained from neoplastic peritoneum, which are characterized by greater stiffness than normal scaffolds. A gene expression analysis of organoids grown on different substrates reflected faithfully the clinical and biological characteristics of the organoids. An impact of the ECM on the response to standard chemotherapy treatment for PM was also observed. The *ex vivo* 3D model, obtained by combining patient-derived decellularized ECM with organoids to mimic the metastatic niche, could be an innovative tool to develop new therapeutic strategies in a biologically relevant context to personalize treatments.

Keywords: colorectal cancer, peritoneal metastasis, organoids, extracellular matrix (ECM), decellularized extracellular matrix, engineered disease model, ECM stiffness

Received February 28, 2022. Revised August 31, 2022. Accepted November 30, 2022.

Introduction

The peritoneum is the second most common site of metastasis for colorectal cancer (CRC) after the liver (Herszeny and Tulassay, 2010). In the past, peritoneal metastases (PM) were considered a terminal condition, amenable only to palliative treatments. The advent of cytoreductive surgery (CRS) and hyperthermic intraperitoneal chemotherapy (HIPEC) in the 1990s have allowed some patients with PM to achieve long-term survival, pushing the median overall survival from 16 to 51 months (Baratti et al., 2015). However, ∼70% of treated patients still experience peritoneal relapse (Yan et al., 2006). The development of preclinical cellular models that faithfully recapitulate PM pathology, therefore, is crucial for the identification of more effective therapeutic strategies.

The peritoneal metastatic cascade consists of a series of steps that begin with cell detachment from the primary tumor (Jayne, 2007). Fine-tuned interactions between biochemical factors and biomechanical events, such as remodeling of the extracellular matrix (ECM), govern the cascade and allow the formation of the metastatic niche (Ksiazek et al., 2010; Lemoine et al., 2016; Peinado et al., 2017; Mikula-Pietrasik et al., 2018). The metastatic niche facilitates organotrophic metastasis through the direct promotion of cancer stem cell survival, exploiting a tissue-specific microenvironment that is more suitable for the attachment of exfoliated neoplastic cells (Lemoine et al., 2016). The biology behind these processes, however, is poorly understood due to the lack of organ-specific experimental models.

Most of the current data on metastatic spread have been obtained using cancer cell lines or patient-derived xenograft models, which do not fully reflect the physiopathology of their tumor of origin (Drost and Clevers, 2018). Tumor-derived organoids (TDO) are an intermediate model between cell lines and xenografts. They grow three-dimensionally and retain cell–cell and cell–matrix interactions, which more closely reflect the characteristics of the original tumor. Importantly, organoids can be established in a short time and are easy to manipulate (Fujii et al., 2016), and they retain the genetic status of the original tissues and can be used to identify new therapeutic targets (Bozzi et al., 2017).

The possibility to isolate natural decellularized ECMs (dECMs) while preserving both three-dimensional (3D) tissue architecture and biochemical properties, enabling the development of more physiological cancer models (Genovese et al., 2014; Chen et al., 2016), prompted us to develop a tissue-engineered PM model for *in vitro* studies. Our model is based on seeding PM-derived organoids onto decellularized peritoneum-derived ECMs. By being able to characterize the biochemical and biophysical properties of both organoids and ECM, the developed PM model allowed us to study the complex interactions between the ECM and neoplastic cells, gaining new insights into PM biology and the mechanisms underlying cell–microenvironment interaction in this system.

Results

Development of PM-derived organoids

Six organoid cultures (C1–C6) were developed from PM, following established protocols (Fujii et al., 2015, 2016), as detailed in the Materials and methods section. The main characteristics of the patients from which the organoids were derived are summarized in Supplementary Table S1. In line with previous works on organoids from advanced CRC (Fujii et al., 2015, 2016), the growth of the organoids required the supplementation of minimal niche factors. Organoids carrying mutations in the *KRAS* gene mainly required noggin-1 supplementation, while organoids carrying *FGR1* amplification grew in the medium with epidermal growth factor (EGF). *BRAF*-mutant TDO grew in the medium with minimal requirements for niche factors. These results highlight how different mutational profiles drive specific niche factor requirements (Supplementary Table S2; Fujii et al., 2016).

PM-derived organoid characterization

PM-derived organoids retained the main characteristics of their tissues of origin, expressing the colorectal-specific markers CK AE1/AE3, CK20, CK19, and CDX2 in the same percentage of cells as the tissue from which they originated (Figure 1A and B; Supplementary Figure S1A, C, and E). The TDO exhibited the typical glandular features observed in the corresponding surgical sample, including signet ring cells, nest-like growth pattern, nuclear atypia, cuboidal nuclear morphology, and pleomorphism (Figure 1A and C).

All organoids and corresponding clinical samples were positive for LGR5, a well-established stem cell marker for the colonic niche (Figure 1D; Supplementary Figure S1B and D; Bozzi et al., 2017). The percentage of LGR5^{+} cells was similar to that of their tissue of origin (Figure 1E; Supplementary Figure S1F). The organoids were also Ki-67^{+}, suggesting that they underwent active proliferation (Figure 1A; Supplementary Figure S1A and C). Moreover, the TDO mutational profiles were very similar to those of the tumor of origin (Figure 1F; Supplementary Figure S1G).

Development of 3D-dECMs

3D-dECMs from PM and normal peritoneum were generated following the protocol described by Genovese et al. (2014). DNA quantification showed almost complete DNA depletion after the decellularization procedure (***$P < 0.001$; Figure 2A; Supplementary Figure S2A). Fluorescence analysis of formalin-fixed paraffin-embedded (FFPE) sections highlighted the complete removal of the nuclei and lipids from the cellular membranes (Figure 2B). Immunohistochemistry (IHC) analysis showed the loss of cytokeratins and vimentin, indicating the absence of epithelial and mesenchymal cells, respectively (Figure 2C). IHC analysis also showed the retained distribution of collagen-IV, which is the main structural protein (Figure 2C). hematoxylin and eosin (H&E), van Gienson, Masson trichrome, and Alcian–PAS

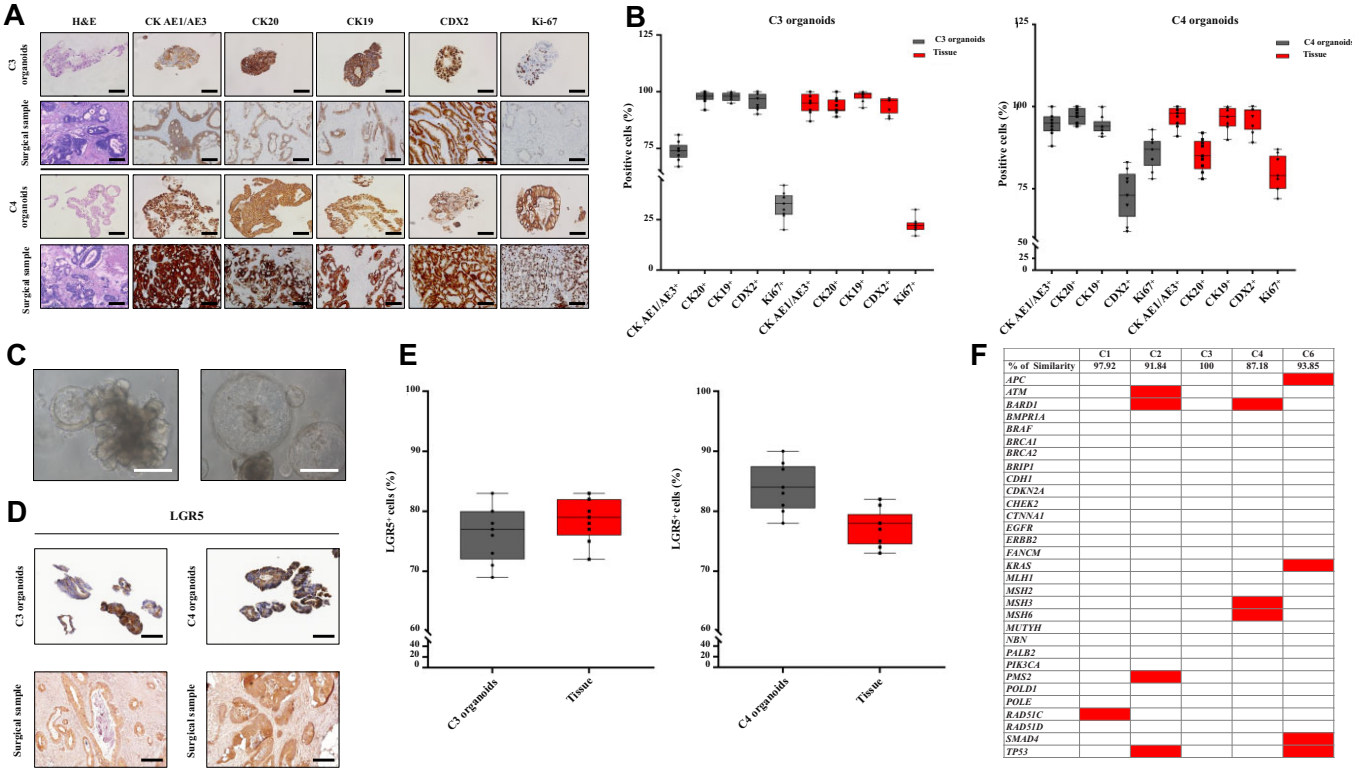

Figure 1 Establishment and characterization of human PM-derived organoids. (**A**) Comparative histochemistry (HC) and IHC analysis of PM-derived organoids and their tissue of origin. Scale bar, 100 μm. Surgical samples and the derived C3 and C4 organoids (passage numbers: P10 and P14, respectively) were developed from patients S16-8598 and S17-3963 who underwent CRS–HIPEC for PM (Supplementary Table S1). (**B**) Quantitative analysis for the expression of CRC markers and Ki-67 in C3 and C4 organoids versus their corresponding tumor of origin. Positive cells were measured as the percentage of CK AE1/AE3$^+$, CK20$^+$, CK19$^+$, CDX2$^+$, and Ki-67$^+$ cells on the total number of cells present in regions free of dead cells. Three high-magnification (40×) fields per experiment were counted. Data are shown as median ± standard deviation (SD) of CK AE1/AE3$^+$, CK20$^+$, CK19$^+$, CDX2$^+$, and Ki-67$^+$ cells present in each FFPE sample. Cells were counted using Qupath software. The experiment was performed in triplicate. (**C**) Micrographs showing a glandular-like branched (left) and a spherical-like cohesive (right) organoid. Scale bar, 100 μm. (**D**) IHC analysis of organoids (top) and their tissue of origin (bottom), using LGR5 immunostaining. Scale bar, 100 μm. (**E**) Quantitative counts of the percentage of LGR5$^+$ cells in C3 and C4 organoids versus their corresponding tumor of origin. Positive cells were measured as the percentage of LGR5$^+$ cells on the total number of cells present in regions free of dead cells. Three high-magnification (40×) fields per experiment were counted, and data are presented as median ± SD of LGR5$^+$ cells present in each FFPE sample. Cells were counted using Qupath software. The experiment was performed in triplicate. (**F**) Summary of cancer-related genes with acquired mutations in TDO with respect to their tumor of origin (red boxes). The percentage of similarity was reported. Passage numbers of the organoid lines were: C1, P11; C2, P13; C3, P10; C4, P14; C6, P10.

staining revealed the maintenance of the architectural structure of the corresponding non-decellularized samples (Figure 2C and D). Finally, lyophilyzed 3D-dECMs were added to the culture media and no differences were observed in cell viability after 72 h of growth, indicating that the decellularization procedure has no cytotoxic effects (Supplementary Figure S2B).

3D-dECMs: morphological features and mechanical properties

Confocal reflection, polarized light microscopy, and atomic force microscopy (AFM) techniques were used to characterize the biophysical properties of patients' peritoneal tissues. Confocal reflection and polarized light investigations showed that the differences between normal and neoplastic tissues obtained from three different PM patients were related to both tissue texture and single collagen fiber distribution and integrity (Figure 3A). The normal 3D-dECMs showed a higher density and clusters of collagen fibers, with a random relative orientation; in the neoplastic 3D-dECMs, the collagen structure appears more irregular and porous, although a tendency toward alignment and clustering of fibers on a larger scale can be observed. AFM topographical analysis revealed an asymmetric distribution of collagen on a micrometric scale: matrices derived from normal tissues are organized in groups of very thin, intersecting fibers (with diameters <50 nm), characterized by a variety of orientations, while matrices derived from neoplastic tissues exhibit a more coiled and disarranged surface pattern (Figure 3B).

At odds with the case of ECM derived from healthy and CRC-affected tissues (Nebuloni et al., 2016), we do not observe a

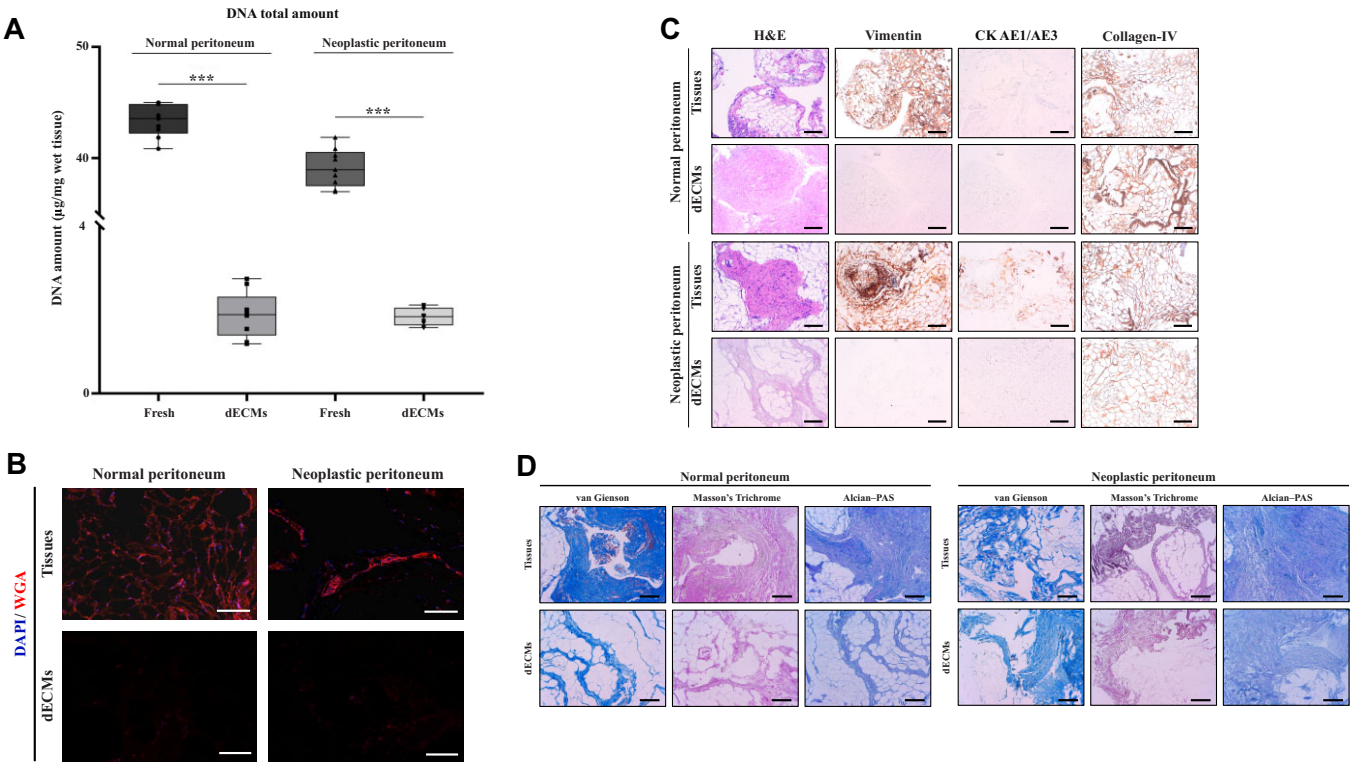

Figure 2 Establishment of 3D-dECM scaffolds from peritoneal cavity. (**A**) DNA quantification of normal and neoplastic peritoneal tissue samples before (fresh) and after the decellularization treatment (dECM). Student's *t*-test (***$P < 0.001$). (**B**) IF analysis of normal and neoplastic peritoneal samples before and after decellularization using the WGA (red) staining. The samples were counterstained with DAPI (blue). Scale bar, 100 µm. (**C**) IHC analysis of fresh peritoneum-derived tissues and the corresponding decellularized samples using H&E staining and vimentin, pan-Cytokeratin, and collagen-IV immunostaining. Scale bar, 200 µm. (**D**) Van Gienson, Masson's Trichrome, and Alcian–PAS staining on fresh and decellularized peritoneum-derived samples. Scale bar, 200 µm.

clear tendency for collagen fibers to form aligned bundles in the neoplastic state, although at this small scale, the neoplastic matrix appears structurally more compact than the normal ECM. The increased anisotropy of the ECM structure reported by Nebuloni et al. (2016) in the case of CRC is more evident in the confocal optical image of the neoplastic sample (Figure 3A). Collagen was less abundant in the neoplastic tissue than in normal tissue, but the latter showed higher levels of glycosaminoglycans (GAGs). Both collagen and GAG levels decreased in decellularized samples (∼20% loss in 3D-dECMs; ***$P < 0.001$ and **$P < 0.01$, Figure 3C).

AFM nanomechanical analysis (details in Supplementary Materials and methods) showed that the neoplastic 3D-dECMs had a wider distribution of Young's modulus (YM) values and were markedly stiffer than normal 3D-dECMs (Figure 3D). In addition, the YM distributions were considerably scattered and there was a significant overlap between the two conditions. These results indicate that the ECM is a complex system that remains locally heterogeneous on the scale of several typical cellular lengths, i.e. 10–100 µm, because the transition from the normal to the neoplastic condition, in terms of change in stiffness and structural organization, is not uniform across the whole macroscopic tissue region. Figure 3E shows YM values measured at the different sites and conditions: the stiffening is statistically significant for four out of five patients.

Decellularized scaffolds sustain PM-derived organoid growth

To develop an *in vitro* model of PM disease, 3D-dECMs were repopulated with C1, C2, and C3 TDO, with mutational profiles resembling the most common gene alterations in CRC (C1 was *KRAS*-mutant, C2 was *BRAF*-mutant, while C3 had amplified *FGFR1*). In line with literature data showing that colonization of decellularized matrices takes 8–12 days, TDO were grown on the matrices for 5, 12, and 21 days (Genovese et al., 2014; Chen et al., 2016; Weijing et al., 2021). Five days after seeding, C1 organoids were localized along the perimeter of the 3D-dECMs generated from the normal peritoneum (Figure 4A). A similar distribution was observed at 12 and 21 days after seeding, with a slight increase in the number of cells in the stromal region. In the 3D-dECMs generated from the neoplastic peritoneum, instead, C1 TDO were distributed throughout the matrix at 5 days after seeding, and colonization was evident with high stromal infiltration at Day 21 (Figure 4A; Supplementary Figure S3A and B). After 5 days, TDO maintained their spheroid

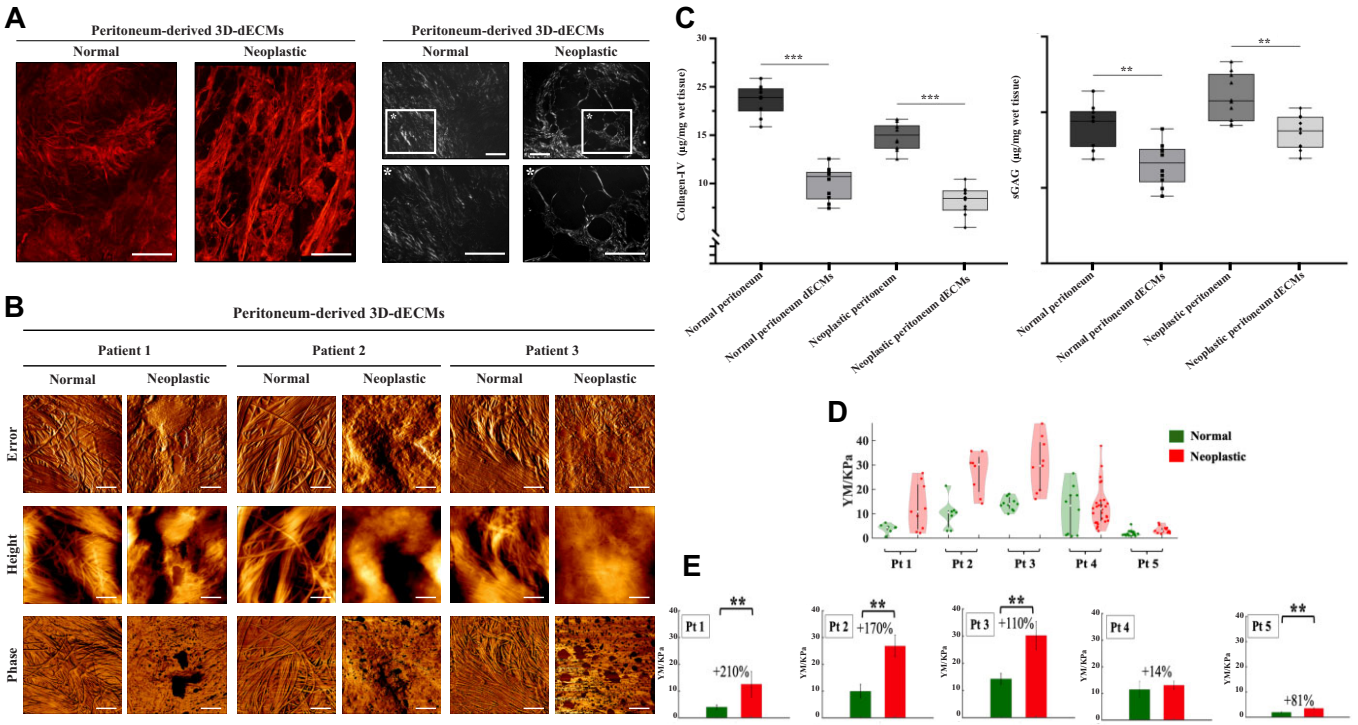

Figure 3 Morphological and mechanical properties of PM-derived 3D-dECMs. (**A**) Confocal and polarized light microscopy analysis of peritoneum-derived 3D-dECM samples. Confocal images (left panel) were obtained by scanning different areas of the samples (area ~1 mm^2), which were then assembled into a single mosaic figure. Scale bar, 200 μm (confocal images) and 50 μm (light microscopy images). (**B**) Topography analysis of peritoneum-derived 3D-dECMs. Phase, height, and peak force error images of both normal and neoplastic decellularized matrices are shown. Scale bar, 1 μm. (**C**) Quantification of collagen-IV and sGAG on fresh and decellularized peritoneal tissues. Student's *t*-test (***$P < 0.001$ and **$P < 0.01$). (**D**) Distribution of the YM values obtained for each patient and condition (normal and neoplastic). Violin-plots: each dot represents the median YM value extracted from a single measurement with Point and Shot made by ~225 force curves. Pt, patient; KPa, kilo Pascal. (**E**) Statistical analysis results of the YM value for each patient and condition tested. The bars and error bars represent mean of the median YM values and effective SD of the mean. The percentages represent the relative stiffening of the neoplastic ECM. Student's *t*-test (**$P < 0.01$).

shape on both scaffolds; at Day 12, single cells began to be observed, especially on the normal matrix, and their number increased significantly at Day 21 (Supplementary Figure S3C). After 21 days, TDO grown on neoplastic 3D-dECMs were able to infiltrate and colonize the ECM much better than TDO grown on normal 3D-dECMs (***$P < 0.001$; Figure 4B; Supplementary Figure S3D and E). The cell density of C1, C2, and C3 TDO grown on neoplastic 3D-dECMs was 520, 960, and 980 cells/mm^2, respectively, and decreased to 200, 470, and 500 cells/mm^2 when TDO were cultured on normal 3D-dECMs. The morphological characteristics and the efficiency of TDO infiltration were correlated with the grade and differentiation state of their tumors of origin. Organoids derived from grade III/G2 metastatic lesions with moderate undifferentiation and low invasive capacity (C1) infiltrated into the 3D-dECMs as single cells, while organoids from poorly undifferentiated grade IV/G3 tumors with *BRAF* mutation (C2) and *FGFR1* amplification (C3) infiltrated into the 3D-dECMs maintaining the spheroid shape (Figure 4A and B; Supplementary Figure S3A–E). Finally, we performed cleaved CASPASE3 (cCASPASE3) staining to assess cell death of TDO grown on the different 3D-dECMs, observing that cCASPASE3 expression was higher in TDO grown on normal peritoneum scaffolds (Supplementary Figure S3F).

3D decellularized scaffolds support the proliferation of organoids

Results showed that 3D-dECMs generated from neoplastic peritoneum had a significantly higher percentage of Ki-67$^+$ cells at Days 5 and 12 (***$P < 0.001$) after seeding, indicating that these organoids underwent a faster growth (Figure 4C and D; Supplementary Figure S3G–L). The neoplastic peritoneum appears to be more favorable for organoid growth, partly because factors promoting TDO growth previously released by resident cells were not removed by the decellularization methods. No differences were observed at Day 21 after seeding. Most likely, after 21 days of growth, the cells on the neoplastic matrix are confluent and the stem cell pool stops growing.

LGR5$^+$ staining showed that the stem cell pool was maintained on both normal and neoplastic 3D-dECMs at 5 and 12 days after seeding (Figure 4E and F; Supplementary

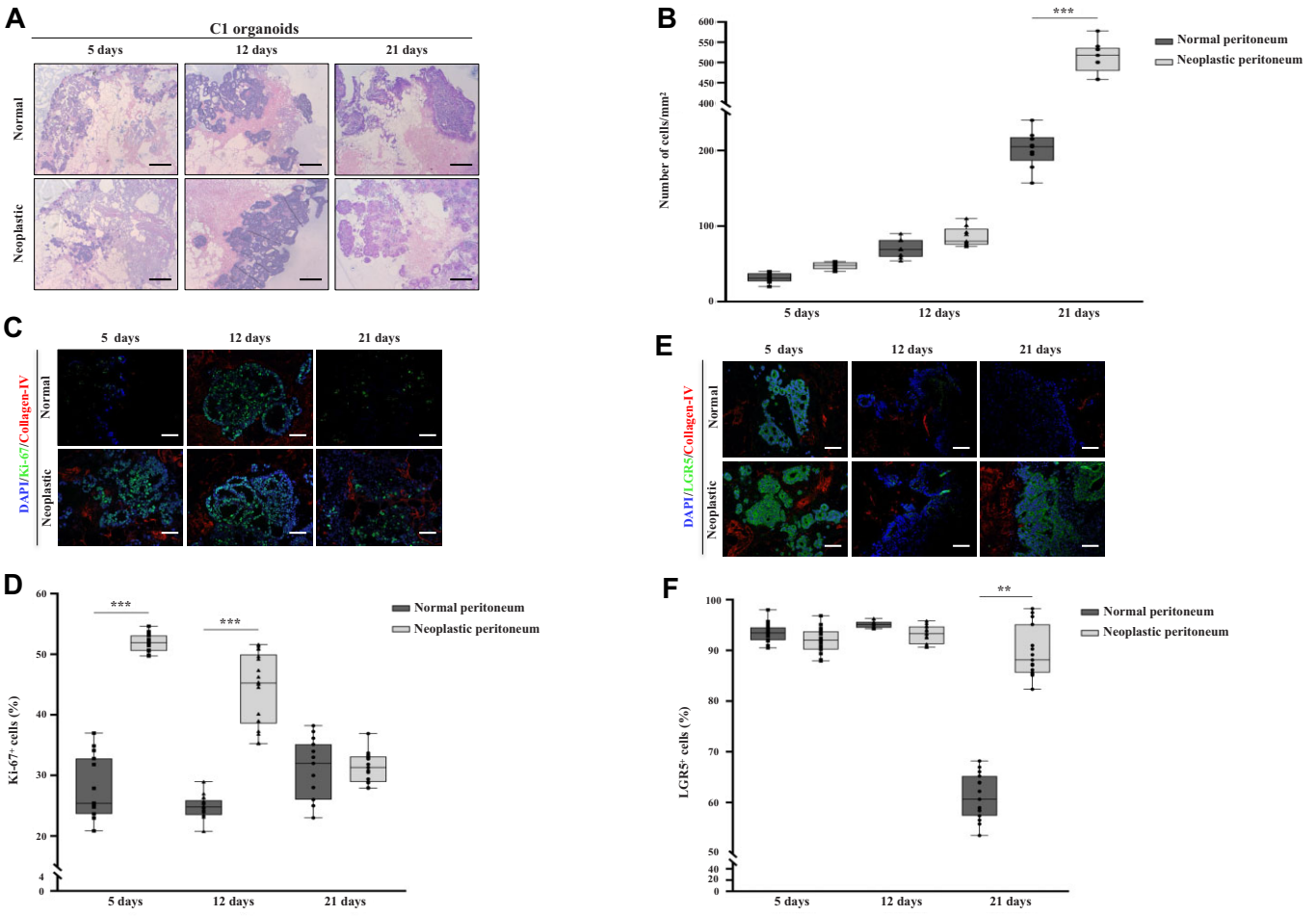

Figure 4 Peritoneum-derived 3D-dECM scaffolds support colonization, infiltration, and proliferation of PM-derived organoids, maintaining the stem cell pool. (**A**) H&E staining of decellularized matrices derived from normal (top) or neoplastic (bottom) peritoneum repopulated with PM-derived organoids (C1). Scale bar, 50 μm. The repopulation experiments were performed in triplicate. (**B**) Number of cells from PM-derived organoids grown on normal and neoplastic 3D-dECMs after 5, 12, and 21 days. Data are presented as median ± SD of three fields per experiment, counted using Qupath software. One-way ANOVA (***$P < 0.001$). (**C**) IF analysis of 3D-dECMs derived from normal (top) and neoplastic (bottom) peritoneum repopulated with organoids (C1) using Ki-67 (green) and collagen-IV (red) antibodies. The samples were counterstained with DAPI (blue). Scale bar, 20 μm. (**D**) Proliferation rate of organoids measured as the percentage of Ki-67$^+$ cells present in fields devoid of dead cells. Data are presented as median ± SD of five fields per experiment (40× magnification), counted using Qpath software. One-way ANOVA (***$P < 0.001$). (**E**) IF analysis of 3D decellularized matrices derived from normal (top) and neoplastic (bottom) peritoneum repopulated with organoids (C1) using LGR5 (green) and collagen-IV (red) antibodies. The samples were counterstained with DAPI (blue). Scale bar, 20 μm. (**F**) Amount of stem cells in organoids, measured as the percentage of LGR5$^+$ cells present in fields devoid of dead cells. Data are presented as median ± SD of five fields per experiment (40× magnification), counted using Qupath software. One-way ANOVA (**$P < 0.01$).

Figure S3G–L). At Day 21, the stem cell pool was significantly lower on 3D-dECMs generated from normal peritoneum than on 3D-dECMs generated from neoplastic peritoneum. Most likely, the cells are confluent and the stem cell pool grown on the neoplastic matrix has an environment that favors the maintenance of its phenotype, as demonstrated by transcriptomics analyses (see below and Supplementary Figure S5C).

Stiffness of 3D-dECMs does not activate YAP/TAZ proteins

The expression of Yes-associated protein (YAP) and Tafazzin (TAZ) was investigated on TDO grown on different substrates. IHC analyses showed that YAP and TAZ were expressed in all TDO grown in Matrigel and localized in the nucleus and in the cytoplasm, respectively (Supplementary Figure S4A–C). TDO were positive for YAP/TAZ expression. For example, C3 showed 55% of cells positive for TAZ and 75% of cells positive for YAP (Figure 5A; Supplementary Figure S4A–C). In contrast, YAP and TAZ were not expressed in TDO grown on normal and neoplastic 3D-dECMs, with cells positive for YAP and TAZ always <5% (Figure 5A–C; Supplementary Figure S4A–C), indicating that the peritoneum-derived matrix is able to modulate and block their expression levels. Both proteins were expressed only in C1 (Supplementary

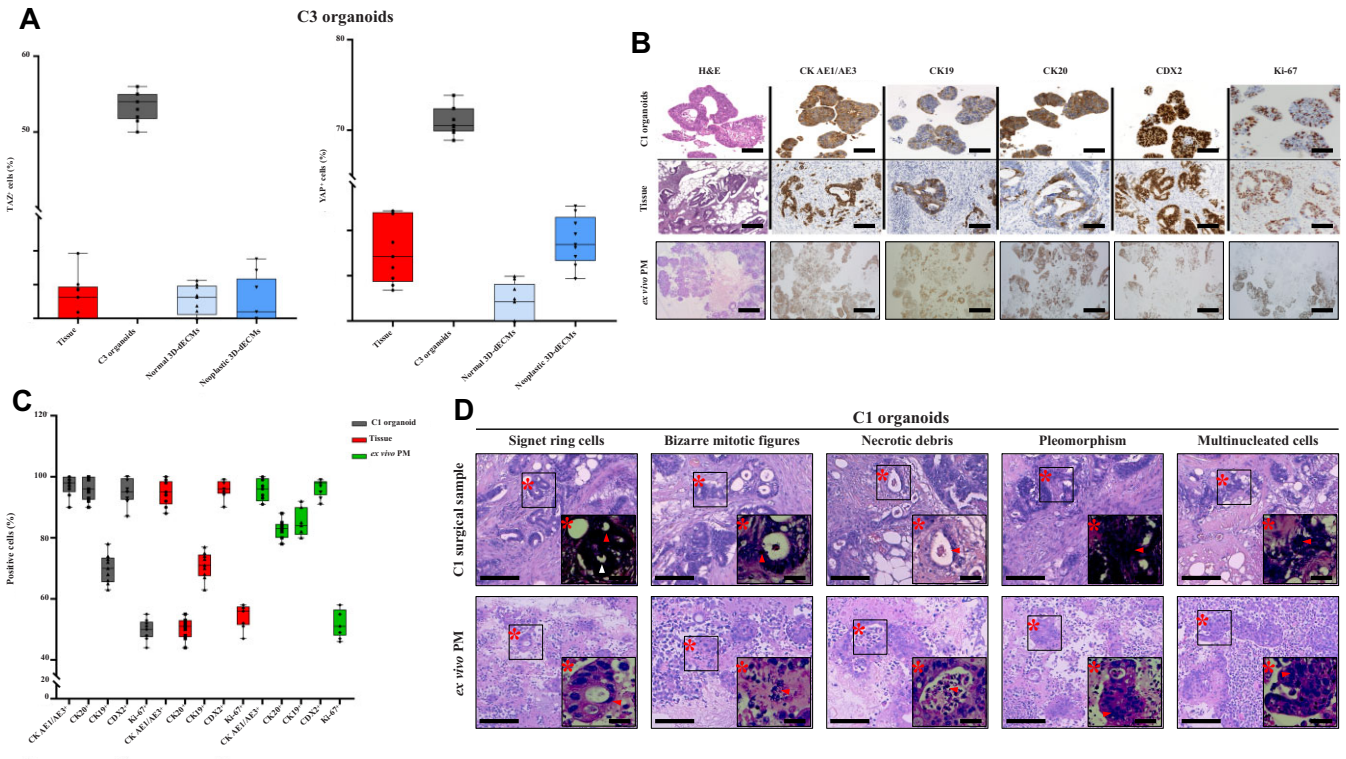

Figure 5 *Ex vivo* engineered PM lesions are comparable to PMs *in vivo*. (**A**) Percentage of YAP^+ and TAZ^+ cells in PM-derived TDO (C3). Data are presented as median ± SD of three fields per experiment (40× magnification), counted using Qupath software. (**B**) Comparative HC and IHC images of organoids (C1) versus their corresponding tumor of origin and the *ex vivo* engineered PM lesion. Samples were analyzed for the expression of CRC-specific markers and Ki-67. Scale bar, 100 μm. Images in the first two lanes were previously published (Bozzi et al., 2017). (**C**) Quantitative counts of the percentage of CRC marker-positive and Ki-67^+ cells in C1 organoids versus their corresponding tumor of origin and the *ex vivo* engineered PM lesion. Data are presented as median ± SD of three fields per experiment, counted using Qupath software. One-way ANOVA did not show differences among the three groups. (**D**) HC comparison of PM surgical sample and neoplastic peritoneum-derived 3D-dECMs repopulated with PM-derived organoids (C1). Asterisks and arrows indicate the main morphological features. Scale bar, 20 μm.

Figure S4A–C), with YAP mainly located in the nucleus and TAZ in the cytoplasm.

Ex vivo engineered PM lesions reproduce patient PM

IHC analysis of the TDO using colorectal markers showed that repopulated 3D-dECMs retain the main characteristics and the morphology of their tumor of origin (Figure 5B; Supplementary Figure S4D and F), expressing the colorectal markers in almost the same percentage of cells as their tissue of origin (Figure 5B and C; Supplementary Figure S4H and I), except for CK20 and CK19 more expressed in the *ex vivo* model, probably because decellularized matrices stimulate their expression. However, ANOVA analysis among the three groups showed no significant variations. The *ex vivo* PM lesions had the typical histological features observed in PM patients, such as (i) signet ring cells, (ii) bizarre mitotic figures, (iii) necrotic debris, (iv) pleomorphic cell size and shape, and (v) multinucleated cells (Figure 5D; Supplementary Figure S4E and G). Signet ring cells have been reported in another *ex vivo* model system (Tian et al., 2018), highlighting that our model of PM is highly representative of *in vivo* lesions.

Gene expression analysis of engineered PM lesions

RNA sequencing (RNA-seq) analysis of the TDO (Figure 6) revealed differences between 3D-dECMs and Matrigel substrates: 327 differentially expressed genes (DEGs) were identified in TDO grown on normal 3D-dECMs and 144 DEGs were identified in TDO grown on neoplastic 3D-dECMs, compared with the TDO grown in Matrigel (|fold change (FC)| $>$ 1.5 and adjusted *P*-value $<$0.05).

The most represented biological processes include cell–cell/cell–matrix interactions, organoid behavior and interactions with the ECM, angiogenesis, metal ion homeostasis, and response to external stimuli. 3D-dECMs deregulated many genes critical for the 3D architecture/organization of the ECM. Many of the upregulated genes identified in TDO grown on neoplastic 3D-dECMs were assigned to the Matrisome database (67% for neoplastic vs. normal 3D-dECMs, and 25% for neoplastic 3D-dECMs vs. Matrigel). Only 8% of the upregulated genes identified in TDO grown on normal 3D-dECMs compared with TDO grown in Matrigel belonged to the Matrisome database (Figure 6A). Unsupervised hierarchical clustering of TDO showed a separation between TDO grown on neoplastic 3D-dECMs and

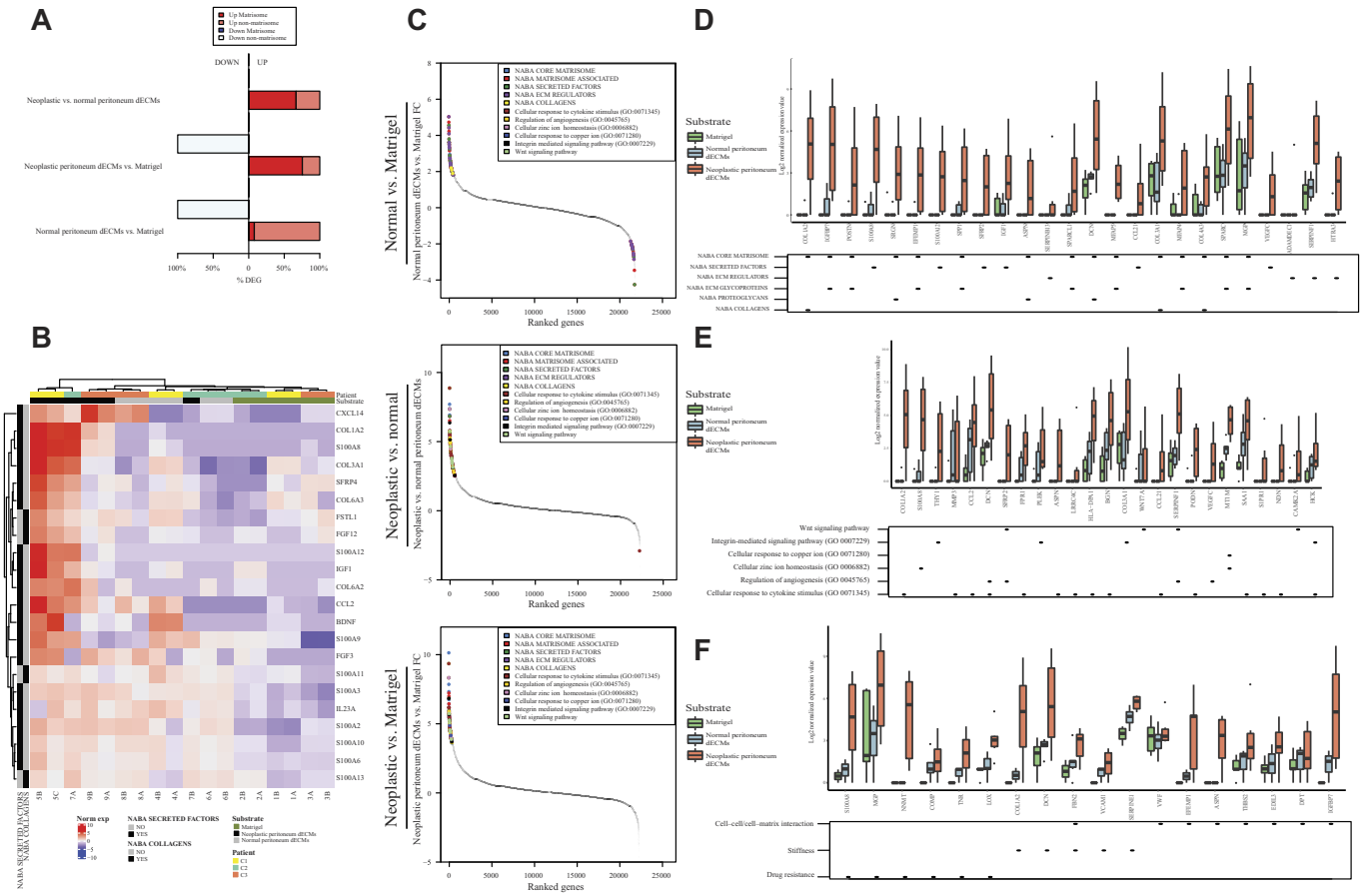

Figure 6 Gene expression analysis of engineered PM lesions. (**A**) Percentages of upregulated and downregulated genes belonging to the Matrisome dataset. (**B**) Unsupervised hierarchical clustering of the organoids according to the expression of the top DEGs included in Naba Secreted Factors and in Naba Collagens categories. (**C**) FCs of genes belonging to the indicated gene sets among the top 100 deregulated genes. Gene ranks for relative FC are shown on the x-axis and the logFCs on the y-axis. (**D**) Box plots showing the expression of genes selected for their involvement in the indicated processes of the Naba Matrisome datasets. Median and interquartile range are displayed as horizontal lines. Black squares in the bottom panel indicate which category the genes belong to. (**E**) Expression of genes selected for their involvement in the indicated processes of GO biological process and KEGG databases. Median and interquartile range are displayed as horizontal lines. Black squares in the bottom panel indicate which category the genes belong to. (**F**) Expression of genes selected for their involvement in the indicated processes, using a selection of genes related to the following biological processes: cell–cell/cell–matrix interactions, extracellular matrix stiffness, and drug resistance. Median and interquartile range are displayed as horizontal lines. Black squares in the bottom panel indicate which category the genes belong to.

TDO grown on normal 3D-dECMs and in Matrigel substrates (Figure 6B; Supplementary Figure S5A–C). TDO grown on normal and neoplastic 3D-dECMs exhibited an over-representation of DEGs involved in ECM composition, regulation, and modulation (Figure 6C). Growth on 3D-dECMs also promotes the expression of genes involved in the regulation of angiogenic processes, response to cytokine stimuli, the integrin pathway, and copper and zinc metabolism. The same categories were found for both normal and neoplastic 3D-dECMs (Supplementary Figure S5C and D).

Using the Matrisome database, we identified genes related to the ECM core composition and ECM interactors/regulators through secretion of specific factors, all of which were higher in 3D-dECMs derived from neoplastic tissue (Figure 6D; Supplementary Figure S5E–H). The 3D-dECMs had high expression of genes involved in stem cell pathways, cellular response to cytokines, zinc and copper metabolism, integrin pathway, and regulation of angiogenesis (Figure 6E; Supplementary Figure S5E–H). Similar results were found for genes involved in cell–cell/cell–matrix interactions (Figure 6F). Finally, gene set enrichment analysis showed no differences in genes from the pathways known to be regulated by YAP/TAZ (Supplementary Figure S5M).

The differences observed with transcriptomic data were validated by quantitative real-time polymerase chain reaction of some representative genes on C1, C2, and C3 TDO grown in Matrigel and on normal and neoplastic 3D-dECMs. The tissue of origin of the six TDO was also analyzed. The trends

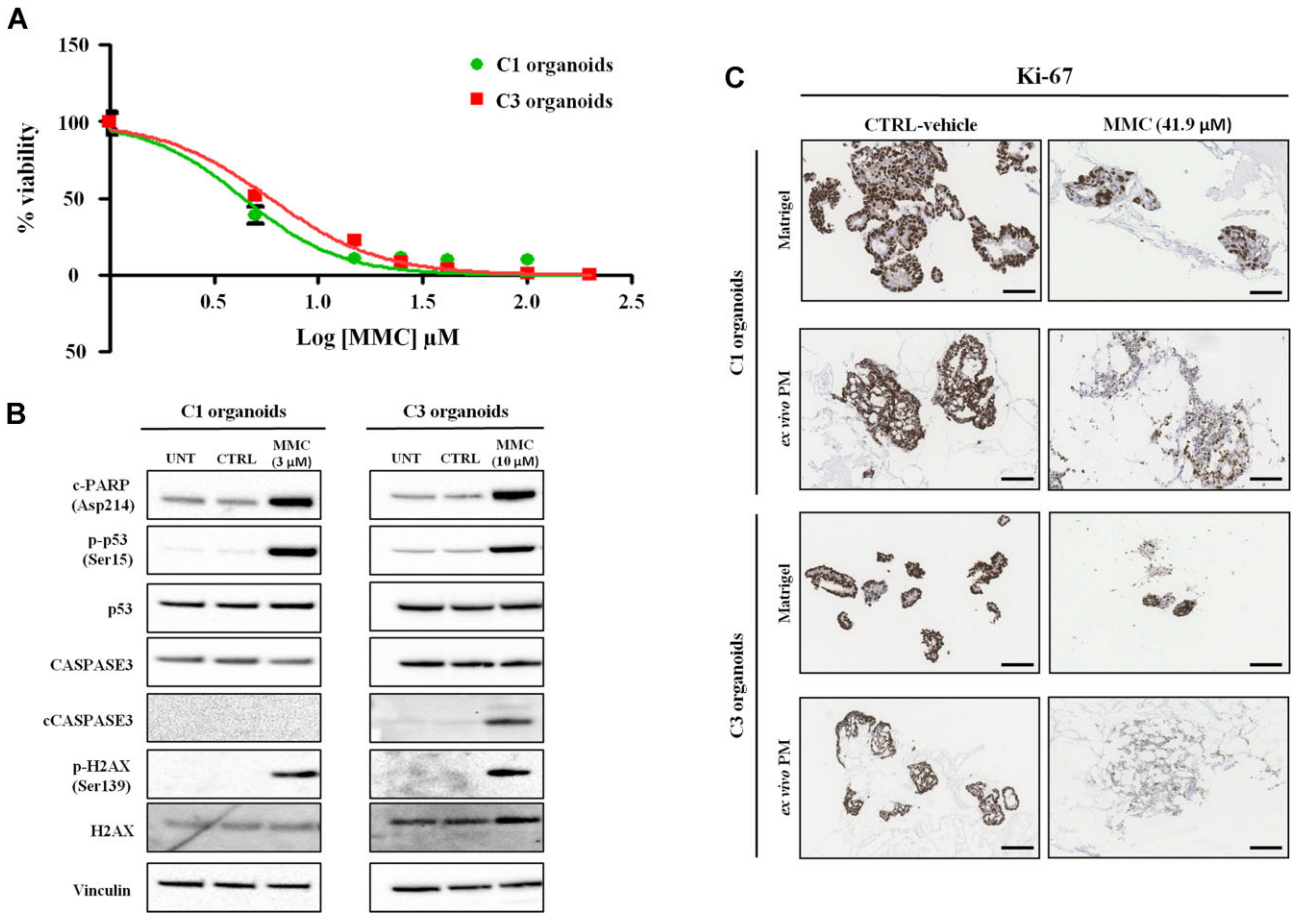

Figure 7 3D-dECM scaffolds decrease the efficacy of HIPEC treatments. (**A**) Dose–response curve of C1 and C3 organoids cultured in Matrigel and treated with MMC at different concentrations at 42.5°C for 1 h. (**B**) Immunoblots of C1 and C3 organoids treated with MMC at 3 µM and 10 µM, respectively. Vinculin was used as loading control. (**C**) IHC analysis of C1 and C3 organoids cultured in Matrigel and on neoplastic peritoneum-derived 3D-dECMs, after *in vitro* HIPEC treatments, using Ki-67 immunostaining. Scale bar, 50 µm.

observed by RNA-seq were confirmed and all the genes analyzed were also expressed in the tissue of origin (Supplementary Figure S5I and L).

3D-dECMs decrease the efficacy of HIPEC treatments

The TDO analyzed had different IC_{50} values: C3 TDO were the most sensitive and C2 the least one to both mitomycin-c (MMC) and oxaliplatin (OXA) (Figure 7A; Supplementary Figure S6C and E). At these values, MMC treatment induced DNA damage and apoptosis in all TDO, as shown by phosphorylation of p53 (Ser15) and H2AX (Ser139) (Figure 7B; Supplementary Figure S6D) and cleavage of PARP and CASPASE3 (Figure 7B; Supplementary Figure S6D). OXA treatment also induced DNA damage and apoptosis in all TDO, although C2 TDO showed only PARP cleavage (Supplementary Figure S6G).

To evaluate the contribution of the ECM to treatment response, we simulated treatment with HIPEC on *ex vivo* engineered micrometastases. C1, C2, and C3 TDO were grown on neoplastic 3D-dECMs for 12 days, a time considered sufficient for the matrix surface colonization (Weijing et al., 2021), and treated with MMC and OXA. Treatment with MMC induced cell rupture in C1 and C3 organoids (Supplementary Figure S6A). Ki-67 expression was lower in the treated group, also showing a diffuse cytoplasmatic signal (Figure 7C; Supplementary Figure S6B). The number of Ki-67$^+$ cells in C1 TDO grown in Matrigel or on 3D-dECMs, was reduced by 95% and 72%, respectively, compared with the untreated control groups (**$P < 0.01$; Figure 8A). Proliferation was reduced by 80% and 66%, respectively, in C3 organoids grown in Matrigel or on 3D-dECMs, compared to the untreated control groups (**$P < 0.01$; Figure 8A). Immunofluorescence (IF) staining with cCASPASE3 confirmed that untreated C1 and C3 TDO were alive (Figure 8C, left panel). The number of cCASPASE3$^+$ cells in C1 TDO grown in Matrigel or on 3D-dECMs was 80% and 60%, respectively, compared with the untreated control groups (**$P < 0.01$; Figure 8B), and 80% and 50%, respectively in C3 TDO (**$P < 0.01$; Figure 8B). MMC treatment had no effect on C2 organoids (Supplementary Figure S6C–E). Regarding OXA treatment, the number of cCASPASE3$^+$ cells in TDO grown in Matrigel or on 3D-dECMs was 50% and 70% for C1, 60% and 85% for C2, and 45% and 65% for C3, compared with untreated control groups (**$P < 0.01$; Supplementary Figure S6F–H).

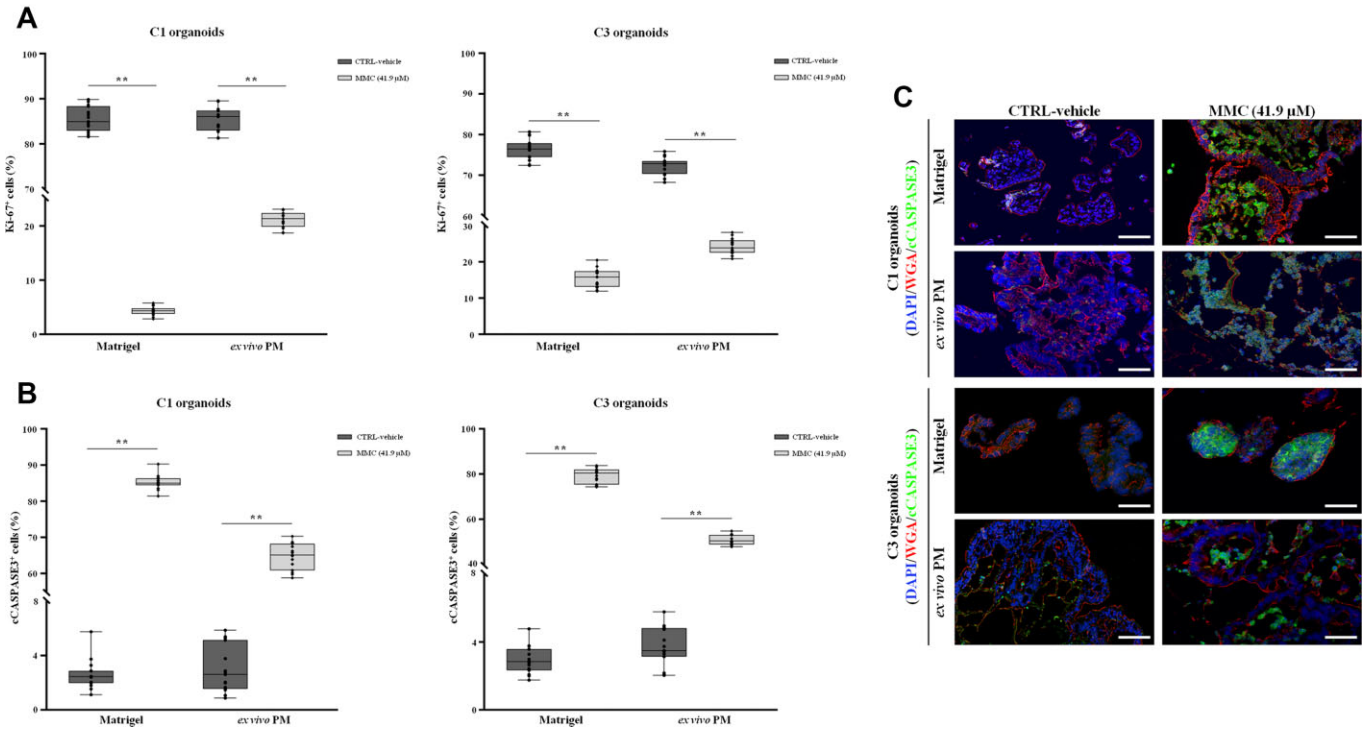

Figure 8 3D-dECMs reduce HIPEC-induced apoptosis in TDO. (**A**) Proliferation rate of PM-derived organoids (C1, left panel; C3, right panel) measured as the percentage of Ki-67$^+$ cells present in fields free of dead cells. Data are presented as median ± SD of five fields per experiment (40× magnification), counted using Qupath software. One-way ANOVA (**$P < 0.01$). (**B**) Percentage of apoptotic organoids (C1, left panel; C3, right panel) measured as the percentage of cCASPASE3$^+$ cells present in selected fields. Data are presented as median ± SD of five fields per experiment (40× magnification), counted using Qupath software. One-way ANOVA (**$P < 0.01$). (**C**) IF analysis of C1 and C3 organoids cultured in Matrigel and on neoplastic peritoneum-derived 3D-dECMs, after HIPEC treatments, using cCASPASE3 antibody (green). The samples were counterstained with WGA (red) and DAPI (blue). Scale bar, 20 μm.

These results demonstrate that HIPEC induces apoptosis in TDO and the presence of 3D-dECMs hinders its efficacy (Figures 7 and 8).

Discussion

Here, we describe an engineered model that combines key features of TDO within the microenvironment, enabling the recapitulation of the PM niche under physiological conditions. Our findings are in line with previous works showing that cancer-derived ECM sustains the proliferation and invasion of CRC cell lines (D'Angelo et al., 2020).

Scaffolds derived from neoplastic peritoneum showed greater stiffness than those derived from normal peritoneum. Increased stiffness and crosslinking of the perilesional ECM was identified as an environmental change predisposing to CRC invasion and can be attributed in part to the more compact fine structure of the matrix and to the linearization of the fibers in bundles (Nebuloni et al., 2016). The increased amount of GAG observed in the perilesional ECM may also be related to increased stiffness. In fact, some authors have shown that negatively charged GAGs provide a repulsive force that opposes compression and shear in the ECM (Buschmann and Grodzinsky, 1995); in addition, the ability of GAGs to retain high quantities of water and hydrated cations confers resistance to compressive forces (Buschmann and Grodzinsky, 1995). The high amount of GAGs observed in neoplastic tissues could be the result of metastatic transformation. In fact, the sulfated GAG (sGAG) chondroitin-sulfate is the main binding site for the isoform v of CD44, which is a key player in metastatic spread (Zanconato et al., 2019). Transcriptome analysis also confirmed higher expression of GAGs in the repopulated neoplastic 3D-dECMs.

Our observations support the proposed role of *YAP* as a tumor suppressor in metastatic CRC, where it can inhibit the Wnt pathway by reprogramming *LGR5*$^+$ cells and, *in vivo*, by reducing Wnt activity (Cheung et al., 2020). Indeed, Wnt pathway activity was one of the most represented Gene Ontology (GO) categories higher in TDO grown on 3D-dECMs than in Matrigel. Analysis of YAP/TAZ expression in tumor tissue from which TDO were derived corroborates this hypothesis. The presence of YAP/TAZ in TDO grown in Matrigel is likely due to the different stiffness of Matrigel compared with 3D-dECMs and the absence of factors previously released from the tumor cells, which are instead present in the 3D-dECMs and could regulate YAP/TAZ signaling activity (Panciera et al., 2017). This result highlights how commercially available substrates fail to fully reproduce the *in vivo* context. Factors other than YAP/TAZ signaling, present in the

stromal compartment, could influence the mechanobiology of the peritoneum. For example, cancer-activated fibroblasts can activate a complex signaling network capable of remodeling and/or removing the ECM, through the activation of the TGFβ pathway (Sanders et al., 2015). The interactions between the ECM and stromal and tumor cells could also regulate the secretion of specific molecules that can induce fibrosis through cytokines and growth factors-mediated pathways (Vasiukov et al., 2020). Indeed, the cytokine signaling-mediated pathway was one of the most represented GO categories observed. These data indicate the development of a complex cell–cell and cell–ECM communication network and suggest a prominent role of the stromal compartment in the mechanical characteristics of the peritoneal ECM. Future experiments will be needed to elucidate how stromal cells can affect mechanobiology of the peritoneal ECM through co-culture of tumor cells, ECM, and stromal cells.

Morphological and topographical experiments showed that the neoplastic scaffold undergoes complex structural modifications that enhance TDO adhesion and proliferation. In support of this concept, both normal and tumor 3D-dECMs showed an upregulation of genes involved in zinc and copper metabolism and homeostasis, which was greater in the neoplastic peritoneum-derived matrix. These metal ions are involved in the regulation and activation of the metalloproteinase enzymes, which are the main modulators of the ECM through a proteolytic activity (Ceelen et al., 2020) and could play a role in the activation of ECM remodeling pathways underlying the metastatic niche.

Transcriptomic analyses showed that repopulated 3D-dECMs presented typical features of the PM disease (Jayne et al., 2002; Siegel et al., 2014) and expressed genes involved in ECM remodeling, such as NABA Matrisome and stem cell-related genes, ECM regulators, and genes involved in the response to cytokine and pro-inflammatory stimuli, integrin interactions and collagen/proteoglycan modifications, epithelial cell differentiation, resistance to compression, and regulation of angiogenesis (Bajou et al., 2008; Schlesinger and Bendas, 2015). These pathways were less represented in normal 3D-dECMs and absent in Matrigel samples, confirming a previous study showing that growth on the ECM of normal colon organoids transfected with mutant *APC* induces features typically associated with CRC progression (Chen et al., 2016). The deregulation of genes belonging to pathways involved in the metastatic process, related to metastatic spread and the development of the metastatic niche (Varghese et al., 2007; Lemoine et al., 2016), is in agreement with the fact that our organoids are derived from metastatic lesions, where the cells activate a series of pathways to better fit to the niche.

HIPEC simulation experiments highlighted the potential role of the neoplastic ECM in the development of drug resistance. Transcriptomic data indicated the activation of mechanisms related to drug resistance along with the modification of the mechanical properties of the ECM. In fact, growth on scaffolds increased the expression of anti-apoptotic and pro-survival genes, as well as genes involved in platin-based drug resistance. High expression of stiffness-related genes was also observed. Integrins, which are involved in ECM remodeling and can function as mechanotransducers, contributing to cancer metastasis, stemness, and drug resistance (Su et al., 2020), were also one of the most representative GO categories, supporting the activation of the drug resistance mechanism when TDO are grown on 3D-dECMs. Dose–response curves to MMC and OXA showed that the TDO had different drug sensitivities and that clinically administered doses of MMC and OXA were insufficient to eliminate all cancer cells. Response to treatment was even less for TDO grown on 3D-dECMs, which showed greater resistance to both drugs. In support of these findings, genes involved in drug resistance, especially to platinum-based compounds, were upregulated in TDO grown on 3D-dECMs. The results observed with the model better reproduce the results in the clinics, as ∼60% of patients treated with HIPEC relapse in one year. All these findings highlight that our proposed engineered model could be a drug screening tool that can more faithfully recapitulate the tumor microenvironment and treatment response for tailored therapies than the classical monoculture two-dimensional (2D) models, or even 3D-cultures, which are still being used (Ghajar, 2015).

However, the model has some limitations, as it does not yet reach a level of resolution that allows it to mimic the PM niche in all its constituents. In fact, other components of the microenvironment play a key role in PM spread (Hussey et al., 2017; Bleijs et al., 2019), such as immune surveillance and the vascular system (Seebauer et al., 2016; Mohrmann et al., 2020). Further optimization of our model will therefore imply the reconstruction of a specialized physiological microenvironment by incorporating vascular networks, the immune system, and organ-specific microbes. In addition, the replacement of patient-derived 3D-dECMs with a synthetic support with the same biochemical and physical characteristics of the components of the decellularized matrix will improve the reproducibility and enable personalized drug screenings on the TDO.

Our model represents a physiological tool that could aid the identification of key players in the metastatic development and may allow the selection, in a biologically relevant context, of new therapeutic strategies. Finally, the approach described here could be used to generate other types of *ex vivo* metastatic niches.

Materials and methods

Human tissues

Peritoneal tissue was collected from six patients with peritoneal metastatic colorectal carcinoma, who underwent surgical resection at the Peritoneal Malignancies Unit of our Institution. The patients were staged according to the WHO classification (Ubink et al., 2018). The study was approved by the Institutional Review Board (134/13; 149/19) and was conducted in accordance with the Declaration of Helsinki, 2009. Written informed consent was acquired. Metastatic lesions and apparently normal tissue (>10 cm from the metastatic lesions) were harvested and one part of the metastatic tissue (1 cm

in diameter) was placed in ice-cold phosphate-buffered saline (PBS; ThermoFisher Scientific) containing gentamicin (50 ng/ml, ThermoFisher Scientific) and amphotericin B (50 ng/ml, ThermoFisher Scientific) for the generation of PM-derived organoids, while a second specimen was frozen in liquid nitrogen for molecular and histopathological analyses. The remaining tissue was used to develop 3D-decellularized matrices (3D-dECMs).

Normal tissue was partly used to develop dECMs and partly frozen for further studies. FFPE blocks were prepared for IHC analyses of normal and metastatic tissue.

Development of PM-derived organoids

PM-derived TDO were developed as described in Fujii et al. (2016) and Bozzi et al. (2017). TDO were grown in basal cell culture medium consisting of advanced DMEM-F12 (ThermoFisher Scientific) and supplemented with different growth factors (Supplementary Table S2) to mimic different niche factor conditions, as described in Fujii et al. (2016). Incubation was performed at 20% O_2 and 5% CO_2. After expansion, the TDO were cultured in cell culture medium lacking growth factors, which was refreshed every three days. Optimal cell culture medium conditions were determined separately for each organoid culture (Supplementary Table S3).

Organoids were split every 1–2 weeks as follows: they were mechanically removed from the Matrigel by pipetting, incubated in Cell Recovery Solution (Corning) for 1 h at 4°C, washed twice with ice-cold PBS, and seeded as described above.

Aliquots of each organoid culture were frozen or prepared for IHC analyses as follows: samples were fixed in 10% formalin at room temperature for 10 min and embedded into 200 µl Bio-Agar (Bio-Optica). The samples were then cooled at −20°C until solidification. For each sample, sections of 3 µm thickness were obtained.

Preparation of 3D-dECMs

3D-dECMs were derived from both PM and the corresponding normal peritoneum. Each experiment was conducted using 3–10 different surgical specimens derived from different patients.

The decellularization was performed as described in Genovese et al. (2014). Briefly, both PM and normal peritoneum samples (60–100 mg wet weight) were washed with ice-cold PBS supplemented with 50 ng/ml gentamicin and 50 ng/ml amphotericin B, followed by treatment with solutions containing detergents and enzymatic agents.

The success of the decellularization procedure was evaluated by analyzing the DNA content of the 3D-dECMs. The 3D-dECMs were then washed with ice-cold PBS and either transferred into chilled freezing solution (90% DMEM-F12 and 10% dimethyl sulfoxide) and frozen for storage or fixed for IHC and IF analyses. All the decellularization experiments were performed in triplicate, using at least three different samples, each derived from a different donor.

Ex vivo engineered PM lesion

TDO were removed from the Matrigel as described above and dissociated into single-cell suspensions with trypsin–EDTA by vigorous pipetting for 10 min. 3D-dECMs derived from normal peritoneal tissue and PM were incubated overnight at 37°C in DMEM-F12 supplemented with 10% fetal bovine serum (FBS; Euroclone) and 50 ng/ml gentamicin and amphotericin B. Then, 1×10^6 cells were resuspended in 1 ml cell culture medium (Supplementary Table S2) and seeded on the top of 50 mg of 3D-dECMs. Repopulated matrices were placed in a 24-well cell culture plate (Corning) containing DMEM-F12 supplemented with 10% FBS and 50 ng/ml gentamicin and amphotericin B, followed by incubation for 2 h at 37°C. Each well was filled with 2 ml cell culture medium, which was changed every two days. Repopulated matrices were either frozen for RNA extraction or fixed for IHC and IF analyses. Representative 3-µm FFPE sections were cut at different depths to verify the presence of TDO in the inner part of the 3D-dECM scaffold. The repopulation experiments were performed in triplicate, using different neoplastic and normal peritoneum-derived matrices obtained from three different donors.

Treatment with cytotoxic drugs

MMC (Kyowa Kirin Co., Ltd) and OXA (Fresenius Kabi) were used for the *in vitro* simulation of HIPEC treatment. MMC was dissolved in dimethyl sulfoxide to obtain a 60 mM stock solution. OXA was diluted in physiological solution (0.45% sodium chloride and 2.5% glucose) to obtain a 15 mM stock solution. Both drugs were diluted to the working concentration in the cell culture medium, where the final solvent concentration was $<0.1\%$ for all samples, including controls. The experiments were performed in triplicate, using different neoplastic and normal peritoneum-derived matrices obtained from three different donors.

Ex vivo PM lesion to test HIPEC efficacy in vitro

PM-derived organoids were grown on the top of neoplastic 3D-dECMs in a 24-well cell culture plate for 12 days in order to allow a complete colonization of the matrix (Genovese et al., 2014; Chen et al., 2016; Weijing et al., 2021). TDO grown in Matrigel were used as control to evaluate the impact of native 3D-dECMs on the HIPEC treatment. The engineered PM lesions were treated with preheated MMC and OXA at a concentration of 41.9 µM for 60 min at 42.5°C and 252 µM for 90 min at 42.5°C, respectively, corresponding to the calculated clinical concentrations, which is in line with the current standard protocols used for HIPEC at Fondazione IRCCS Istituto Nazionale dei Tumori, Milan, Italy. After the treatments, the PM models were subjected to three washes with 1× PBS and incubated for 48 h with appropriate cell growth medium.

Samples were fixed in formalin and FFPE sections were obtained as described above. The impacts of HIPEC treatment on TDO proliferation and the activation of an apoptotic program were determined by Ki-67 and cCASPASE3 immunostaining, respectively. All the experiments were performed in triplicate,

using different neoplastic and normal peritoneum-derived matrices obtained from three different donors.

Supplementary material

Supplementary material is available at *Journal of Molecular Cell Biology* online.

Acknowledgements

The authors wish to thank the Imaging Technological Development Unit (TDU) of the AIRC Institute of Molecular Oncology, IFOM ETS, Milan, Italy, as well as the DNA Sequencing Facility, in particular Sara Volorio, and the Microarray Facility, in particular Mirko Riboni and Claudia Valli, of Cogentech Ltd Benefit Corporation with a Sole Shareholder, Milan, Italy. We also wish to thank Oscar Illescas Pomposo from Fondazione IRCCS Istituto Nazionale dei Tumori for helping us in TDO maintenance and development. The authors express their gratitude to Wessen Maruwge, an English author's editor in Milan, and to Tommaso Cavalleri for revising the manuscript.

Funding

This work was supported by an Italian law that allows taxpayers to allocate 0.5% of their tax to a research institution of their choice, by EU Horizon 2020 Marie Skłodowska-Curie programme 812772 (project Phys2BioMed) and by FET Open 801126 (project EDIT).

Conflict of interest: none declared.

References

Bajou, K., Peng, H., Laug, W.E., et al. (2008). Plasminogen activator inhibitor-1 protects endothelial cells from FasL-mediated apoptosis. Cancer Cell *14*, 324–334.

Baratti, D., Kusamura, S., Pietrantonio, F., et al. (2015). Progress in treatments for colorectal cancer peritoneal metastases during the years 2010–2015. A systematic review. Crit. Rev. Oncol. Hematol. *100*, 209–222.

Bleijs, M., van de Wetering, M., Clevers, H., et al. (2019). Xenograft and organoid model systems in cancer research. EMBO J. *38*, e101654.

Bozzi, F., Mogavero, A., Varinelli, L., et al. (2017). MIF/CD74 axis is a target for novel therapies in colon carcinomatosis. J. Exp. Clin. Cancer Res. *36*, 16.

Buschmann, M.D., and Grodzinsky, A.J. (1995). A molecular model of proteoglycan-associated electrostatic forces in cartilage mechanics. J. Biomech. Eng. *117*, 179–192.

Ceelen, W., Ramsay, R.G., Narasimhan, V., et al. (2020). Targeting the tumor microenvironment in colorectal peritoneal metastases. Trends Cancer *6*, 236–246.

Chen, H.J., Wei, Z., Sun, J., et al. (2016). A recellularized human colon model identifies cancer driver genes. Nat. Biotechnol. *34*, 845–851.

Cheung, P., Xiol, J., Dill, M.T., et al. (2020). Regenerative reporgramming of the intestinal stem cell state via Hippo signaling supresses metastatic colorectal cancer. Cell Stem Cell *27*, 590–604.

D'Angelo, E., Natarajan, D., Sensi, F., et al. (2020). Patient-derived scaffolds of colorectal cancer metastases as an organotypic 3D model of the liver metastatic microenvironment. Cancers *12*, 1–15.

Drost, J., and Clevers, H. (2018). Organoids in cancer research. Nat. Rev. Cancer *18*, 407–418.

Fujii, M., Matano, M., Nanki, K., et al. (2015). Efficient genetic engineering of human intestinal organoids using electroporation. Nat. Protoc. *10*, 1474–1485.

Fujii, M., Shimokawa, M., Date, S., et al. (2016). A colorectal tumor organoid library demonstrates progressive loss of niche factor requirements during tumorigenesis. Cell Stem Cell *18*, 827–838.

Genovese, L., Zawada, L., Tosoni, A., et al. (2014). Cellular localization, invasion, and turnover are differently influenced by healthy and tumor-derived extracellular matrix. Tissue Eng. Part A *20*, 2005–2018.

Ghajar, C.M. (2015). Metastasis prevention by targeting the dormant niche. Nat. Rev. Cancer *15*, 238–247.

Herszeny, L., and Tulassay, Z. (2010). Epidemiology of gastrointestinal and liver tumors. Eur. Rev. Med. Pharmacol. Sci. *14*, 249–258.

Hussey, G.S., Keane, T.J., and Badylak, S.F. (2017). The extracellular matrix of the gastrointestinal tract: a regenerative medicine platform. Nat. Rev. Gastroenterol. Hepatol. *14*, 540–552.

Jayne, D. (2007). Molecular biology of peritoneal carcinomatosis. Cancer Treat. Res. *134*, 21–33.

Jayne, D.G., Fook, S., Loi, C., et al. (2002). Peritoneal carcinomatosis from colorectal cancer. Br. J. Surg. *89*, 1545–1550.

Ksiazek, K., Mikula-Pietrasik, J., Catar, R., et al. (2010). Oxidative stress-dependent increase in ICAM-1 expression promotes adhesion of colorectal and pancreatic cancers to the senescent peritoneal mesothelium. Int. J. Cancer *127*, 293–303.

Lemoine, L., Sugarbaker, P., and Van der Speeten, K. (2016). Pathophysiology of colorectal peritoneal carcinomatosis: role of the peritoneum. World J. Gastroenterol. *22*, 7692–7707.

Mikula-Pietrasik, J., Uruski, P., Tykarski, A., et al. (2018). The peritoneal 'soil' for a cancerous 'seed': a comprehensive review of the pathogenesis of intraperitoneal cancer metastases. Cell. Mol. Life Sci. *75*, 509–525.

Mohrmann, L., Zowada, M.K., Strakerjahn, H., et al. (2020). A perivascular niche in the bone marrow hosts quiescent and proliferating tumorigenic colorectal cancer cells. Int. J. Cancer *147*, 519–531.

Nebuloni, M., Albarello, L., Andolfo, A., et al. (2016). Insight on colorectal carcinoma infiltration by studying perilesional extracellular matrix. Sci. Rep. *4*, 22522.

Panciera, T., Azzolin, L., Cordenonsi, M., et al. (2017). Mechanobiology of YAP and TAZ in physiology and disease. Nat. Rev. Mol. Cell Biol. *18*, 758–770.

Peinado, H., Zhang, H., Matei, I.R., et al. (2017). Pre-metastatic niches: organ-specific homes for metastases. Nat. Rev. Cancer *17*, 302–317.

Sanders, A.J., Chowdhury, R., Jiang, W.G., et al. (2015). Differentiation of tumor promoting stromal myofibroblasts by cancer exosomes. Oncogene *34*, 290–303.

Schlesinger, M., and Bendas, G. (2015). Vascular cell adhesion molecule-1 (VCAM-1) an increasing insight into its role in tumorigenicity and metastasis. Int. J. Cancer *136*, 2504–2514.

Seebauer, C.T., Brunner, S., Glockzin, G., et al. (2016). Peritoneal carcinomatosis of colorectal cancer is characterized by structural and functional reorganization of the tumor microenvironment inducing senescence and proliferation arrest in cancer cells. Oncoimmunology *5*, e1242543.

Siegel, R., Desantis, C., and Jemal, A. (2014). Colorectal cancer statistics, 2014. CA Cancer J. Clin. *64*, 104–117.

Su, C., Li, J., Zhang, L., et al. (2020). The biological functions and clinical applications of integrins in cancer. Front. Pharmacol. *11*, 579068.

Tian, X., Werner, M.E., Roche, K.C., et al. (2018). Organ-specific metastases obtained by culturing colorectal cancer cells on tissue-specific decellularized scaffolds. Nat. Biomed. Eng. *2*, 443–452.

Ubink, I., van Eden, W.J., Snaebjornsson, P., et al. (2018). Histopathological and molecular classification of colorectal cancer and corresponding peritoneal metastases. Br. J. Surg. *105*, e204–e211.

Varghese, S., Burness, M., Xu, H., et al. (2007). Site-specific gene expression profiles and novel molecular prognostic factors in patients with lower gastrointestinal adenocarcinoma diffusely metastatic to liver or peritoneum. Ann. Surg. Oncol. *14*, 3460–3471.

Vasiukov, G., Novitskaya, T., Zijlstra, A., et al. (2020). Myeloid cell-derived TGFβ signaling regulates ECM deposition in mammary carcinoma via adenosine-dependent mechanisms. Cancer Res. *15*, 2628–2638.

Weijing, H., El Botty, R., Montaudon, E., et al. (2021). In vitro bone metastasis dwelling in a 3D bioengineered niche. Biomaterials *269*, 120624.

Yan, T.D., Black, D., Savady, R., et al. (2006). Systematic review on the efficacy of cytoreductive surgery combined with perioperative intraperitoneal chemotherapy for peritoneal carcinomatosis from colorectal carcinoma. J. Clin. Oncol. *24*, 4011–4019.

Zanconato, F., Cordenonsi, M., and Piccolo, S.. (2019). YAP and TAZ: a signalling hub of the tumour microenvironment. Nat. Rev. Cancer *219*, 454–464.

Supplementary Matherial and Methods

Nucleic acids extraction

DNA from FFPE sections of the PM-derived organoids and their tissue of origin was used for mutational analysis. DNA was extracted using the Masterpure Complete DNA Purification Kit (Lucigen-Biosearch Technologies, Middleton, WI, USA) and quantified on the QIAxpert® spectrophotometer (QIAGEN, Hilden, Germany).

DNA from 20 mg of normal peritoneum and PMs, both decellularized and untreated, was used to evaluate the success of the decellularization procedure. DNA was extracted using the DNeasy Blood&Tissue kit (QIAGEN) according to the manufacturer's instructions, and quantified using Nanodrop 1000 (ThermoFisher Scientific) at 260/280 nm ratio. DNA from decellularized ECM, normal peritoneum, PM, and their corresponding non-decellularized samples was loaded onto a 1% agarose gel. The separated bands were visualized by exposing the gel to UV light and images were acquired using Gel Doc (Bio-Rad, Hercules, CA, USA). All of the experiments were performed in triplicate.

RNA from the three organoid cultures (C1, C2 and C3) grown both in Matrigel and on normal or neoplastic peritoneal 3D-dECMs was used for RNA-sequencing (RNA-seq) analyses. For the PM organoids, the Matrigel was digested with Cell Recovery Solution (Corning) as described above. The pellet was washed three times with ice-cold PBS and suspended in 1 ml TRIzol™ reagent (QIAGEN). Instead, for the repopulated 3D-dECMs, the matrices were washed three times with ice-cold PBS and homogenized using the TISSUE Tearor Homogenizer (QIAGEN) in 500 µl TRIzol™ reagent (QIAGEN). Then, RNA was extracted following the manufacturer's instructions, quantified on a ND-1000 spectrophotometer (ThermoFisher Scientific) and stored at -80 °C.

RNA from FFPE sections (10 µm) of the PMs from which the six TDO were derived was used to validate the results from the RNA-seq analysis. RNA was extracted using the miRNeasy FFPE kit (QIAGEN) and quantified on a NanoDrop™ 1000 (ThermoFisher Scientific, Waltham, MA).

Histochemistry (HC), IHC and IF

Before HC and IHC staining, FFPE sections were cut into slices and dewaxed in xylene, rehydrated through decreasing concentrations of ethanol and washed with water. Slices were stained with H&E for quality control. For HC analysis, sections were stained with Masson's trichrome (Aniline blue kit; Bio-Optica), Alcian blue stain (pH 2.5 kit, Bio-Optica), van Gieson trichrome (Bio-Optica), and Periodic Acid Schiff (PAS, Bio-Optica) following the manufacturers' instructions. IHC was performed using the following mouse anti-human antibodies: Ki-67, CK19, CK20, CK AE1/AE3, CDX2, LGR5, vimentin, YAP and TAZ. Images were acquired with a DM6000B microscope (Leica). Staining for Ki-67, CK19, CK20, CK AE1/AE3, CDX2, LGR5 and vimentin antibodies was performed automatically using theAutostainer Link 48 (Dako, Agilent, Santa Clara, CA. US). Antigen retrieval for YAP and TAZ antibodies was carried out using preheated target retrieval solution (pH 6.0) for 30 minutes. Tissue sections were blocked with FBS serum in PBS for 60 min and incubated overnight with primary antibodies. The antibody binding was detected using a polymer detection kit (GAM/GAR-HRP, Microtech) followed by a diaminobenzidine chromogen reaction (Peroxidase substrate kit, DAB, SK-4100; Vector Lab). All sections were counterstained with Mayer's hematoxylin. Dilutions and experimental conditions are listed in Supplementary Table S3. For IF analyses, FFPE sections were stained with Alexa680-conjugated Wheat Germ Agglutinin (WGA) marker (ThermoFisher Scientific) and DAPI (VECTASHIELD Mounting Medium with DAPI**,** Maravai LifeScencies, San Diego, CA, USA), with anti-human Ki-67 and LGR5 monoclonal antibodies, with anti-human Collagen-IV and anti-human monoclonal cCASPASE3 antibodies and DAPI, followed by Alexa488-conjugate goat anti-mouse or Alexa546-conjugated

goat anti-rabbit IgG polyclonal secondary antibodies for 1 hour at RT in dark (ThermoFisher Scientific). Images were acquired with a DM6000B microscope (Wetzlar, Germany Leica,) equipped with a 100 W mercury lamp, and analyzed using Cytovision software (Leica). Dilutions and experimental conditions are listed in Supplementary Table S4.

DNA sequencing

About 150–200 ng genomic DNA (measured with Qubit dsDNA HS assay kit, ThermoFisher Scientific), were sheared by the Sure Select Enzymatic Fragmentation kit (Agilent Technologies Inc., Santa Clara, CA, USA). NGS libraries were created using Sure Select XT2 Low input Custom library probes (Agilent Technologies Inc.). The probe set was custom designed by Cogentech (OncoPan panel) and includes the exonic regions of the following genes: APC, ATM, BARD1, BMPR1A, BRCA1, BRCA2, BRIP1, CDH1, CDKN2A (α and β isoform), CDK4 (exon 2), CHEK2 , CTNNA1, EPCAM , FANCM, MLH1, MSH2, MSH3, MSH6, MUTYH, NBN, NHTL1, PALB2, PMS2, POLD1, POLE, PTEN, RAD51C, RAD51D, SMAD4, STK11, TP53, KRAS, NRAS, BRAF, EGFR, HER2 (ERBB2), and PIK3CA. Sequencing was performed on Illumina MiSeq platform, in PE mode (2 x 150 bp). Raw reads were demultiplexed and aligned to a reference genome (Human GRCh37) using a pipeline developed in-house in collaboration with enGenome Software Company and annotated with the eVai tool. Results were compared to find the percentage of common SNVs (Single Nucletode Variants). Five PM-derived organoids (C1, C2, C3, C4 and C6) and their corresponding surgical samples were analyzed. FFPE tissue for C5, unfortunately,was not available.

Morphological evaluation of the decellularized matrices

3D-dECMs from normal peritoneum and PM lesions were washed twice with 1X PBS and placed in a 60 mm petri dish. Samples were illuminated with a widefield lamp laser to visualize the architecture of the collagen fibers. An image format of 1024x1024 pixels was used and all images were acquired with Leica Application Suite X, ver. 3 software. 3D-dECMs FFPE sections deriving from normal and PM peritoneum were used to perform polarized light microscopy (PLM). FFPEs were analyzed with an Olympus BX63 upright widefield microscope equipped with a motorized stage and a Hamamatsu OrcaAG camera, using Metamorph software. UplanSApo 4X/0.16 N.A objective was used to acquire the mosaics of the sections. Insets were acquired with UplanSApo 10X/0.4 N.A. and UplanSApo 20X/0.75 N.A. objectives. All experiments were perfomed at least in duplicate. Confocal reflection microscopy images were acquired with a Leica TCS SP8 laser confocal scanner mounted on a Leica DMi8 microscope through a HC PL FLUOTAR 20×/0.5 NA.

Nanoscale topographical analysis of 3D-dECMs

The topographical evaluation of the 3D-dECMs was performed by atomic force microscopy (AFM) analysis on samples deriving from normal peritoneum and PM of three different patients. Before the AFM analysis, the 3D-dECM slides were left for 30 minutes at RT to dissolve the optimal cutting temperature (OCT) compound. Then, the samples were carefully washed with ultrapure water and covered with 1X PBS buffer. AFM topographic measurements were carried out at RT using a NanoWizard3 AFM (JPK, Germany) coupled to an Olympus BX61 inverted microscope and equipped with tapping mode silicon ACTG AFM probes (APPNANO). The 50 μm thick tissue slices, instead, were mounted on polarized glass slides (ThermoFisher Scientific), left for 30 minutes at RT and carefully washed with ultrapure water. The topography of each tissue was

characterized by collecting at least 10 areas (5x5 μm^2) of the sample surface with 512×512 points (scan speed 3,5 $\mu m\ s^{-1}$).

ECM component quantification

Total collagen and sulphated glycosaminoglycan (sGAG) content in fresh and decellularized normal and PM peritoneum were quantified using the SIRCOL collagen assay (Biocolor, Carrickfergus, UK) and the Blyscan GAG assay kit (Biocolor), respectively. The experiments were performed in triplicate following the manufacturer's instruction. Data are the mean of three different neoplastic and normal-derived samples obtained from three different donors.

Nanoindentation measurements by AFM

AFM mechanical analysis was carried out on 3D-dECMs deriving from normal peritoneum and PM of five patients. 3D-dECMs were embedded in OCT and frozen with nitrogen-cooled 2-propanol for 10 seconds. Slices of 100 μm thickness were cut with a microtome (Leica) and attached to positively charged poly-lysine coated glass coverslips (ThermoFisher Scientific), exploiting the electrostatic interaction. Nanomechanical tests were performed in liquid on samples covered by a PBS droplet confined by a circular ridge of hydrophobic two-component silicone paste (Leica). A Bioscope Catalyst AFM (Bruker) was used, which was resting on an active anti-vibration base (DVIA-T45, Daeil Systems) and put into an acoustic enclosure (Schaefer). The measurements were performed at RT. Custom monolithic borosilicate glass probes consisting of spherical glass beads (SPI Supplies), with radii R in the range of 7.5–12.5 μm, were attached to tipless cantilevers (Nanosensor, TL-FM) with nominal spring constant k = 3-6 N/m. Probes were fabricated and calibrated, in terms of tip radius, according to an established custom protocol (Indieri et al., 2011). The spring constant was measured using the thermal noise calibration (Hutter and Bechoefer, 1993)

and corrected for the contribution of the added mass of the sphere (Chighizola et al., 2021; Laurent et al., 2013;). The deflection sensitivity was calibrated *in situ* and non-invasively before every experiment by using the previously characterized spring constant as a reference, according to the SNAP procedure described in (Schillers et al., 2017).

The mechanical properties of the 3D-dECMs were obtained by fitting the Hertz model to sets of force versus indentation curves (simply force curves, FCs), as described elsewhere (Schillers et al., 2017; Nebuloni et al., 2016; Puricelli et al., 2015; Shimshoni et al., 2020), to extract the value of the YM of elasticity, which measures ECM rigidity. FCs were collected in Point and Shoot (P&S) mode, selecting the regions of interest from optical images, exploiting the accurate alignment of the optical and AFM images obtained using the Miro software module integrated in the AFM software. Each set of FCs consisted of an array of typically 15x15=225 FCs spatially separated by 5-10 μm, each FC containing 8192 points, with ramp length L = 8-15 μm, maximum load Fmax = 150-1500 nN, and ramp frequency f = 1 Hz. The maximum load was chosen in order to achieve a maximum indentation in the range of 4-9 μm. Typical approaching speed of the probe during indentation was 16-30 μm/s. Five samples were characterized for each condition. In each sample, 3-10 P&S were acquired in macroscopically separated locations, for a total of 10-25 independent P&S per patient and condition (up to 2250-5500 FCs per patient and condition).

Stem cell maintenance, proliferation and apoptosis assays

Growing cells, stem cells and apoptotic cells were detected on FFPE sections. Growing cells, deriving from disaggregated TDO, were stained with anti-human Ki-67 monoclonal antibody (clone MIB-1) and DAPI, and their growth rate was expressed as the percentage of Ki-67-positive cells present in fields devoid of dead cells. Stem cells were stained with anti-human LGR5 monoclonal antibody (clone OTI2A2) and DAPI, and their density was expressed as the percentage of LGR5-

positive cells present in fields devoid of dead cells. Apoptotic cells were stained with anti-human cCASPASE3 monoclonal antibody (clone 9661) and DAPI, and the apoptotic rate was calculated as the percentage of cCASPASE3-positive cells present in the field. The percentage of Ki-67-positive, LGR5-positive and cCASPASE3-positive cells was obtained by dividing the number of positive cell present in one field by the total number of cells in one field, multiplied by 100. Cells in three independent fields (40X magnification) were counted using ImageJ software. The experiments were performed in triplicate using three different neoplastic and normal-derived matrices obtained from three different donors.

Qpath analyses

Percentage estimation and cell counting were performed using Qupath software (https://qupath.github.io, version 0.2.3). The images used for Qpath analyses were acquired using Aperio Leica ScanScope XT (Leica Biosystems, Wetzlar, Germany). The slides were evaluated by an expert pathologist. The percentage of CK AE1/AE3, CK20, CK19, CDX2, Ki-67, and LGR5 positive cells was calculated by dividing the number of positive cells present in each field by the total number of cells in the same field. TDO-derived infiltrating cells were evaluated by calculating the total number of H&E stained cells. Three fields were counted per experiments.

RNA-seq analysis

Gene expression profiles were conducted on C1, C2 and C3 organoid cultures grown in Matrigel and on 3D-dECMs. Total RNA was extracted using TRIzol™ reagent (QIAGEN). Qubit fluorimeter (ThermoFisher Scientific) and Agilent Bioanalyzer 2100 (RIN > 8) were used to measure and assess RNA abundance and integrity, respectively. Indexed library preparation was performed starting with 500 ng total RNA with the TruSeq stranded mRNA (Illumina) according to

the manufacturer's instructions. RNA-seq was performed in PE mode (2x75nt) on an Illumina NextSeq550 platform, generating an average of 55 million PE reads per sample. For every condition (Matrigel, normal 3D-dCM and neoplastic 3D-dECM), two replicates per organoid were sequenced, for a total of 18 data points. Raw reads were aligned to the human transcriptome (hg38) with STAR (Dobin et al., 2013) using the quantMode option to generate transcripts counts. Differentially expressed genes in the three growth conditions were identified with DESeq2 (Alshehri, 2018). All *p*-values were adjusted for false discovery rate with the Benjamini-Hochberg method.

Gene Set Enrichment Analysis

Gene Set Enrichment Analysis was performed with the enrichR R package (Chen et al., 2013) on deregulated genes (absolute fold change > 2 and adjusted *p*-value <0.05). In particular, the enrichment for the Matrisome database was assessed. This database provides live cross-referencing to gene and protein databases for every ECM and ECM-associated gene, also integrating experimental proteomic data on ECM and ECM-associated proteins and genes from the ECM Atlas (Naba et al., 2016). Gene sets with adjusted *p*-value <0.05 were considered significantly enriched.

Quantitative real-time polymerase chain reaction (qRT-PCR)

For gene expression analysis, cDNA was synthesized from 100 ng of total RNA using a High-Capacity cDNA Reverse Transcription Kit (ThermoFisher Scientific, Waltham, MA) and qPCR was carried out with gene-specific assays for MT1A (Hs00831826_s1), LOX (Hs00942480_m1), THY1 (Hs00174816_m1), FZD9 (Hs00268954_s1), SPP1 (Hs00959010_m1), and performed using the TaqMan FAST Universal PCR Master Mix, no AmpErase® UNG in a PRISM 7900HT Real-Time PCR system (Thermo Fisher Scientific). The expression values of the genes were normalized to GAPDH (Hs99999905_m1).

Dose-response curves for HIPEC treatment

To determine the IC_{50} value of MMC and OXA, $5x10^3$ C1, C2 and C3 TDO were suspended in 100 µl of culture medium and seeded on 96-well plates (Costar 3904; Corning, New York, USA) coated with 40 µl of Matrigel. TDO were dispensed on the top of the matrigel. After two days, TDO were incubated with 100 µl preheated drug at concentrations ranging from 2.5 to 200 µM for MMC and between 10 and 700 µM for OXA, for 60 min (MMC) or 90 min (OXA) at 42.5 °C. The values were chosen by scaling up and down the concentrations used for patients (35 mg/m^2 for MMC and 200 mg/m^2 for OXA, which correspond to 41.9µM for MMC and 252 µM for OXA for *in vitro* treatments (Ubink et al., 2019). TDO viability, was assessed using a CellTiterGlo® 2.0 kit (Promega, Fitchburg, Wisconsin, USA) on a TECAN spark microplate reader (Tecan Trading AG, Switzerland). Viability was normalized to the mean of three control samples/plate (TDO treated with 0.5 % DMSO in MMC and physiological solution in OXA experiments). All the experiments were performed in triplicate.

Immunoblotting

After HIPEC simulation using drugs at a concentration corresponding to the IC_{50} value of each TDO, C1, C2, and C3 TDO were lysed in Ripa buffer (50 mM Tris, pH 8.0, 50 mM NaCl, 0.5% Triton X-100, 0.1% sodium deoxycholate, 0.25% sodium dodecyl sulphate [SDS]) supplemented with protease inhibitors (Merck Millipore, Billerica, MA, USA) and a phosphatase inhibitor cocktail (Sigma-Aldrich, St. Louis, MO, USA), for 3 h at 4 °C on a rotation wheel. Samples were then sonicated and their protein content was quantified using the Bradford protein assay (Bio-Rad, Hercules, CA, USA). For each sample, 40 µg of protein extract were separated on 4–12% polyacrylamide gels, transferred onto nitrocellulose membranes (Sigma-Aldrich, St. Louis, MO, USA) and incubated with primary antibodies (Supplementary Table S4). The signals were detected

using enhanced chemiluminescence, and protein levels were quantified using Imagelab software (Bio-Rad, Hercules, CA, USA). Each experiment was repeated at least three times.

Statistical analyses

Statistical analyses were performed using GraphPad Prism software (version 8.4.1 (676), GraphPad Software, San Diego, USA). Data are expressed as mean and SEM. A two-tailed Student's t test was used to compare paired groups. Differences among groups were evaluated using two-way ANOVA. In the case of AFM mechanical experiments, for each patient and each condition tested, the median values of the YM were extracted from each measured location (P&S) using the procedure described in Cramer et al (Shimshoni et al., 2020; Cramer, 1999). The distributions of the measured YM values were obtained by grouping all P&S measured in all locations, for each patient and each condition tested. The mean and median values and the corresponding standard deviations of the mean (as SEM) were calculated by averaging between P&S. The statistical significance of differences between normal and neoplastic conditions was estimated by applying the two-tailed *t* test. A p-value <0.05 was considered statistically significant.

References

Alshehri H.A.N. (2018). Compare and Contrast of Differential Gene Expression Software Packages of RNA-Seq.*Computational Science and Computational Intelligence (CSCI)*. Las Vegas, NV, USA: IEEE.

Butt H.J. , Jaschke M. (1995). Calculation of thermal noise in atomic force microscopy. *Nanotechnology* 6, 1.

Chen E.Y. , Tan C.M. , Kou Y. , *et al*. (2013). Enrichr: interactive and collaborative HTML5 gene list enrichment analysis tool. *BMC Bioinformatics* 14, 128.

Chighizola M. , Puricelli L. , Bellon L. , Podestà A. (2021). Large colloidal probes for atomic force microscopy: Fabrication and calibration issues. *J*. *Mol*. *Recognit*. 34, e2879.

Cramer H. (1999). Mathematical methods of statistics. *Princeton University Press* 1999.

Dobin A. , Davis C.A. , Schlesinger F. , *et al*. (2013). STAR: ultrafast universal RNA-seq aligner *Bioinformatics*. 29, 15-21.

Hutter J.L. , Bechhoefer J. (1993). Calibration of atomic-force microscope tips. *Rev*. *of Sci*. *Intrum*. 64, 1-5.

Indrieri M. , Podestà A. , Bongiorno G. , *et al*. (2011). Adhesive-free colloidal probes for nanoscale force measurements: production and Characterization. *Rev*. *Sci Instrum*. 82, 50-62.

Laurent J. , Steinberger A. , Bellon L. (2013). Functionalized AFM probes for force spectroscopy: eigenmode shapes and stiffness calibration through thermal noise measurements. *Nanotechnology* 7, 225504.

Naba A. , Clauser K.R. , Ding H. , *et al*. (2016). The extracellular matrix: Tools and insights for the "omics" era. *Matrix Biol*. 49, 10-24.

Nebuloni M. , Albarello L. , Andolfo A. , *et al*. (2016). Insight On Colorectal Carcinoma Infiltration by Studying Perilesional Extracellular Matrix. *Sci*. *Rep*. 4, 22522.

Puricelli L. , Galluzzi M. , Schulte C. , *et al*. (2015). Nanomechanical and topographical imaging of living cells by atomic force microscopy with colloidal probes. *Rev*. *Sci*. *Instrum*. 86, 033705.

Schillers H. , Rianna C. , Schäpe J. , *et al*. (2017). Standardized Nanomechanical Atomic Force Microscopy Procedure (SNAP) for Measuring Soft and Biological Samples. *Sci*. *Rep*. 11, 5117.

Shimshoni E. , Adir I. , Afik R. , *et al*. (2020). Distinct extracellular-matrix remodeling events precede symptoms of inflammation. *Matrix Biol*. s0945-053X, 30103-30107.

Ubink I. , Bolhaqueiro A.C.F. , Elias S.G. , *et al*. (2019). Organoids from colorectal peritoneal metastases as a platform for improving hyperthermic intraperitoneal chemotherapy. *Br*. *J*. *Surg*. 106, 1404-1414.

Supplementary Table S1

ID	Gender	Diagnosis	Grade	Mutations	Microsatellite	Chemotherapy	PM Organoid line
S07-7576	F	Moderately differentiated infiltrating adenocarcinoma	pT3G2	G12S KRAS;TP53	MSS	None	C1
S11-2361	M	Poorly differentiated mucinous multiple intestinal adenocarcinoma	pT4G3	V600E BRAF; TP53	MSS	None	C2
S16-8598	F	Intestinal mucinous adenocarcinoma	pT4G3N2	G12S KRAS; TP53; FGFR1 amplification	MSS	Yes	C3
S17-3963	F	Moderately differentiated adenocarcinoma	T4aG3N2aM1b	G12S KRAS	MSS	None	C4
S17-3610	M	Intestinal adenocarcinoma with mucinous component	pT4aG2N0Mx	G12S KRAS	MSS	None	C5
S18-8607	M	Colloidal / gelatinous mucinous adenocarcinoma associated with hairy adenocarcinoma of high and low grade	T4aN2bG3Mx	G12S KRAS; TP53	MSS	Yes	C6

Supplementary Table S1: The main pathological characteristics of the patients from whom the tumor specimens were obtained.

Supplementary Table S2

Factor	Description	Vendor	Working Concentration
Gentamicin	Antibiotic	ThermoFisher Scientific	50 ng/ml
HEPES	Buffer	ThermoFisher Scientific	10 mM
L-Glutamine (GlutaMAX)	Cell culture supplement	ThermoFisher Scientific	2 mM
B27	Cell culture supplement	ThermoFisher Scientific	1:50
Gastrin-1, recombinant human	Recombinant protein	Sigma Aldrich	10 nM
N-acetylcysteine	Colonic niche factor	Wako	1 mM
EGF, recombinant human	Recombinant protein	ThermoFisher Scientific	50 ng/ml
Noggin, recombinant human	Recombinant protein	Preprotech	100 ng/ml
R-spondin-1, recombinant human	Recombinant protein	Preprotech	100 ng/ml
Wnt3A, recombinant human	Recombinant protein	Preprotech	50 ng/ml
Prostaglandin E2	Colonic niche factor	Tocris	100 nM
A83-01	p38 inhibitor	Tocris	500 nM
SB202190	ROCK inhibitor	Sigma Aldrich	10 μM

Supplementary Table S2: The complete list of growth factors, media supplements and concentrations used for PM-derived organoid cultures.

Supplementary Table S3

Organoid culture	Medium composition
C1	DMEM-F12; B27; Glutamax; N-acetylcysteine; prostaglandin-E2; gastrin-I
C2	DMEM-F12; B27; Glutamax
C3	DMEM-F12; B27; Glutamax; N-acetylcysteine; prostaglandin-E2; gastrin-I; A83-01
C4	DMEM-F12; B27; Glutamax; N-acetylcysteine; prostaglandin-E2; gastrin-I; EGF; A83-01; Noggin
C5	DMEM-F12; B27; Glutamax; N-acetylcysteine; prostaglandin-E2; gastrin-I; A83-01; SB202190; Noggin
C6	DMEM-F12; B27; Glutamax; N-acetylcysteine; prostaglandin-E2; gastrin-I; A83-01; Noggin

Supplementary Table S3: The specific media composition for each PM-derived organoid culture.

Supplementary Table S4

Antigen (human)	Host	Clone	Vendor	Dilution	Antigen retrieval solution
Ki-67	Mouse	MIB-1	Dako	1:400	5 mM EDTA (pH 8), 10 min, 96 °C
CK19	Mouse	A53-B/A2	Dako	1:1000	5 mM EDTA (pH 8), 15 min, 96°C
CK20	Mouse	Ks20.8	Dako	1:500	5 mM EDTA (pH 8), 30 min, 96°C
CK AE1/AE3	Mouse	AE1+AE3	Dako	1:100	10 mM Citrate (pH 6), 15 min, 96°C
CDX2	Mouse	CDX2_88	Dako	1:50	5 mM EDTA (pH 8), 30 min, 96°C
LGR5	Mouse	OTI2A2	Origene	1:250	10 mM Citrate (pH 6), 15 min, 96 °C
Vimentin	Mouse	V9	Dako	1:400	10 mM Citrate (pH 6), 15 min, 96°C
Collagen-IV	Rabbit	CIV-22	Abcam	1:200	5 mM EDTA (pH 8), 10 min, 96 °C
cCASPASE3	Rabbit	#9661	Cell Signaling	1:250	10 mM Citrate (pH 6), 15 min, 96 °C
TAZ	Rabbit	WWTR1	Sigma	1:100	10 mM Citrate (pH 6), 15 min, 96 °C
YAP	Mouse	63.7	Santa Cruz	1:100	10 mM Citrate (pH 6), 15 min, 96 °C

Supplementary Table S4: The primary antibodies and the experimental conditions used for IHC and IF analyses.

Supplementary Table S5

Antigen (human)	Vendor	Host	Code	MW	Dilution
Vinculin	Sigma	Mouse	V9131	116 kDa	1:10000 in 5% MILK
Cleaved PARP (Asp214)	Cell Signaling	Rabbit	9541S	89 kDa	1:1000 in 5% MILK
p-p53 (Ser15)	Cell Signaling	Rabbit	9284S	53 kDa	1:1000 in 5% MILK
p53	Santa Cruz	Mouse	sc-126	53 kDa	1:1000 in 5% MILK
Caspase-3	Cell Signaling	Rabbit	9662	35, 19, 17 kDa	1:1000 in 5% BSA
Cleaved Caspase-3 (Asp175)	Cell Sigaling	Rabbit	9661S/L	17, 19 kDa	1:1000 in 5% MILK
p-Histone H3(Ser10 Thr11)	Abcam	Rabbit	Ab 32107	17 kDa	1:2500 in 5% BSA
p-H2AX (Ser139)	Upstate, Millipore	Mouse	05-636	17 kDa	1:1000 in 5% MILK
H2AX	Abcam	Rabbit	Ab11175	15 kDa	1:5000 in 5% MILK

Supplementary Table S5: The primary antibodies and the experimental conditions used for WB analyses.

Supplementary Figure S1

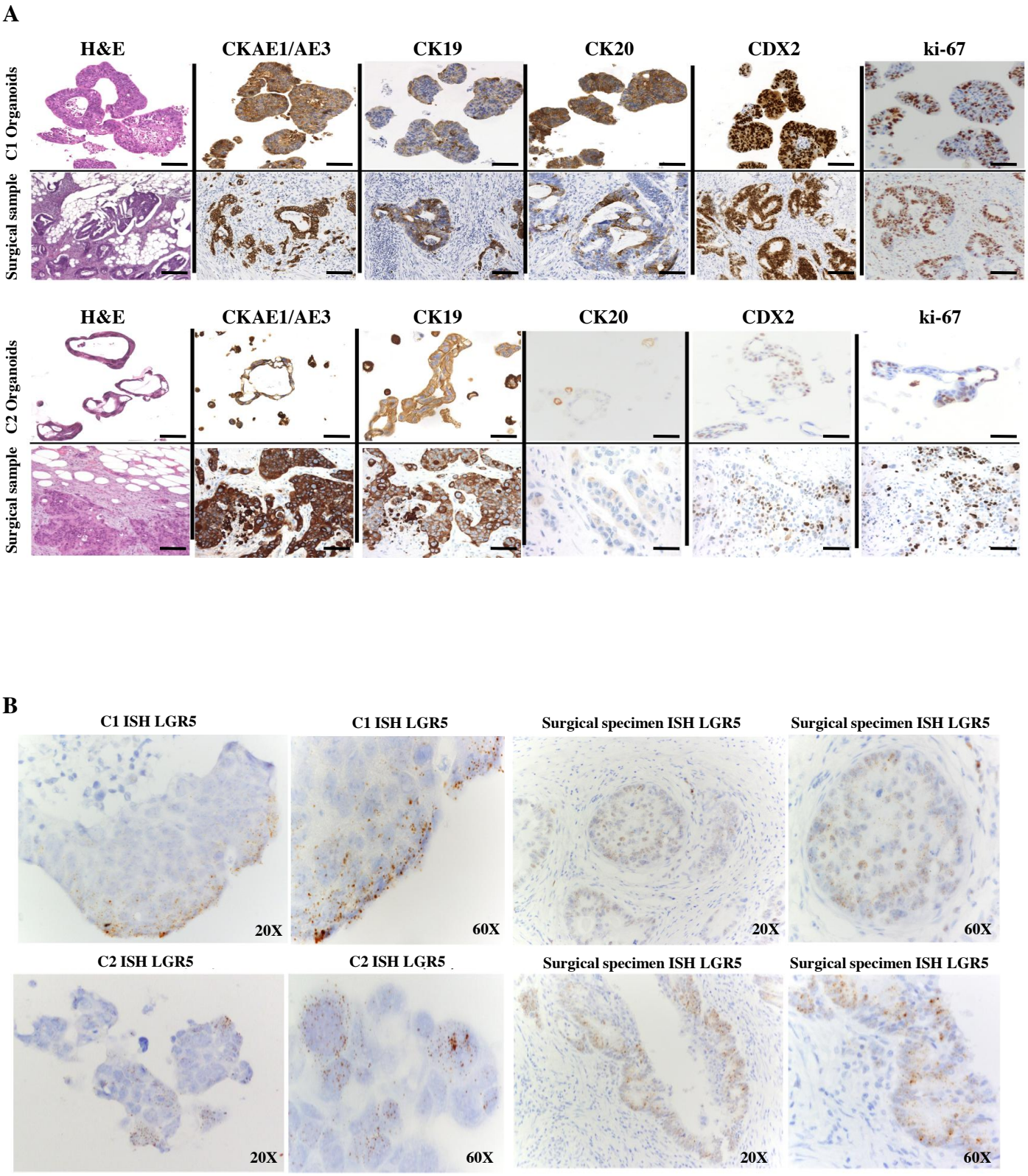

Supplementary Fig. S1. (A) IHC analysis of C1 and C2 organoids and their corresponding surgical samples, using H&E staining and CK AE1/AE3, CK19, CK20, CDX2 and Ki-67 immunostaining (20X magnification). The images were previously published by Bozzi et al. [11]. **(B)** In situ hybridization (ISH) of C1 and C2 organoids and corresponding surgical samples, using LGR5 immunostaining (20X magnification). The images were previously published [11].

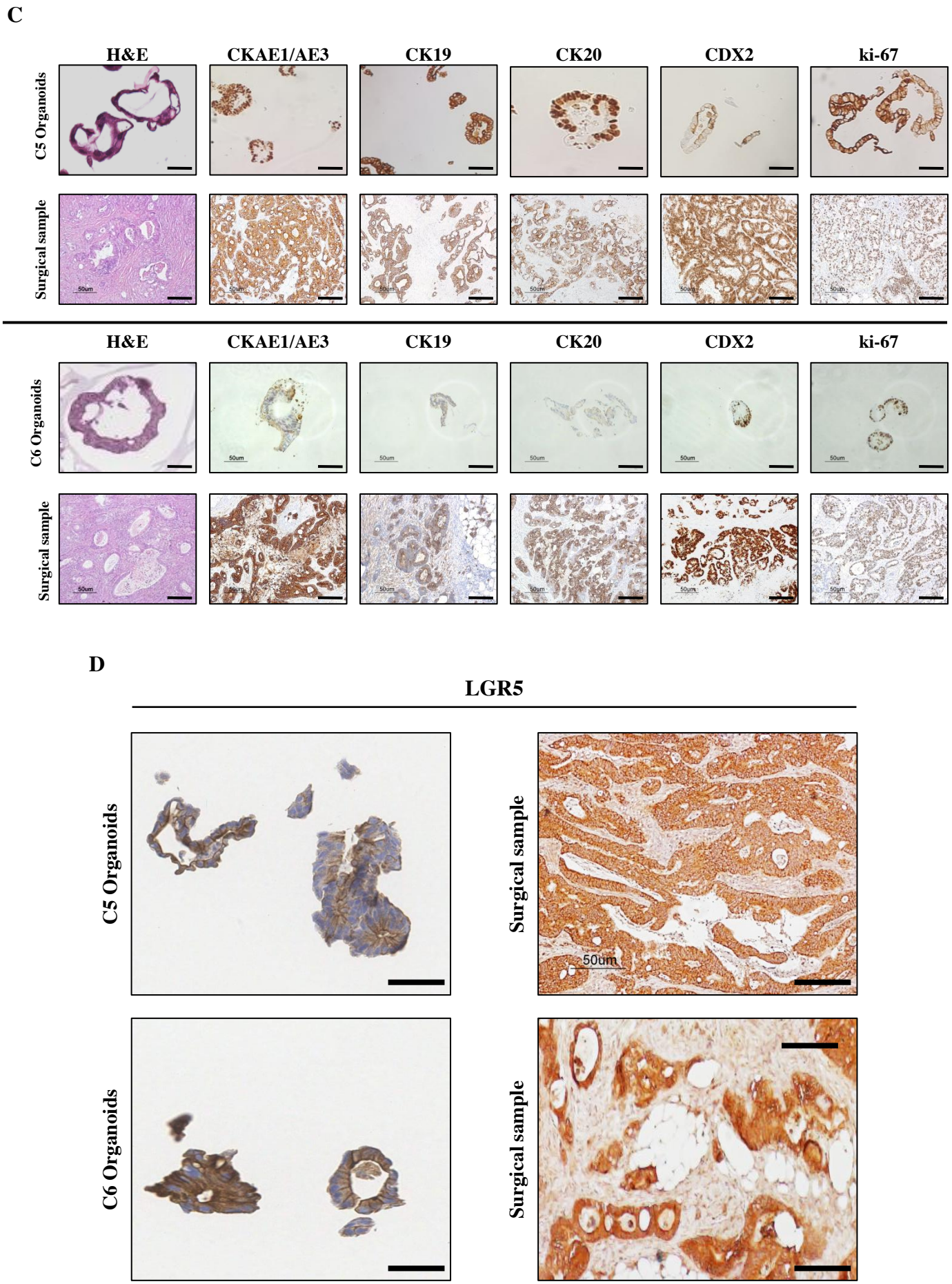

Supplementary Fig. S1. (C) H&E staining and CK AE1/AE3, CK19, CK20, CDX2, and Ki-67 immunostaining of C5 and C6 organoid cultures and their corresponding surgical samples. Scale bar: 50 µm. **(D)** IHC analysis of C5 and C6 organoid cultures and their tumor of origin, using LGR5 immunostaining. Scale bar: 50 µm.

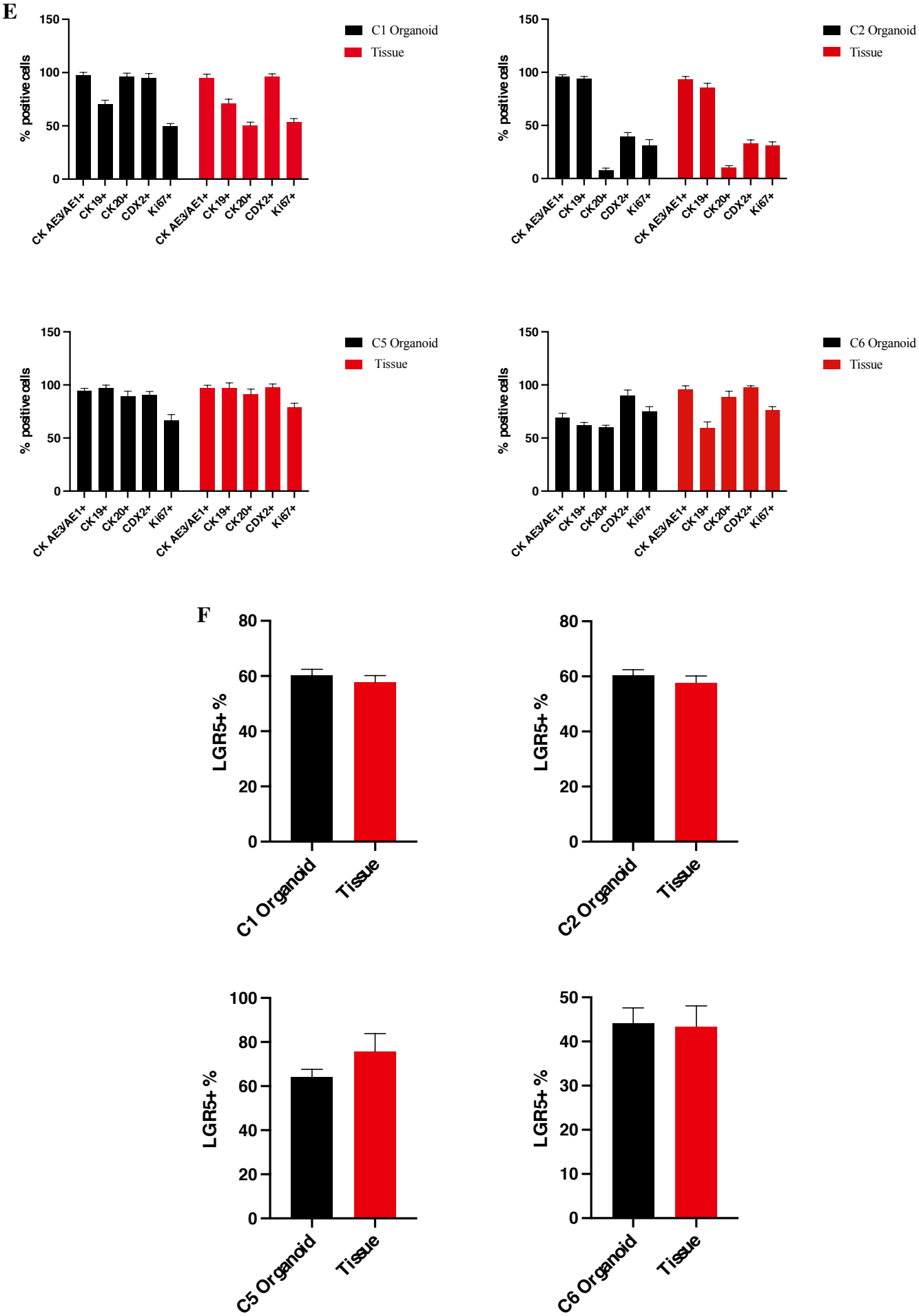

Supplementary Fig. S1. (E) Quantitative counts of the percentage of CK AE/AE3, CK19, CK20, CDX2 and Ki-67 positive cells in C1, C2, C5 and C6 PM-derived organoids Vs their corresponding tumor of origin. Three fields per experiments were counted using Qpath software. Data are presented as median and SD. One-way ANOVA did not show differences between the two groups. **(F)** Quantitative counts of the percentage of LGR5 positive cells in C1, C2, C5 and C6 PM-derived organoids Vs their corresponding tumor of origin. Three fields per experiments were counted using Qpath software. Data are presented as median and SD. One-way ANOVA did not show differences between the two groups.

G

Genes	C1 Organoid	Tissue of origin
MSH3 (A62P)		
BRCA2 (G267Q)		
BRCA2 (S2414S)		
POLE (L1903L)		
PMS2 (S260S)		
BRCA2 (K1132K)		
RAD51C (D253H)		
POLE (A252V)		
BRCA2 (V2466A)		
ATM (D1853N)		
BRCA1 (E1038G)		
BRCA2 (V2171V)		
EGFR (N158N)		
ERBB2 (A356D)		
BRCA1 (S694S)		
BRCA1 (K1183R)		
BRCA1 (L771L)		
BRCA1 (D693N)		
BRCA1 (P871L)		
BRCA1 (S1436S)		
BRIP1 (Y1137Y)		
EGFR (T629T)		
BRCA1 (S1613G)		
KRAS (R161R)		
ATM (N1983S)		
BRCA1 (S1040N)		
ERBB2 (P1140A)		
POLD1 (K738N)		
MSH3 (E949R)		
BRCA2 (L1521L)		
EGFR (A613A)		
MSH6 (G39Q)		
BRIP1 (Q879Q)		
TP53 (R213R)		
BRIP1 (S919P)		
CDH1 (A692A)		
EGFR (T903T)		
KRAS (Q61H)		
POLE (A1510A)		
POLE (T1052T)		
POLE (S2084S)		
BARD1 (H506H)		
APC (S1411S)		
TP53 (P72R)		
EGFR (Q787Q)		
TP53 (R175H)		
BARD1 (T351T)		
PMS2 (K541E)		

% of Similarity: 97.92 %

Genes	C2 Organoid	Tissue of origin
MSH2 (L556L)		
PALB2 (T1100T)		
BMPR1A (P2T)		
PALB2 (E559R)		
APC (E260)		
MLH1 (I219V)		
APC (T1556fs)		
PMS2 (V280V)		
PALB2 (G998Q)		
MSH6 (D180D)		
MSH6 (P92P)		
POLD1 (T495T)		
PIK3CA (I391M)		
CTNNA1 (L180L)		
MSH6 (R62R)		
BRCA2 (V2466A)		
KRAS (R162R)		
BARD1 (A40V)		
MSH3 (I78V)		
BRCA2 (V1269V)		
PALB2 (E672Q)		
FANCM (I1460V)		
ATM (S1270C)		
BRCA2 (I3412V)		
BRAF (G643G)		
BRCA2 (V2171V)		
MSH3 (Q949R)		
FANCM (V878L)		
ATM (N1983S)		
EGFR (T629T)		
BRAF (V600E)		
ATM (D1853N)		
MSH3 (A1045T)		
POLE (P1548T)		
BRCA2 (L1521L)		
CTNNA1 (S740S)		
EGFR (T903T)		
FANCM (S175F)		
BRIP1(E879E)		
NBN (D399D)		
BARD1 (P24S)		
CDH1 (A692A)		
BARD1 (H506H)		
TP53 (R273H)		
PMS2 (K541E)		
EGFR (Q787Q)		
EGFR (R521K)		
FANCM (P1812A)		
TP53 (P72R)		

% of Similarity: 91.84 %

Supplementary Fig. S1. (G) List of the gene mutations acquired in the TDOs compared to the tumor of origin (red boxes). The percentage of similarity is also reported. Passage numbers of the organoid lines were: C1: P11; C2: P13; C3: P10; C4: P14; C6: P10.

G

Genes	C3 Organoid	Tissue of origin
PMS2 (K541E)		
PMS2 (P470S)		
PMS2 (S260S)		
TP53 (R273C)		
TP53 (P72R)		
CDKN2A (A148T)		
PALB2 (V932M)		
KRAS (R161R)		
BRCA2 (N372H)		
BRCA2 (K1132K)		
BRCA2 (L1521L)		
BRCA2 (V2171V)		
BRCA2 (S2414S)		
BRCA2 (V2466A)		
RAD51D (R24R)		
ERBB2 (I625V)		
ERBB2 (P1104A)		
BRCA1 (S1613G)		
BRCA1 (S1436S)		
BRCA1 (K1183R)		
BRCA1 (E1038G)		
BRCA1 (P871L)		
BRCA1 (L771L)		
BRCA1 (S694S)		
BRCA1 (D693N)		
FANCM (S175F)		
FANCM (V878L)		
FANCM (I1460V)		
FANCM (I1742V)		
FANCM (P1812A)		
MSH6 (R62R)		
MSH6 (P92P)		
MSH6 (D180D)		
EGFR (N158N)		
EGFR (T903T)		
BRIP1 (Y1137Y)		
BRIP1 (S919P)		
BRIP1 (E879E)		
CDH1 (A692A)		
MSH3 (A55Adel)		
MSH3 (A61Pdup		
MSH3 (P67P69del)		
MSH3 (I79V)		
MSH3 (Q949R)		
MSH3 (A1045T)		
BMPR1A (P2T)		
NBN (P672P)		
NBN (D399D)		
NBN (E185Q)		
NBN (L34L)		
ATM (N1983S)		
APC (Q480)		
APC (D774D)		
APC (I1417fs)		
APC (V1822D)		
POLE (S2084S)		
POLE (A1510A)		
POLE (T1052T)		
CTNNA1 (A179V)		
PIK3CA (Q546R)		

% of Similarity: 100 %

Genes	C4 Organoid	Tissue of origin
KRAS (R161R)		
KRAS (G12S)		
BRCA2 (K1132L)		
BRCA2 (L1521L)		
BRCA2 (T1915M)		
BRCA2 (V2171V)		
BRCA2 (S2414)		
BRCA2 (V2466A)		
MSH6 (R62R)		
MSH6 (P92P)		
MSH6 (D180D)		
MSH6 (R1034Q)		
SMAD4 (D351N)		
POLD1 (T495T)		
EGFR (T903T)		
EGFR (D994D)		
BRIP1 (Y1137Y)		
BRIP1 (S919P)		
BRIP1 (E879E)		
CDH1 (T379M)		
CDH1 (A692A)		
MSH3 (A55A60del)		
MSH3 (P67P69del)		
MSH3 (I79V)		
MSH3 (Q949R)		
BMPR1A (P2T)		
ATM (N1983S)		
APC (Y486Y)		
APC (A545A)		
APC (S835fs)		
APC (L1488)		
APC (T1493T)		
APC (G1678G)		
APC (S1756S)		
APC (V1822D)		
APC (P1960P)		
POLE (S2084S)		
BRAF (G643G)		
BARD1 (V507M)		

% of Similarity: 87.18 %

Supplementary Fig. S1. (G) List of the gene mutations acquired in the TDOs compared to the tumor of origin (red boxes). The percentage of similarity is also reported. Passage numbers of the organoid lines were: C1: P11; C2: P13; C3: P10; C4: P14; C6: P10.

G

Genes	C6 organoid	Tissue of origin
PMS2 (P470S)		
PMS2 (S260S)		
TP53 (G245V)		
TP53 (P72A)		
CDKN2A (A148T)		
KRAS (R161R)		
KRAS (G12A)		
BRCA2 (N372H)		
BRCA2 (K1132K)		
BRCA2 (L1521L)		
BRCA2 (T1915M)		
BRCA2 (V2171V)		
BRCA2 (S2414S)		
BRCA2 (V2466A)		
RAD51D (R145C)		
MLH1 (I219V)		
ERBB2 (P1140A)		
BRCA1 (S1613G)		
BRCA1 (S1436S)		
BRCA1 (K1183R)		
BRCA1 (E1038G)		
BRCA1 (P871L)		
BRCA1 (L771L)		
BRCA1 (S694S)		
MUTYH (S515F)		
MUTYH (Q338H)		
MSH6 (R62R)		
MSH6 (P92P)		
MSH6 (D180D)		
MSH6 (Y214Y)		
SMAD4 (D315H)		
EGFR (N158N)		
EGFR (R521K)		
EGFR (Q787Q)		
EGFR (R836R)		
EGFR (T903T)		
BRIP1 (Y1137Y)		
BRIP1 (S919P)		
BRIP1 (E879E)		
CDH1 (A692A)		
MSH3 (A55A60del)		
MSH3 (P67P69del)		
MSH3 (I79V)		
MSH3 (Q949R)		
MSH3 (A1045T)		
BMPR1A (P2T)		
ATM (D1853N)		
ATM (N1983S)		
APC (Y486Y)		
APC (A545A)		
APC (L1129S)		
APC (Q1406fs)		
APC (T1493T)		
APC (G1678G)		
APC (S1756S)		
APC (V1822D)		
APC (P1960P)		
POLE (S2084S)		
POLE (A1510A)		
POLE (N1396S)		
POLE (T1052T)		
CTNNA1 (S740S)		
BRAF (G643G)		
BARD1 (H506H)		
BARD1 (T351T)		

% of Similarity: 93.85 %

Supplementary Fig. S1. (G) List of the gene mutations acquired in the TDOs compared to the tumor of origin (red boxes). The percentage of similarity is also reported. Passage numbers of the organoid lines were: C1: P11; C2: P13; C3: P10; C4: P14; C6: P10.

Supplementary Figure S2

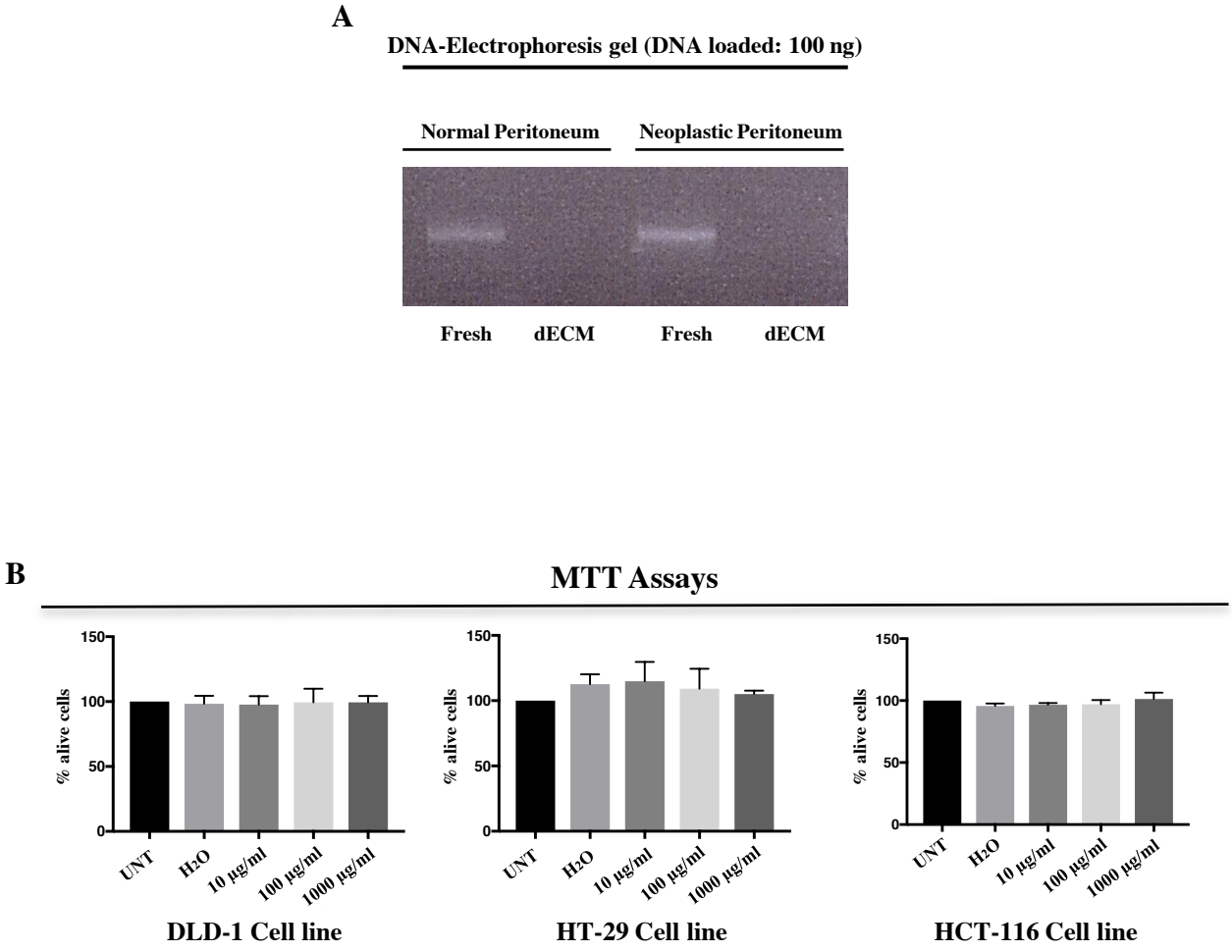

Supplementary Fig. S2. (A) To confirm the efficacy of the decellularization treatment, the loss of DNA content was assessed. DNA was extracted from 20 mg of non-decellularized or decellularized ECM and quantified with the Nanodrop instrument. Ten µl of DNA from PM or dECM were loaded onto a 1% agarose gel and the images were acquired using Gel Doc (Biorad). The results showed the absence of DNA in dECM samples, indicating the success of the decellularization procedure. The experiments were performed in triplicate. **(B)** Assessment of whether the components and procedures of the decellularization protocol can influence cell viability. CRC-derived DLD-1, HT-29 and HCT-116 cell lines were obtained from the American Type Culture Collection (ATCC, Rockville, MD, USA) and were authenticated by the Cell Culture Facility at the FIRC Institute of Molecular Oncology (IFOM, Milan, Italy) with the StemElite ID system (Promega). Cells were routinely tested for mycoplasma and cultured following the recommended ATCC's protocols. The 3D-dECMs were placed at − 80 °C overnight, lyophilized using freeze-drier cycles following standard procedures, and then added to the culture media of the three cell lines. During the experiments, three different concentrations of lyophilized 3D-dECMs were tested and cell viability was evaluated after 72 hours of growth by MTT (3-(4, 5-dimethylthiazol-2-yl)-2, 5-diphenyltetrazolium bromide) assay (Sigma Aldrich), following the manufacturer's instructions. The results showed no differences in cell viability between cells cultured with or without lyophilized ECM, highlighting that the decellularization procedure is safe for cell growth. The experiments were performed in duplicate**.**

Supplementary Figure S3

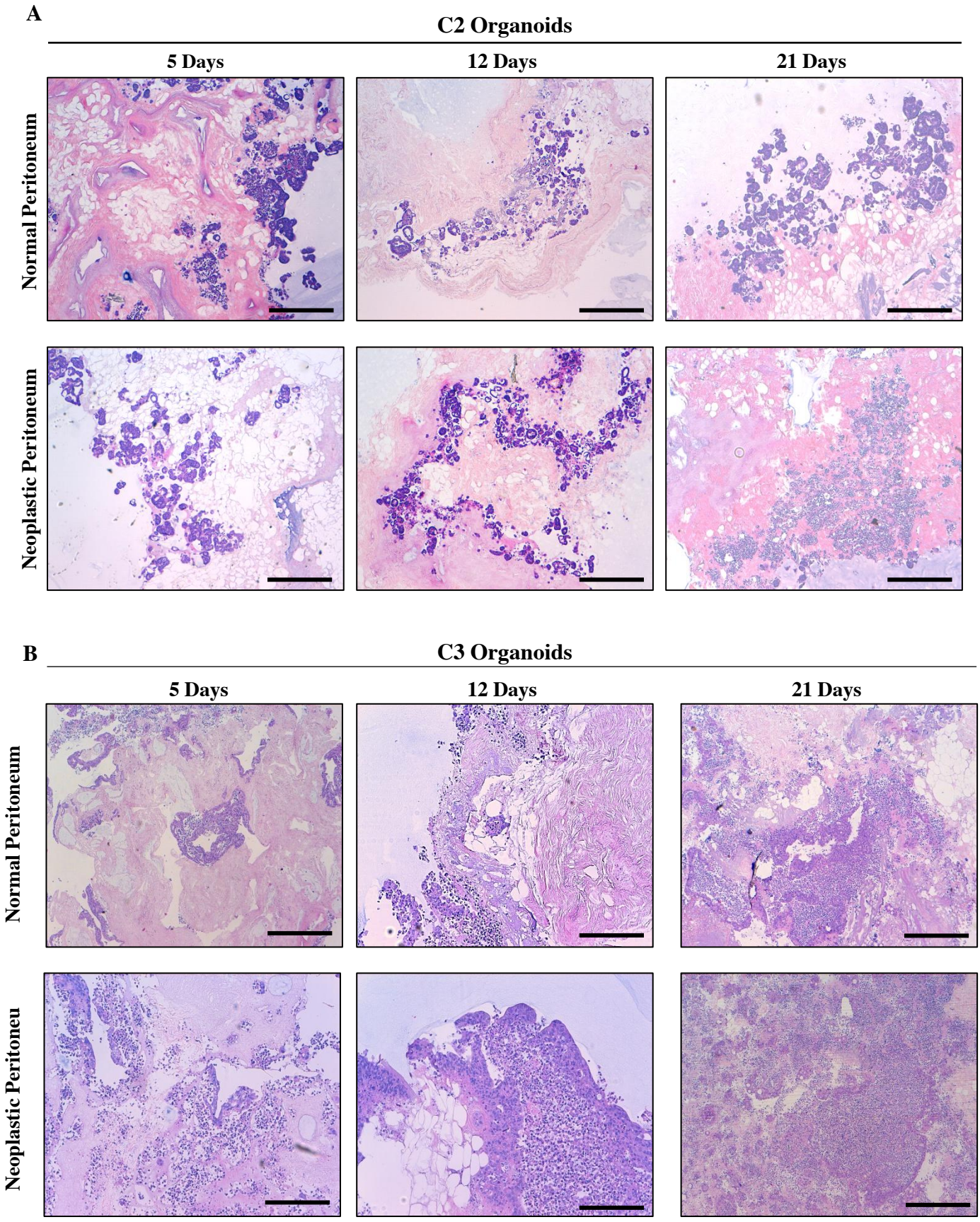

Supplementary Fig. S3. (A) H&E staining of decellularized matrices derived from normal (top) or neoplastic (bottom) peritoneum repopulated with PM-derived organoids (C2) at three different time points as indicated. Scale bar: 100 µm. The repopulation experiments were performed in triplicate. **(B)** H&E staining of decellularized matrices derived from normal (top) or neoplastic (bottom) peritoneum repopulated with PM-derived organoids (C3) on day 12. Scale bar: 100 µm. The repopulation experiments were performed in triplicate.

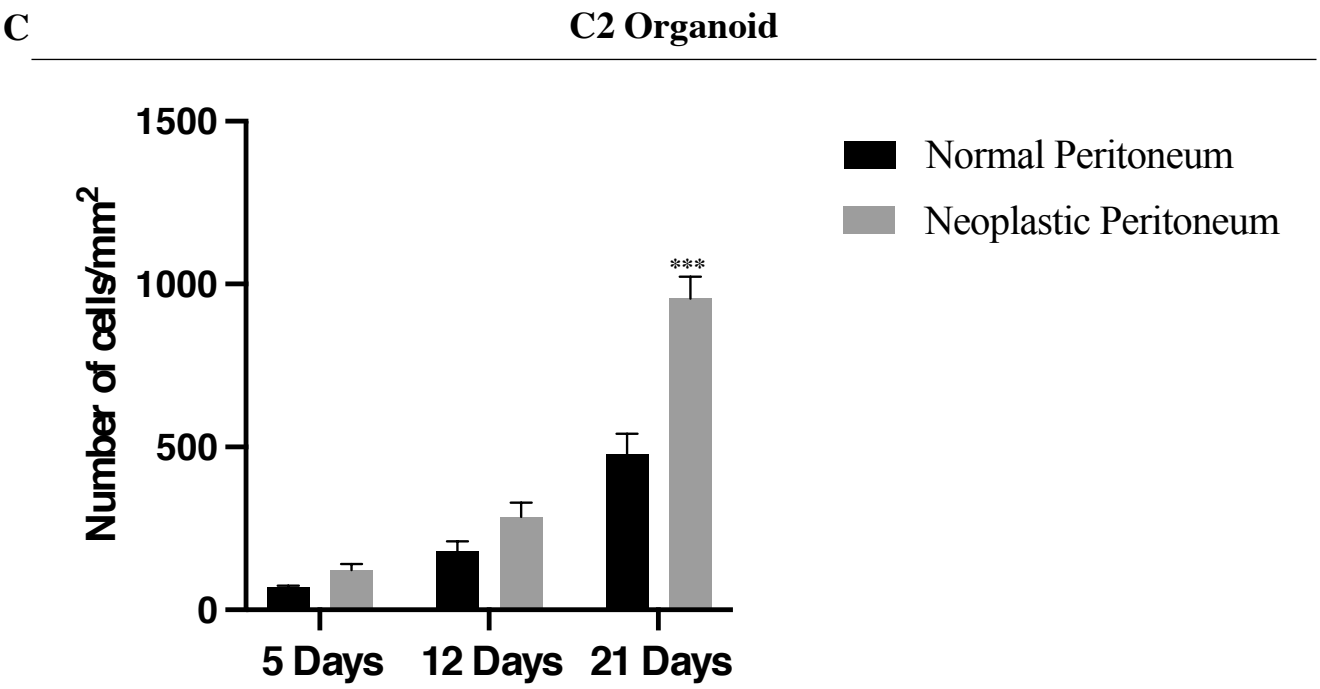

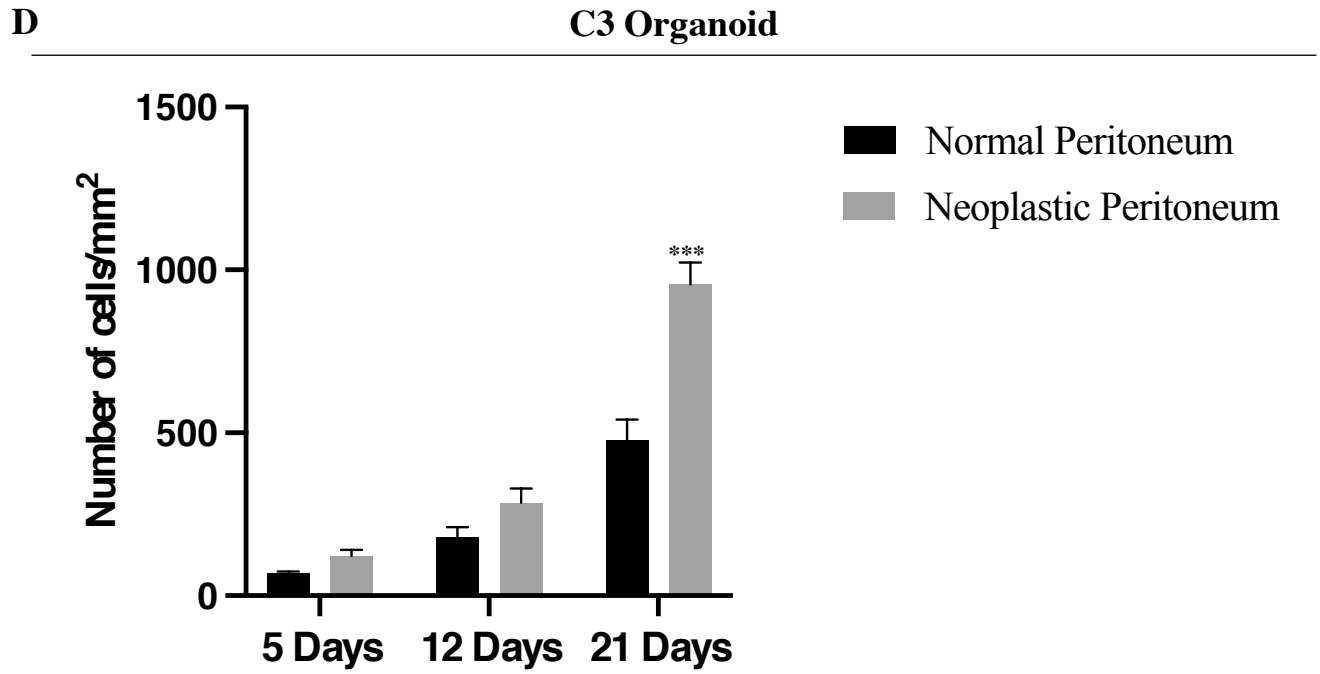

Supplementary Fig. S3. (C) Number of C2 PM-organoid derived cells grown onto normal and neoplastic-derived 3D-dECM per mm^2 after 5, 12 and 21 days. Three fields per experiments were counted using Qpath software. Data are presented as median and SD. One-way ANOVA (***p<0.001). **(D)** Number of C3 PM-organoid derived cells grown onto normal and neoplastic-derived 3D-dECM per mm^2 after 5, 12 and 21 days. Three fields per experiments were counted using Qpath software. Data are presented as median and SD for surgical specimens of three patients. One-way ANOVA (***p<0.001). The repopulation experiments were performed in triplicate.

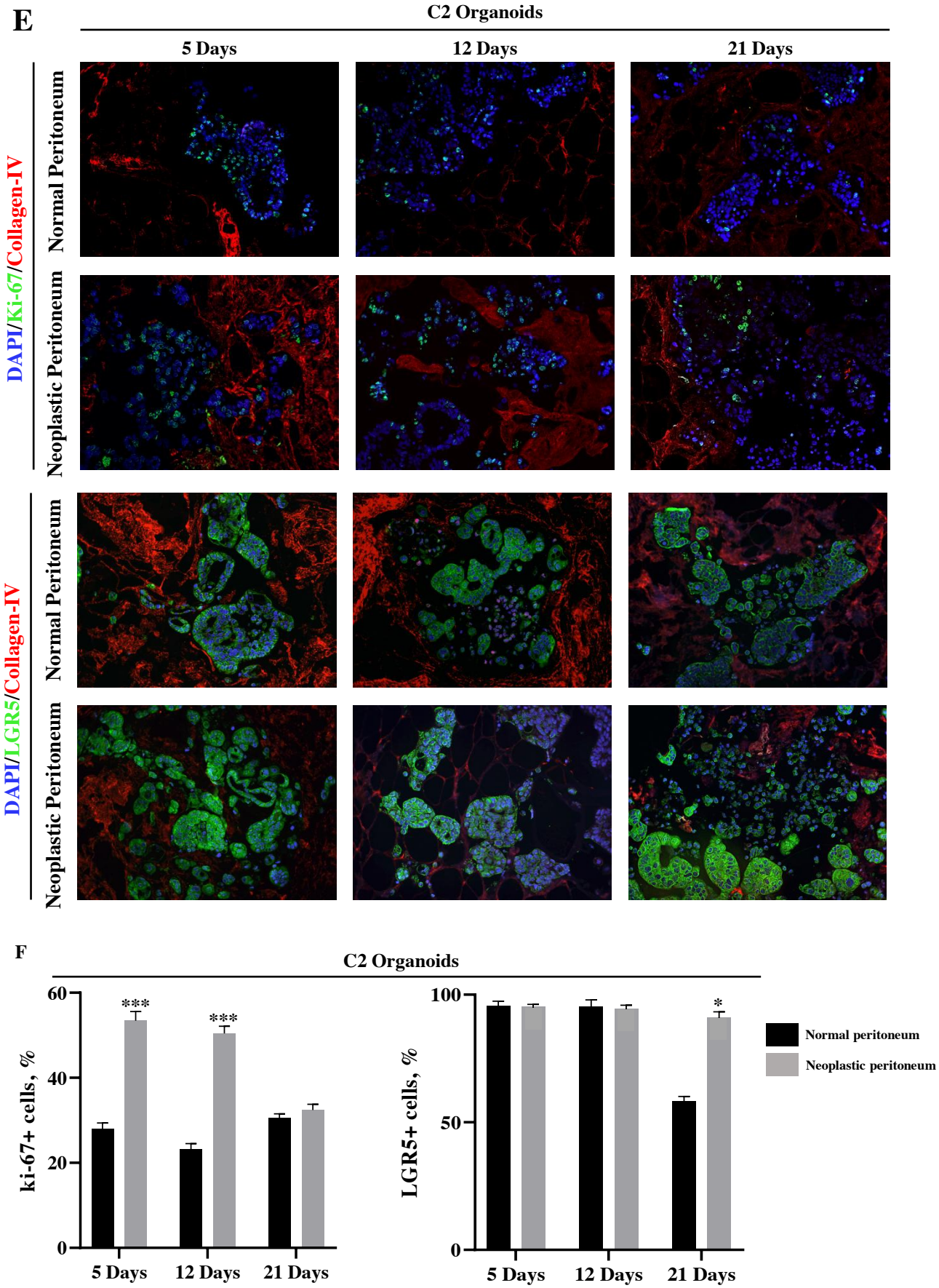

Supplementary Fig. S3. (E) Top panel: IF analysis of 3D-dECMs derived from normal (top) and neoplastic (bottom) peritoneum repopulated with PM-derived organoids (C2) at different time points as indicated, using Ki-67 (green) and collagen IV (red) antibodies. Scale bar: 50 µm. The experiments were performed in triplicate. **Bottom panel:** IF analysis of 3D-dECMs derived from normal (top) and neoplastic (bottom) peritoneum repopulated with PM-derived organoids (C2) at different time points as indicated, using LGR5 (green) and collagen IV (red) antibodies. The samples were counterstained with DAPI (blue) Scale bar: 50 µm. The experiments were performed in triplicate. **(F) Left panel:** proliferation rate of PM-derived organoids, measured as the percentage of Ki-67^{+} cells present in fields devoid of dead cells. Five fields per experiment (40X magnification) were counted. Data are presented as median and SD. One-way ANOVA (***p<0.001). **Right panel:** amount of stem cells in PM-derived organoids, measured as the percentage of LGR5^{+} cells present in fields devoid of dead cells. Five fields per experiment (40X magnification) were counted. Data are presented as median and SD. One-way ANOVA (*p<0.05). The experiments were performed in triplicate.

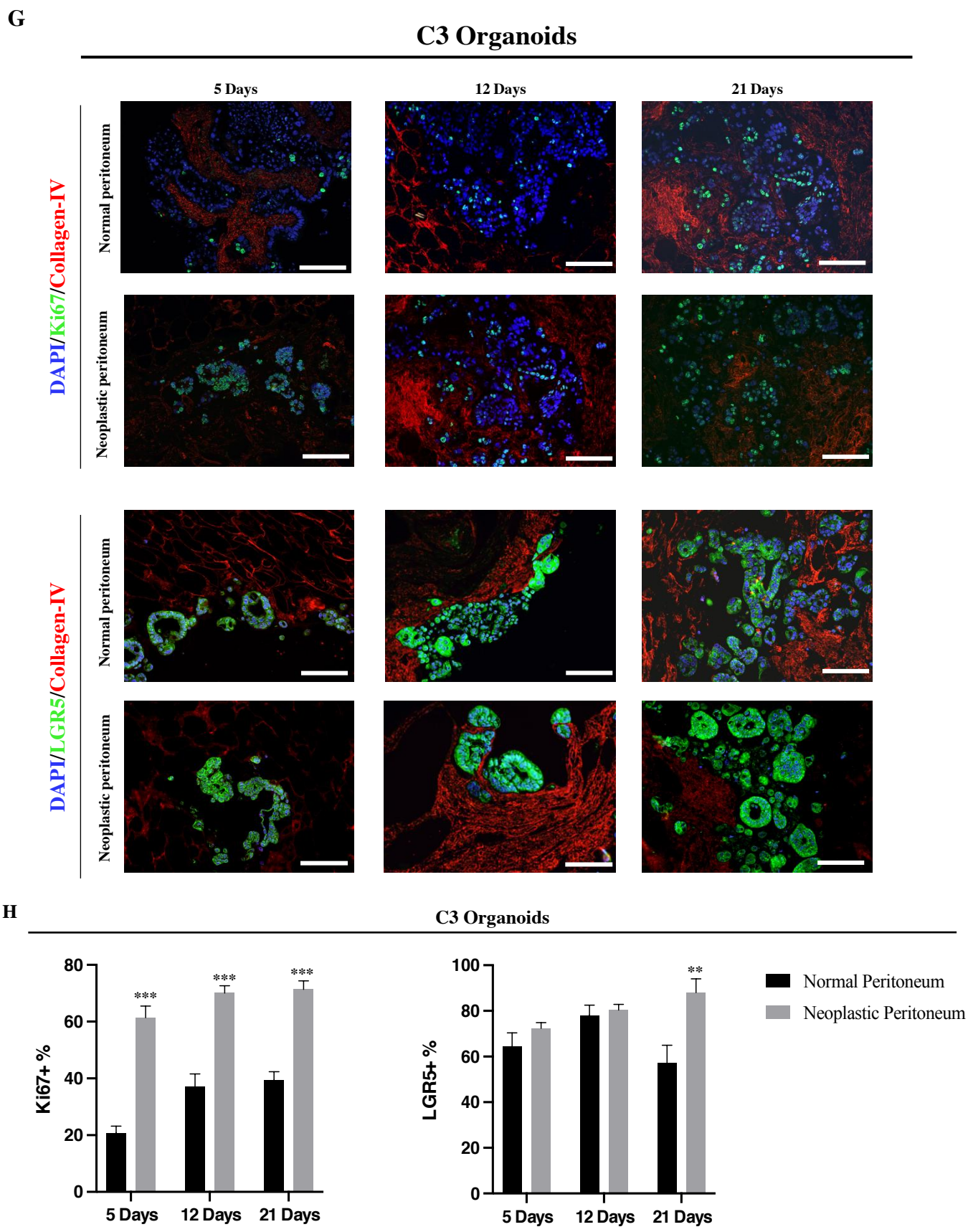

Supplementary Fig. S3. (G) Top panel: IF analysis of 3D decellularized matrices derived from normal (top) and neoplastic (bottom) peritoneum repopulated with PM-derived organoids (C3), using Ki-67 (green) and collagen IV (red) (left panel). **Bottom panel:** LGR5 (green) and collagen IV (red) (right panel) antibodies. The samples were counterstained with DAPI (blue). Scale bar: 50 µm. The experiments were performed in triplicate. **(H) Left panel:** proliferation rate of PM-derived organoids measured as the percentage of Ki-67^{+} cells present in fields devoid of dead cells. Five fields per experiment (40X magnification) were counted. Data are presented as median and SD. Student's *t-test* (**p<0.01). **Right panel:** percentage of stem cells in PM-derived organoids, measured as the percentage of LGR5^{+} cells present in fields devoid of dead cells. Five fields per experiment (40X magnification) were counted. Data are presented as median and SD. Student's *t-test* (*p<0.05). The experiments were performed in triplicate.

Supplementary Figure S4

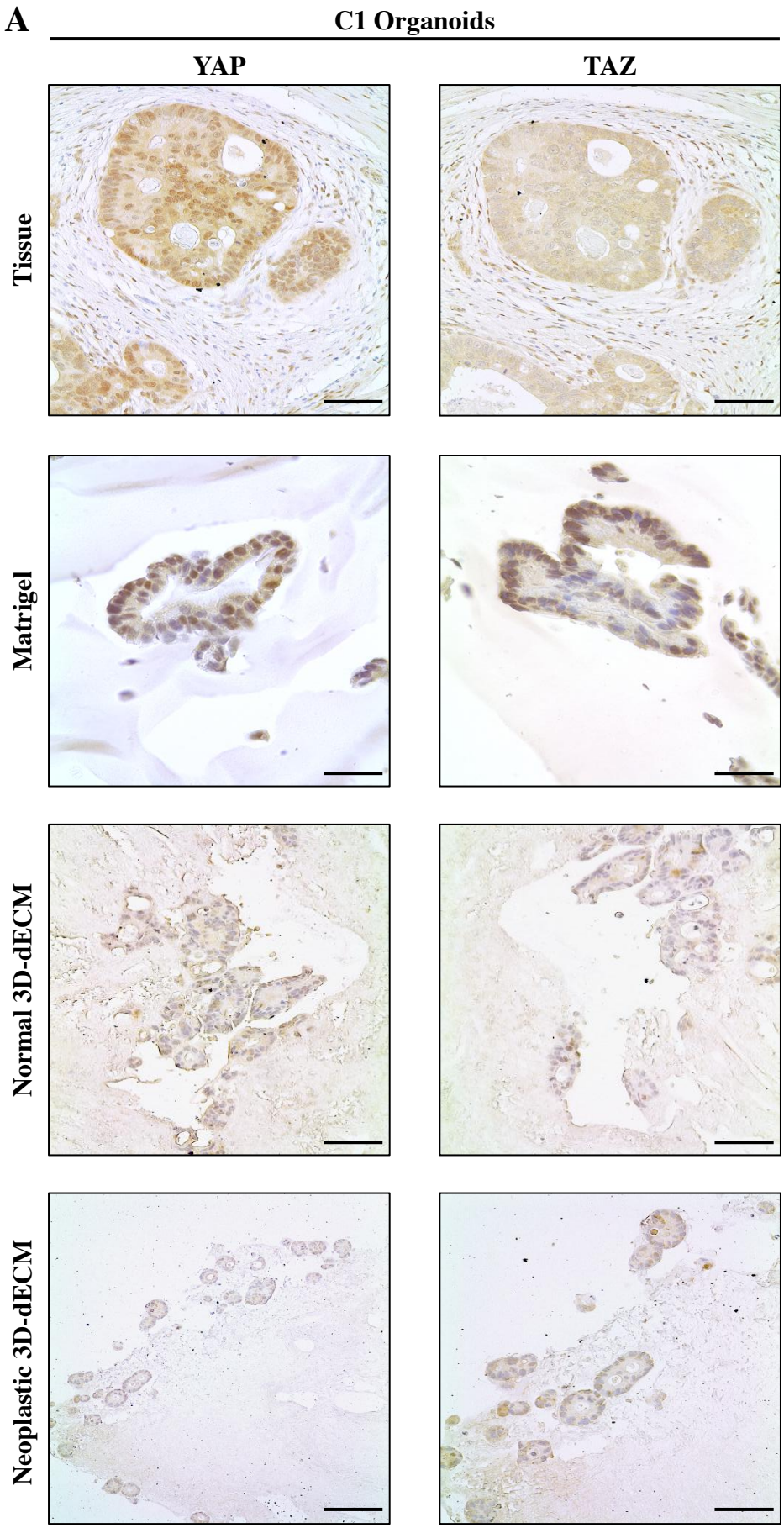

Supplementary Fig. S4. (A) Comparative immunohistochemical images of PM-derived organoids (C1) grown on different substrates (Matrigel, Normal 3D-dECM and Neoplastic 3D-dECM) and their corresponding tumor of origin. Expression of YAP and TAZ proteins was analysed. Scale bar: 100 μM.

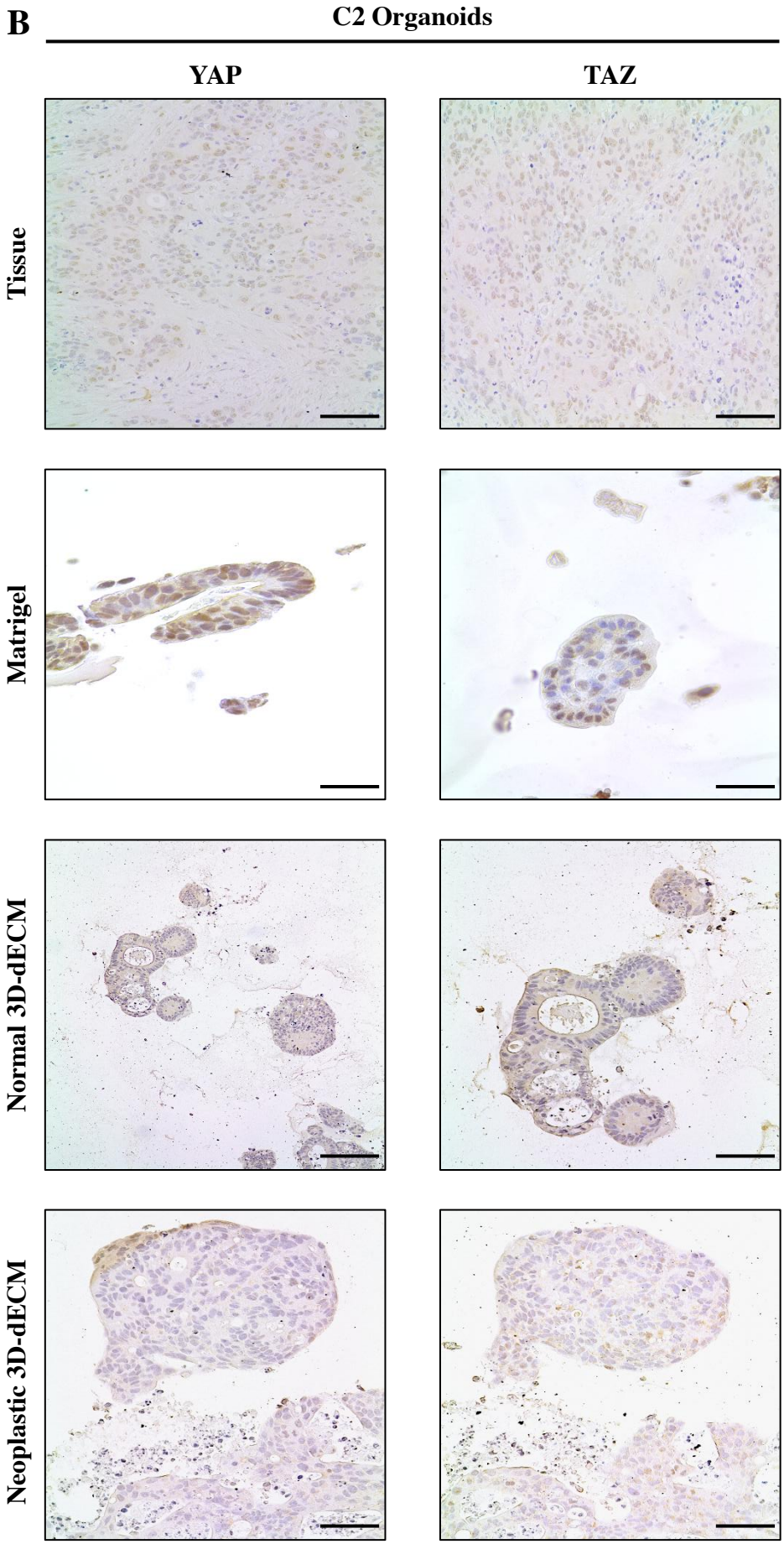

Supplementary Fig. S4. (B) Comparative immunohistochemical images of PM-derived organoids (C2) grown on different substrates (Matrigel, Normal 3D-dECM and Neoplastic 3D-dECM) and their corresponding tumor of origin. Expression of YAP and TAZ proteins was analyzed. Scale bar: 100 μM.

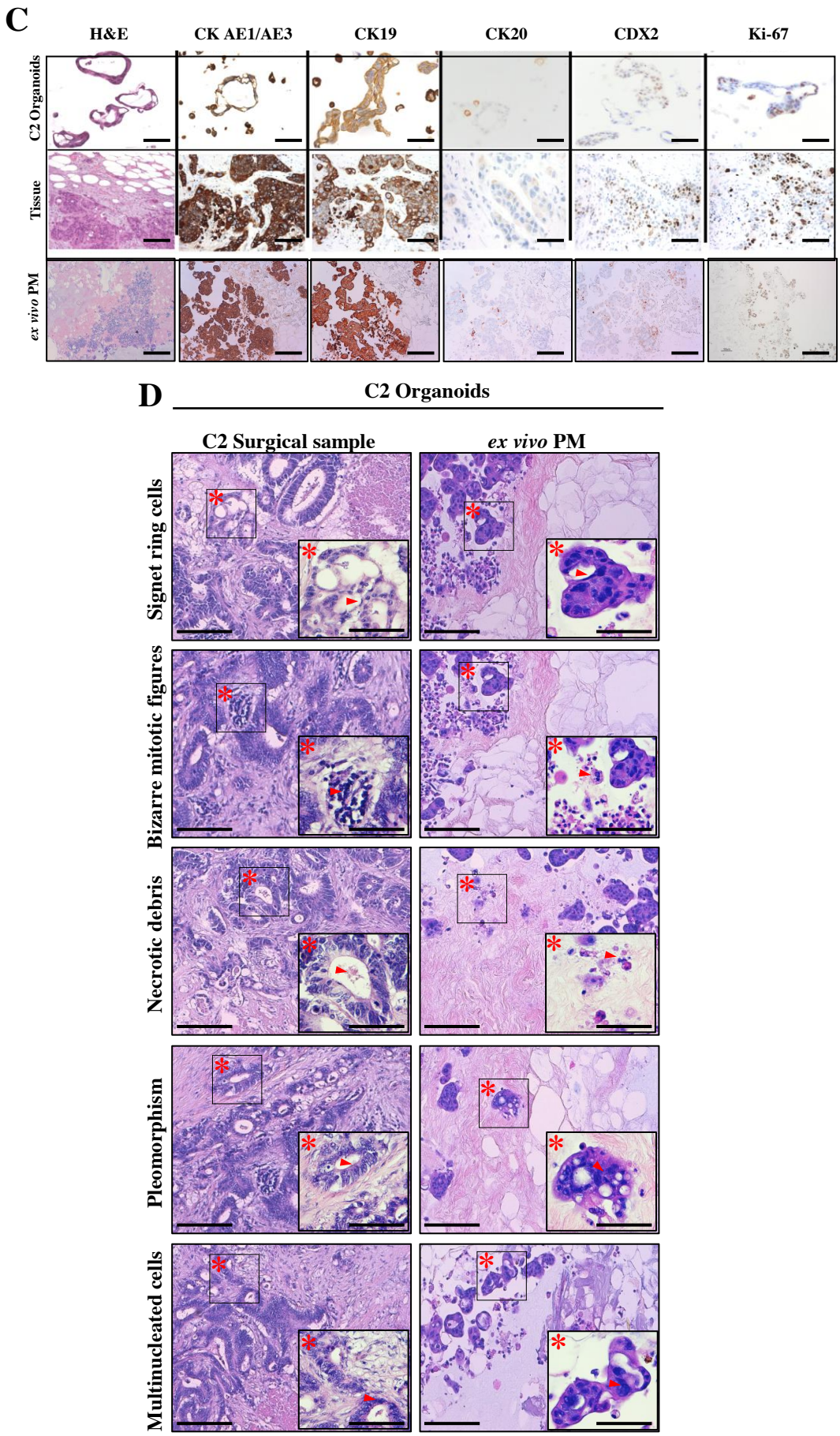

Supplementary Fig. S4. **(C)** Comparative histological and immunohistochemical analysis of C2 PM-derived organoids Vs their corresponding tumor of origin and the *ex vivo* engineered PM lesion. Samples were analyzed for the expression of the CRC-specific markers as indicated. Scale bar: 50 μM. Images in the first two lanes were previously published [11]. **(D)** Histological analysis of PM and neoplastic-derived 3D-dECM repopulated with C2 PM-derived organoids. The *ex vivo* engineered PM lesions present histological features that are typical of PMs of gastrointestinal origin. Asterisks and arrows indicated the main morphological features. Scale bar: 20 μm.

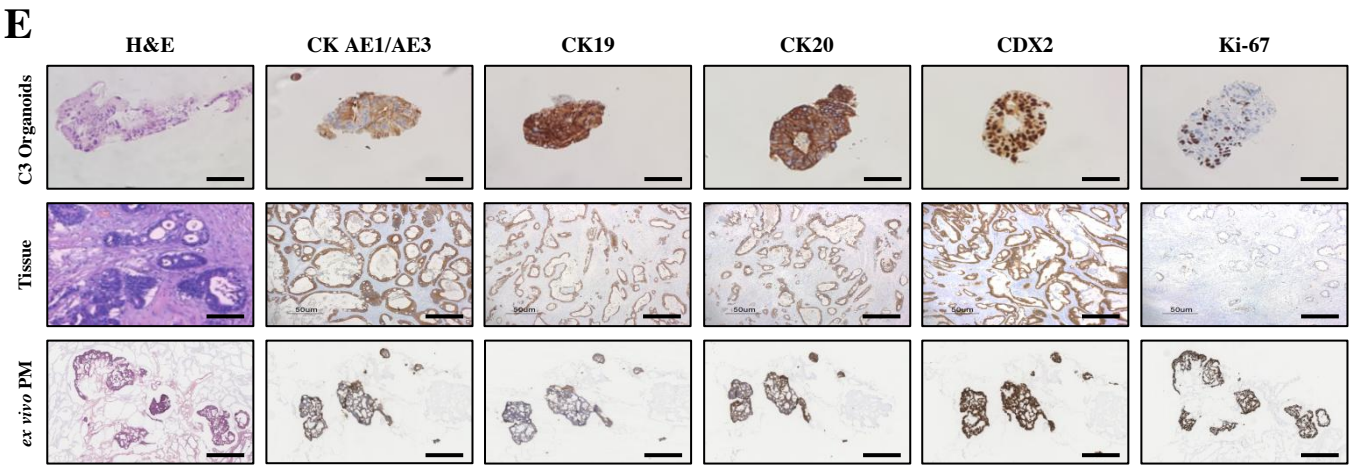

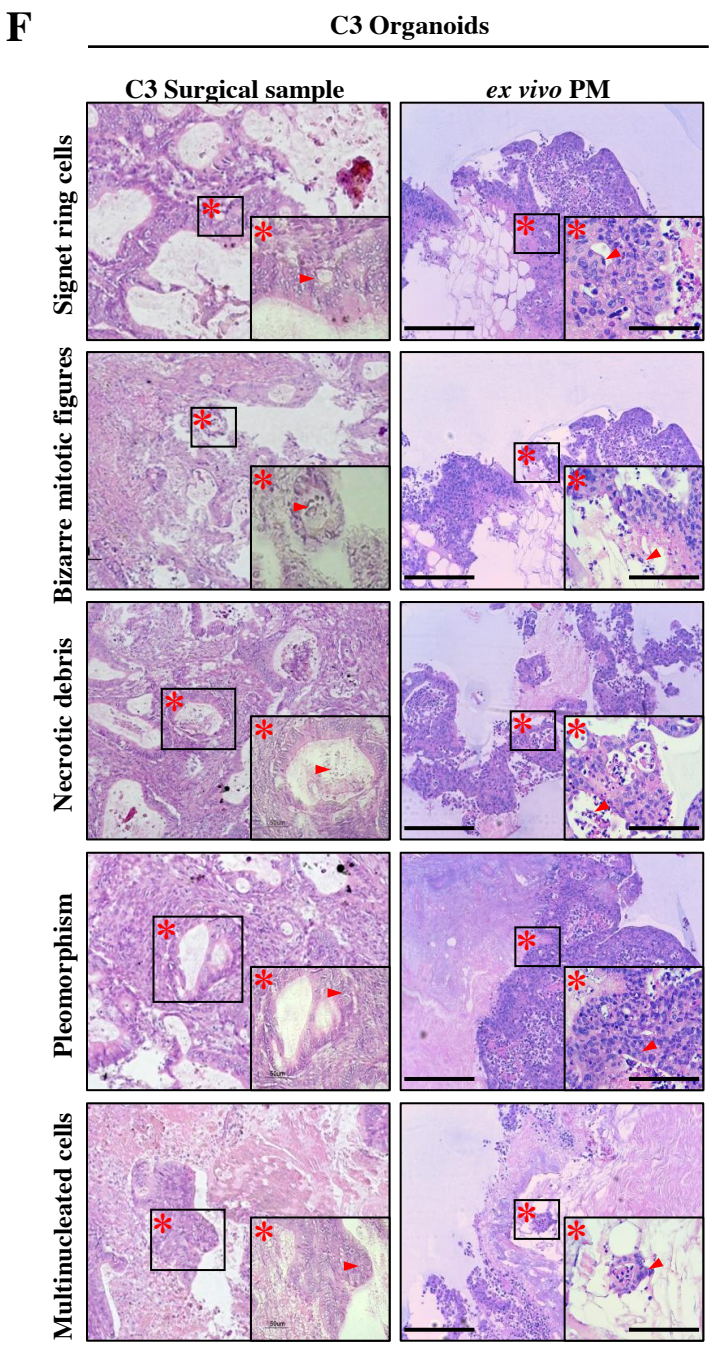

Supplementary Fig. S4. (E) Comparative histological and immunohistochemical analysis of C3 PM-derived organoids Vs their corresponding tumor of origin and the *ex vivo* engineered PM lesion. Samples were analyzed for the expression of the CRC-specific markers as indicated. Scale bar: 50 µm. **(F)** Histological analysis of peritoneal metastasis and neoplastic-derived 3D-dECMS repopulated with C3 PM-derived organoids. The *ex vivo* engineered PM lesions present histological features that are typical of PMs of gastrointestinal origin. Asterisks and arrows indicated the main morphological features. Scale bar: 20 µm.

G

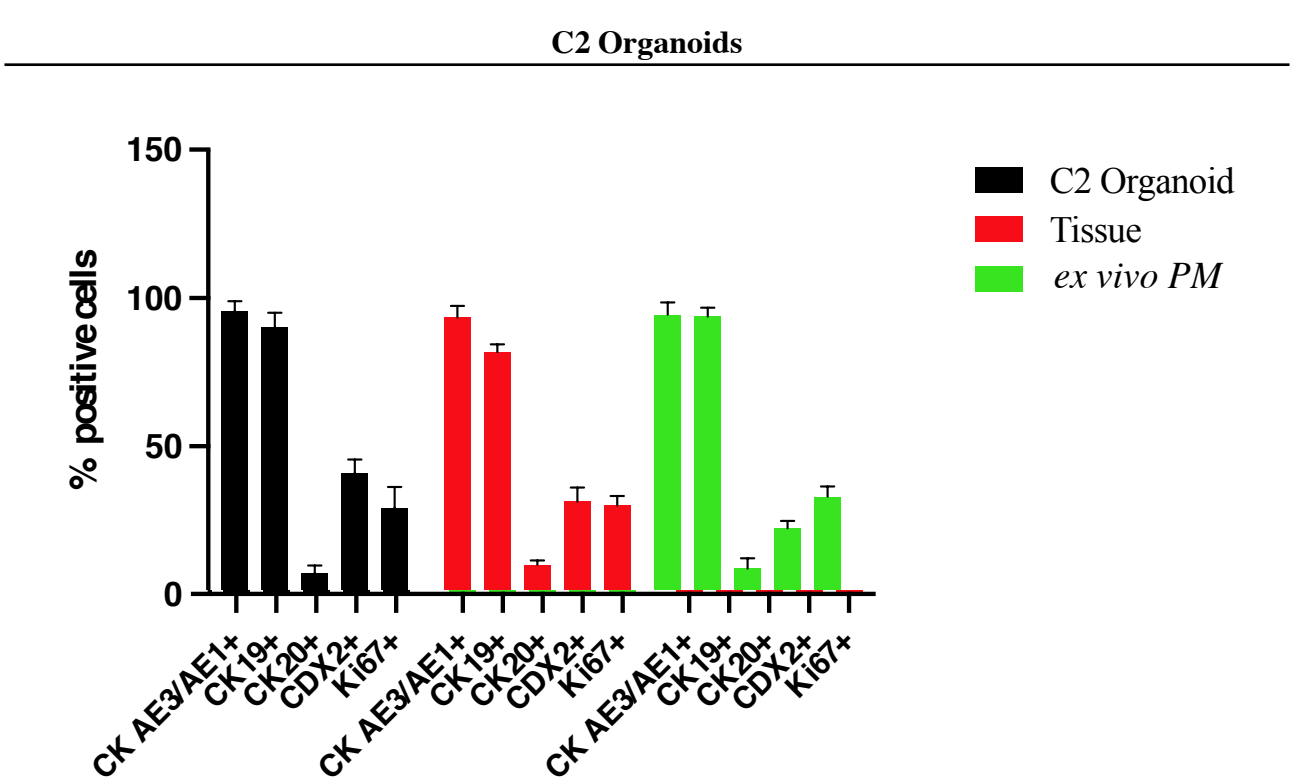

H

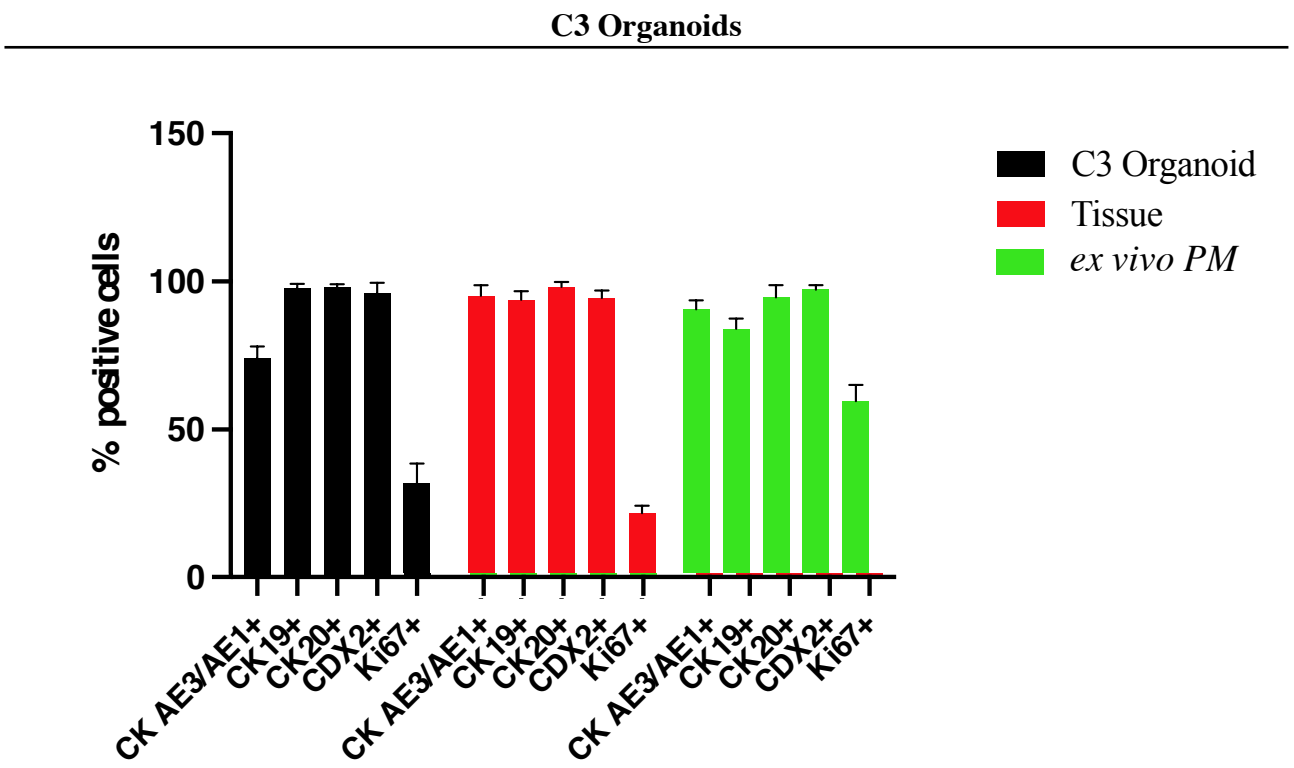

Supplementary Fig. S4. (G) Quantitative counts of the percentage of CK AE/AE3, CK19, CK20, CDX2 and Ki-67 positive cells in C2 PM-derived organoids Vs their corresponding tumor of origin and the *ex vivo* engineered PM lesion Three fields per experiments were counted using Qpath software. Data are presented as median and SD. One-way ANOVA did not show differences between the two groups. **(H)** Quantitative counts of the percentage of CK AE/AE3, CK19, CK20, CDX2 and Ki-67 positive cells in C3 PM-derived organoids Vs their corresponding tumor of origin and the *ex vivo* PM engineered lesion. Three fields per experiments were counted using Qpath software. Data are presented as median and SD. One-way ANOVA did not show differences between the two groups.

Supplementary Figure S5

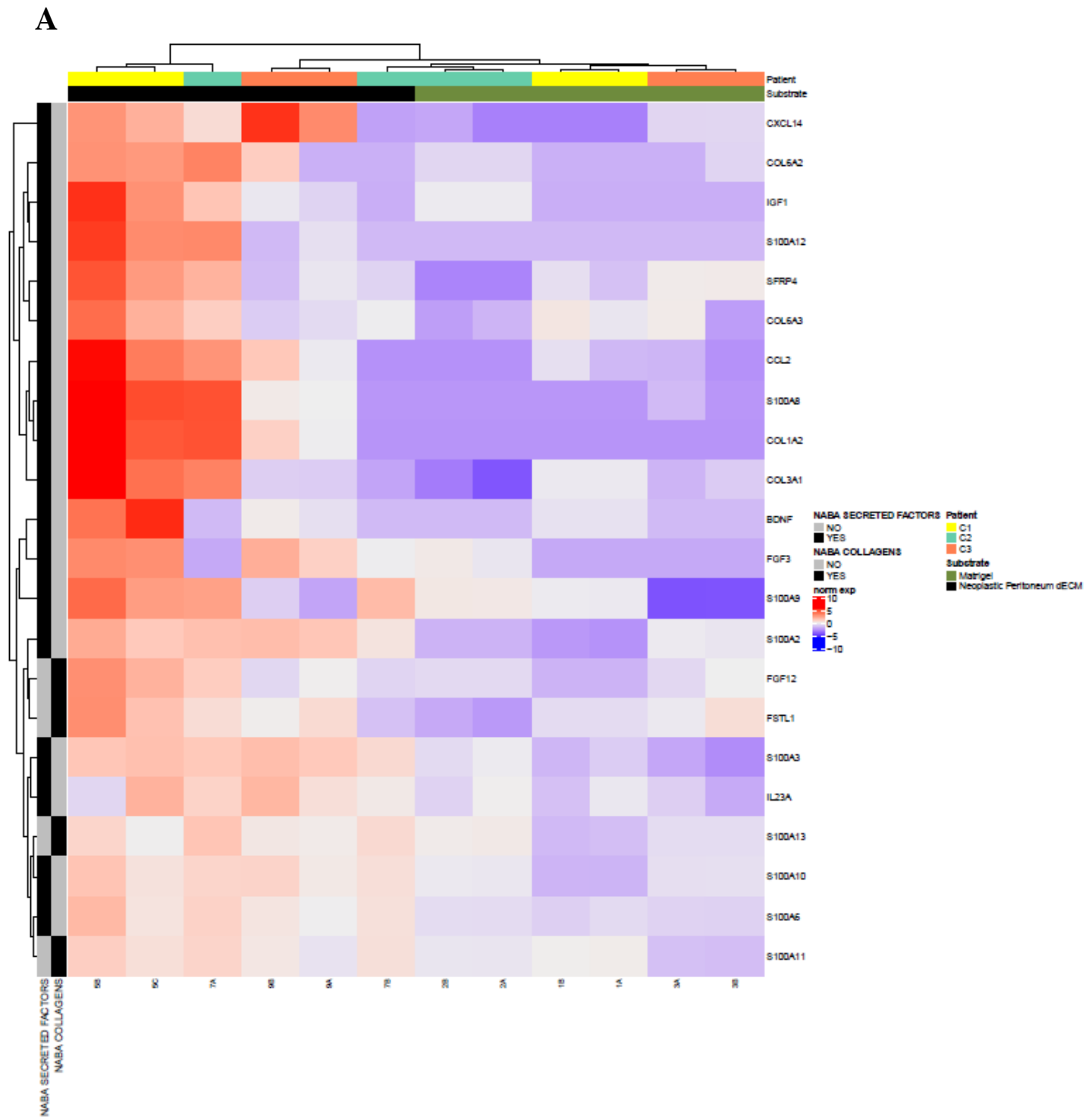

Supplementary Fig. S5. (A) Unsupervised hierarchical clustering of organoids based on the expression of the top DEGs between organoids grown on neoplastic 3D-dECM and in Matrigel, and present in Naba Secreted Factors or Naba Collagen categories.

B

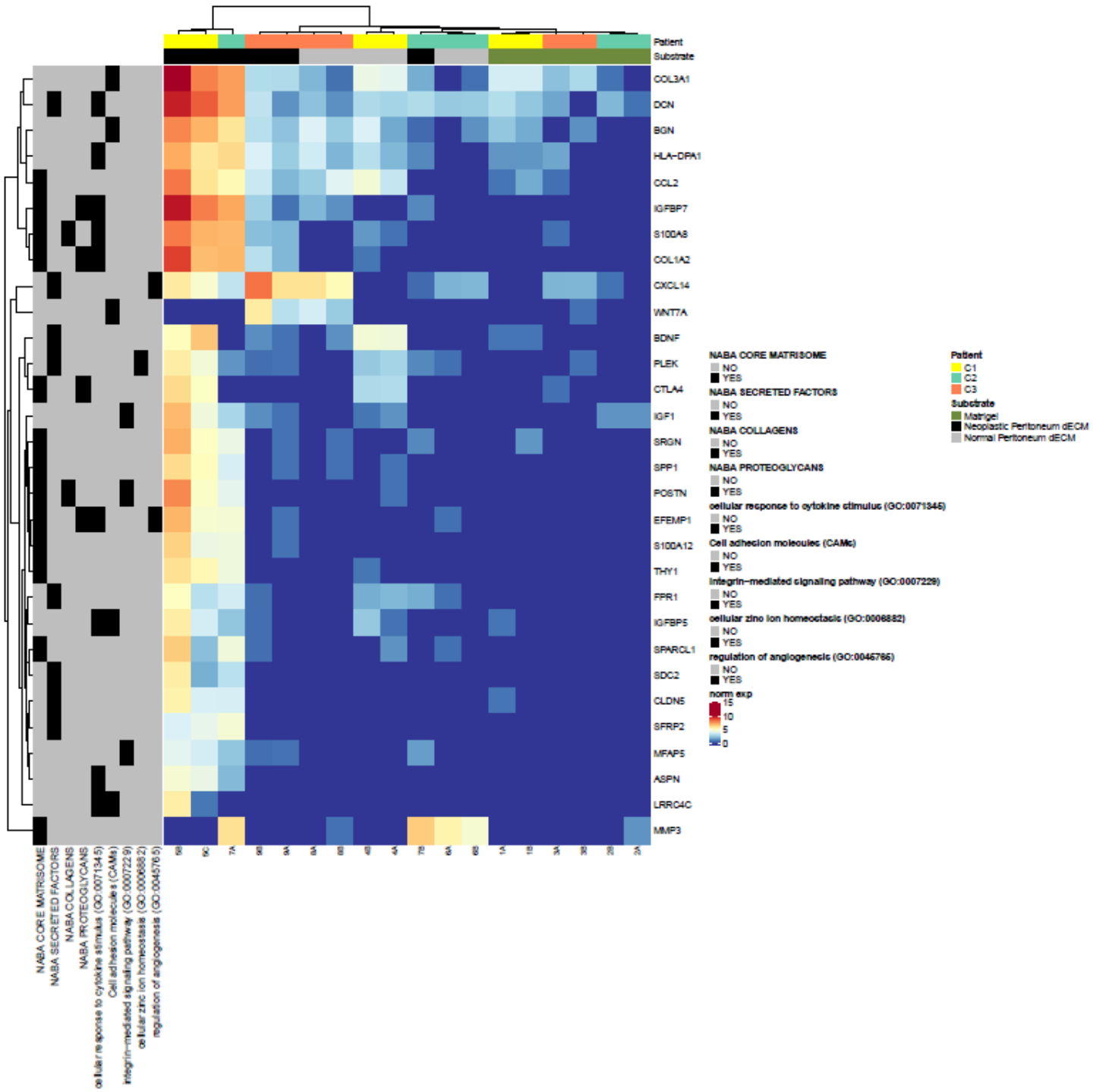

Supplementary Fig. S5. (B) Unsupervised hierarchical clustering of organoids based on the expression of the top DEGs between organoids grown on neoplastic 3D-dECM, normal 3D-dECM and in Matrigel, and present in Naba Core Matrisome, Naba Secreted Factors, Naba Collagen categories, Naba Proteoglycan categories, cellular response to cytokine stimulus, cell adhesion molecules, integrin mediated signaling pathway, cellular zinc ion homeostasis, and regulation of angiogenesis categories.

C

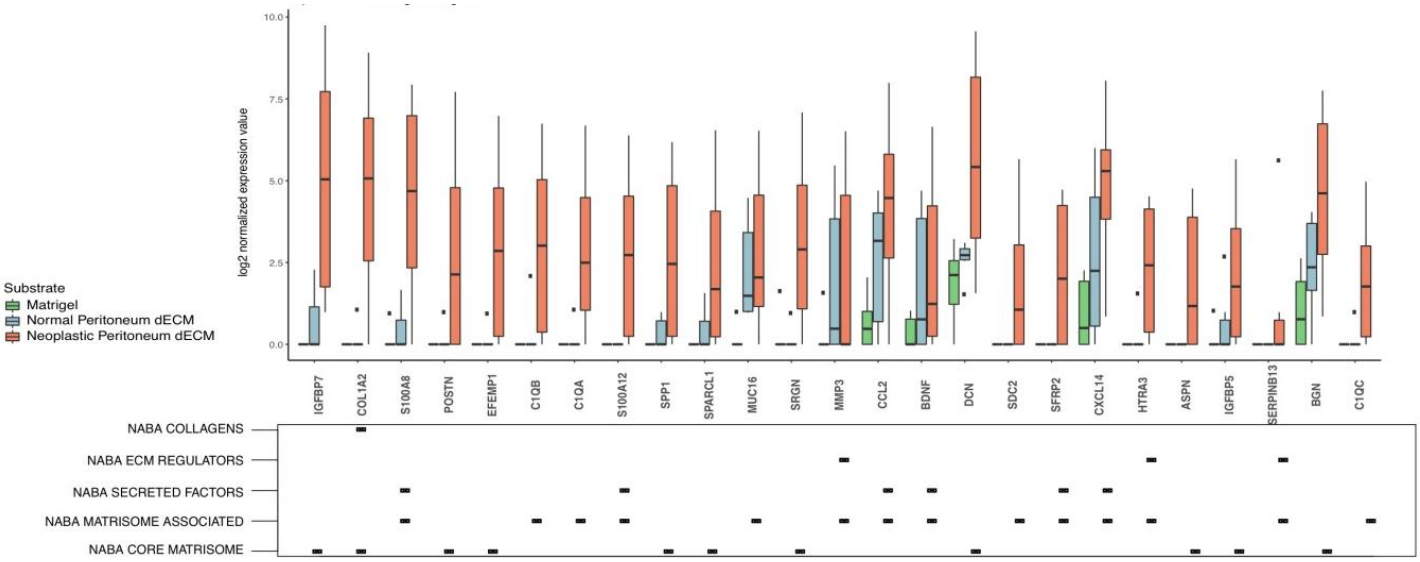

D

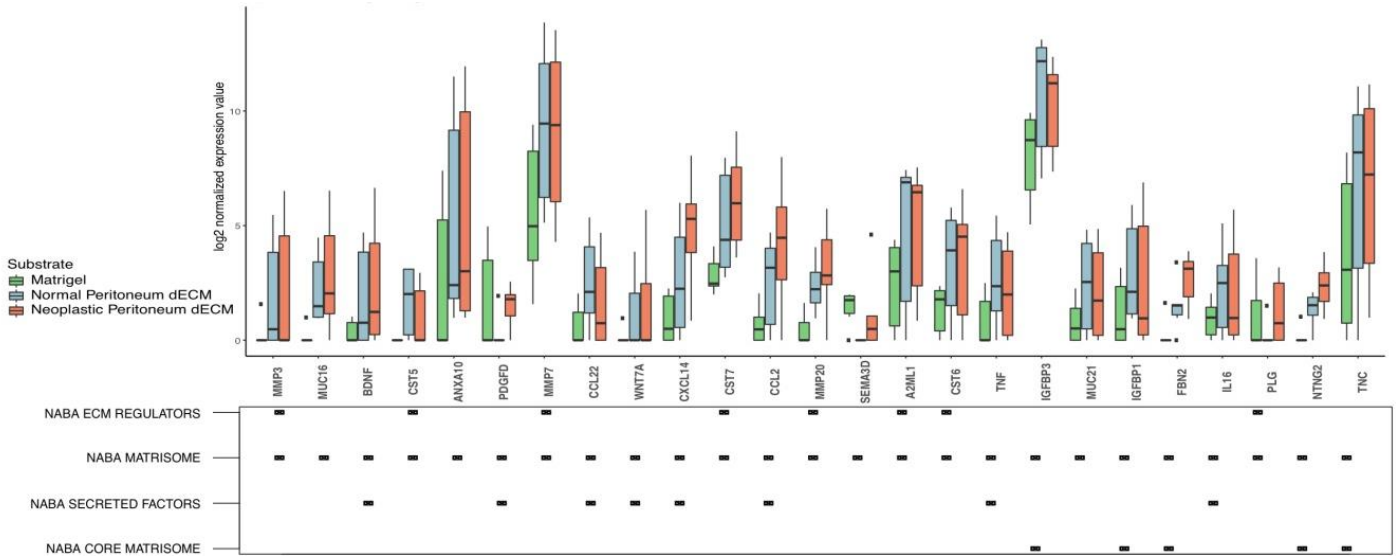

Supplementary Fig. S5. **(C)** Box plot showing the expression in organoids grown on neoplastic 3D-dECM and in Matrigel, of DEGs selected based on their involvement in the indicated processes of the Naba Matrisome geneset. DEGs expression in organoids grown on normal 3D-dECM is also shown. Median and interquartile range are displayed as horizontal lines. Black squares in the bottom panel indicate which category the genes belong to. **(D)** Box plot showing the expression, in organoids grown on normal 3D-dECM and in Matrigel, of DEGs selected based on their involvement in the indicated processes of the Naba Matrisome geneset. DEGs expression in organoids grown on neoplastic 3D-dECM is also shown. Median and interquartile range are displayed as horizontal lines. Black squares in the bottom panel indicate which category the genes belong to.

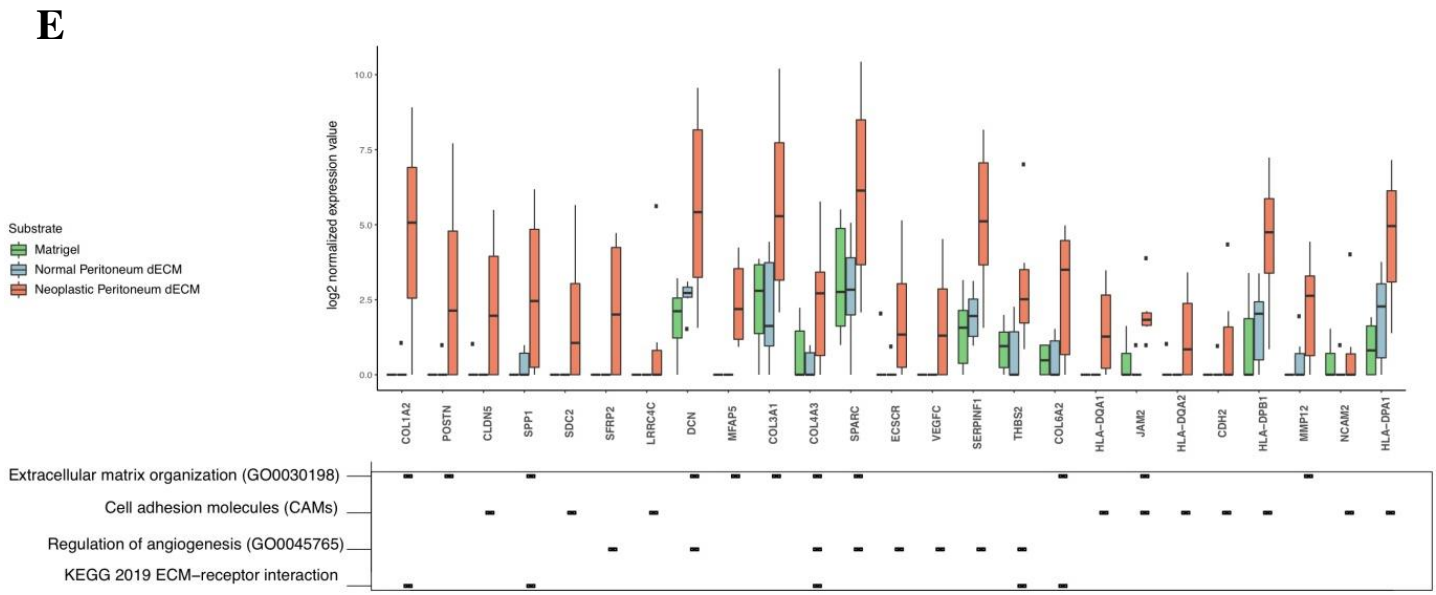

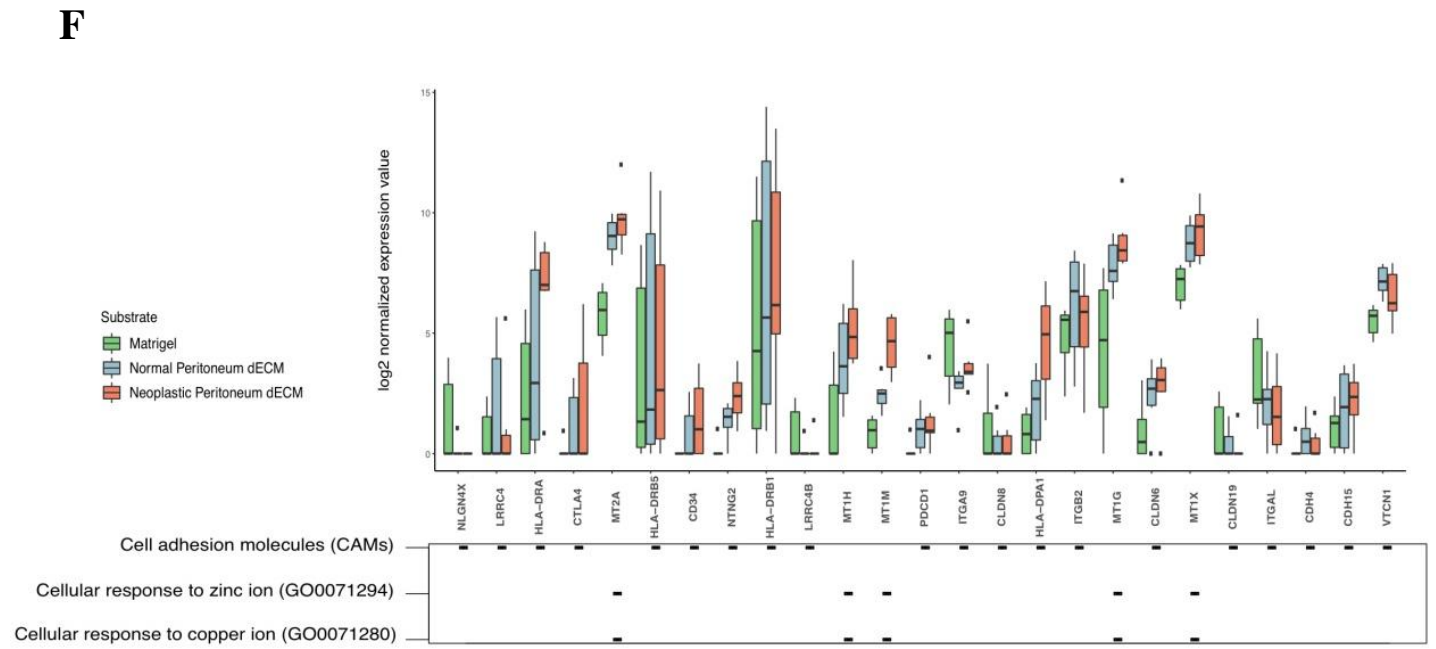

Supplementary Fig. S5. (E) Box plot showing the expression in organoids grown on normal 3D-dECMs and in Matrigel, of DEGs selected based on their involvement in the indicated processes of GO Biological Process, KEGG and Reactome databases. DEGs expression in organoids grown on neoplastic 3D-dECM is also shown. Median and interquartile range are displayed as horizontal lines. Black squares in the bottom panel indicate which category the genes belong to. **(F)** Box plot showing the expression levels of genes selected based on their involvement in the indicated processes. The expression levels of the selected genes were compared in organoids grown in Matrigel, on neoplastic 3D-dECM and on normal 3D-dECM. Median and interquartile range are displayed as horizontal lines. Black squares in the bottom panel indicate which category the genes belong to.

G

	Collection	ID	Term	Adjusted *p-value*	Leading Edge genes (%)	# Genes
Neoplastic 3D-dECM Vs Matrigel	GO BP	GO:0071345	Cellular response to cytokine stimulus	0.003365	27.1	413
	GO BP	GO:0045765	Regulation of angiogenesis	0.003365	19.3	171
	GO BP	GO:0006882	Cellular zinc ion homeostasis	0.003365	46.7	30
	GO BP	GO:0071280	Cellular response to copper ion	0.003365	55.0	20
	GO BP	GO:0007229	Integrin-mediated signaling pathway	0.011230	19.6	56
	KEGG		Wnt signaling pathway	0.022987	20.5	151
Normal 3D-dECM Vs Matrigel	GO BP	GO:0071280	Cellular response to copper ion	0.006015	55.0	20
	GO BP	GO:0071294	Cellular response to zinc ion	0.006015	64.7	17
	KEGG		Cell adhesion molecules (CAMs)	0.006015	32.8	128
Neoplastic 3D-dECM Vs Normal 3D-dECM	KEGG		ECM-receptor interaction	0.004499	25.0	80
	GO BP	GO:0045765	Regulation of angiogenesis	0.009176	15.2	171
	KEGG		Cell adhesion molecules (CAMs)	0.020511	22.7	132
	Reactome	R-HSA-5660526	Response to metal ions Homo sapiens	0.040965	81.8	11
	GO BP	GO:0030198	Extracellular matrix organization	0.002740	25.3	221

H

	Collection	Term	Adjusted *p-value*	Leading Edge genes (%)	# Genes
Neoplastic 3D-dECM Vs Matrigel	NABA MATRISOME	Naba Matrisome Associated	0.003365	38.2	663
	NABA MATRISOME	Naba Core Matrisome	0.003365	36.1	266
	NABA MATRISOME	Naba ECM Regulators	0.003365	30.6	222
	NABA MATRISOME	Naba Secreted Factors	0.003365	45.1	288
	NABA MATRISOME	Naba Collagens	0.004307	31.2	44
Normal 3D-dECM Vs Matrigel	NABA MATRISOME	Naba ECM Regulators	0.0060150	39.2	217
	NABA MATRISOME	Naba Core Matrisome	0.006015	22.7	256
	NABA MATRISOME	Naba Secreted Factors	0.006015	34.7	274
	NABA MATRISOME	Naba Matrisome	0.006024	32.9	897
Neoplastic 3D-dECM Vs Normal 3D-dECM	NABA MATRISOME	Naba Core Matrisome	0.002740	26.3	266
	NABA MATRISOME	Naba Secreted Factors	0.002740	39.2	291
	NABA MATRISOME	Naba ECM Glycoproteins	0.002740	21.9	192
	NABA MATRISOME	Naba Collagens	0.002740	40.9	44
	NABA MATRISOME	Naba Proteoglycans	0.002740	53.3	30
	NABA MATRISOME	Naba ECM Regulators	0.024908	28.2	16

Supplementary Fig. S5. (G) Selected categories enriched in DEGs between organoids grown on neoplastic 3D-dECM, normal 3D-dECM and in Matrigel involved in relevant biological processes according to GO Biological Process, KEGG and Reactome databases. **(H)** Selected Matrisome categories enriched in DEGs between organoids grown on neoplastic 3D-dECM, normal 3D-dECM and in Matrigel involved in relevant biological processes according to Naba Maatrisome dataset.

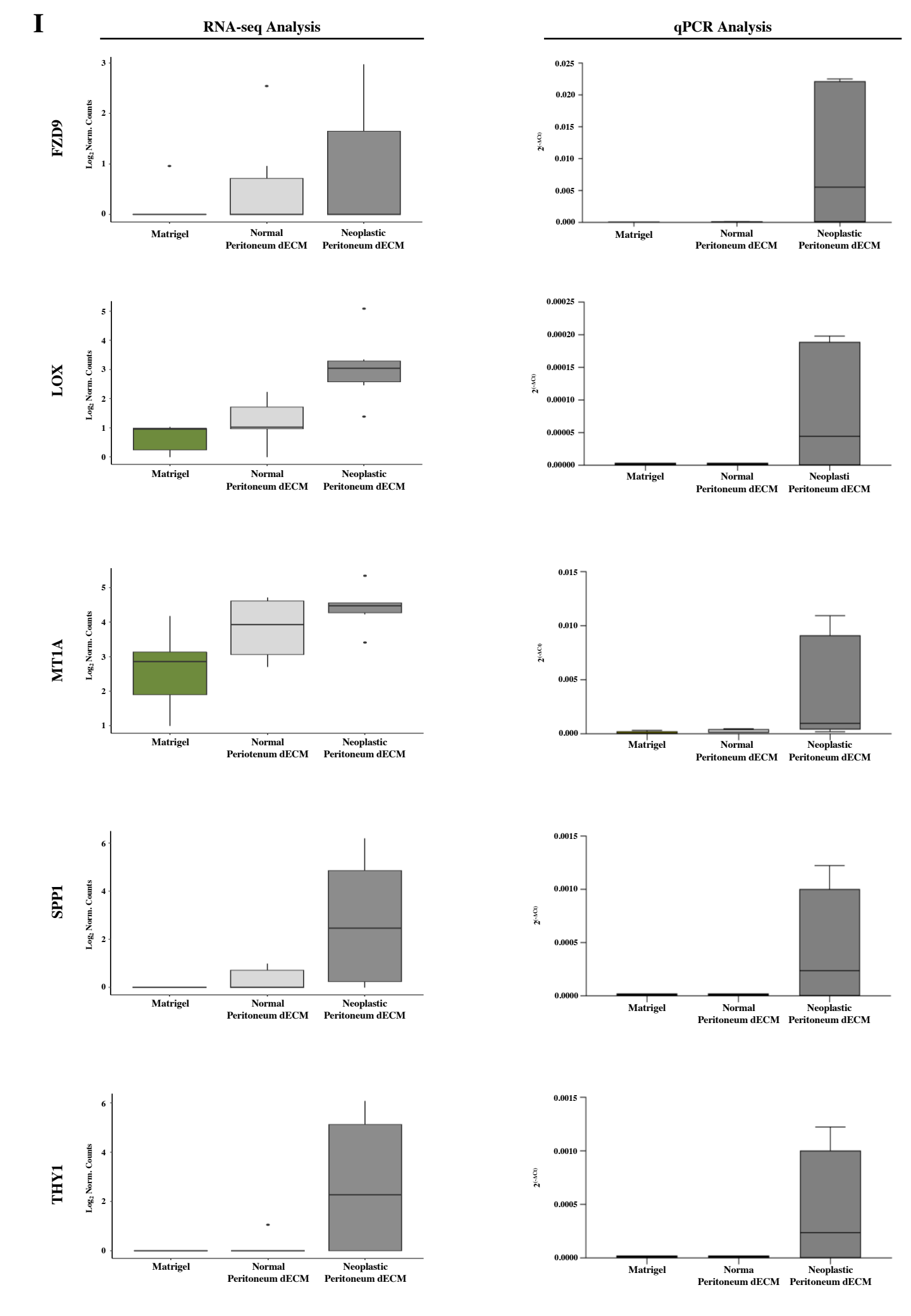
I
RNA-seq Analysis
qPCR Analysis
FZD9
LOX
MT1A
SPP1
THY1
Log2 Norm. Counts
2^(-ΔCt)
Matrigel
Normal Peritoneum dECM
Neoplastic Peritoneum dECM
Periotenum dECM
Neoplasti
Norma

L

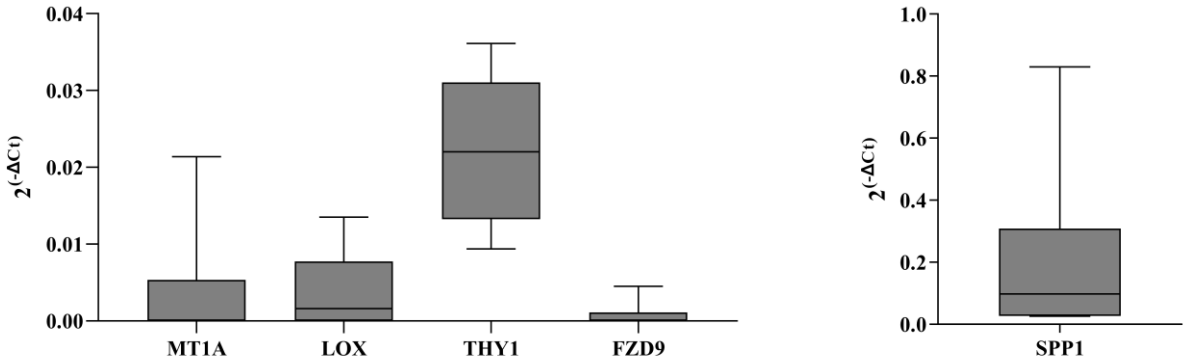

Supplementary Fig. S5. (I) Expression levels of MT1A, LOX, THY1, FZD9 and SPP1 in C1, C2 and C3 grown into Matrigel and on normal and neoplastic-derived 3D-dECMs (left panel). Values are calculated as $\log_2$ of the total normal counts. The horizontal line inside the box indicates the median and the whiskers indicate the extreme measured values.
Expression levels of MT1A, LOX, THY1, FZD9 and SPP1 genes on organoid cultures grown in Matrigel and on normal or neoplastic peritoneal 3D-dECMs (right panel). Values are calculated as $2^{(-\Delta Ct)}$ and normalized to GAPDH. The horizontal line inside the box indicates the median and the whiskers indicate the extreme measured values. **(L)** Expression levels of MT1A, LOX, THY1, FZD9 and SPP1 genes on FFPE tissues from PM-derived organoids. Values are calculated as $2^{(-\Delta Ct)}$ and normalized to GAPDH. The horizontal line inside the box indicates the median and the whiskers indicate the extreme measured values.

Supplementary Figure S6

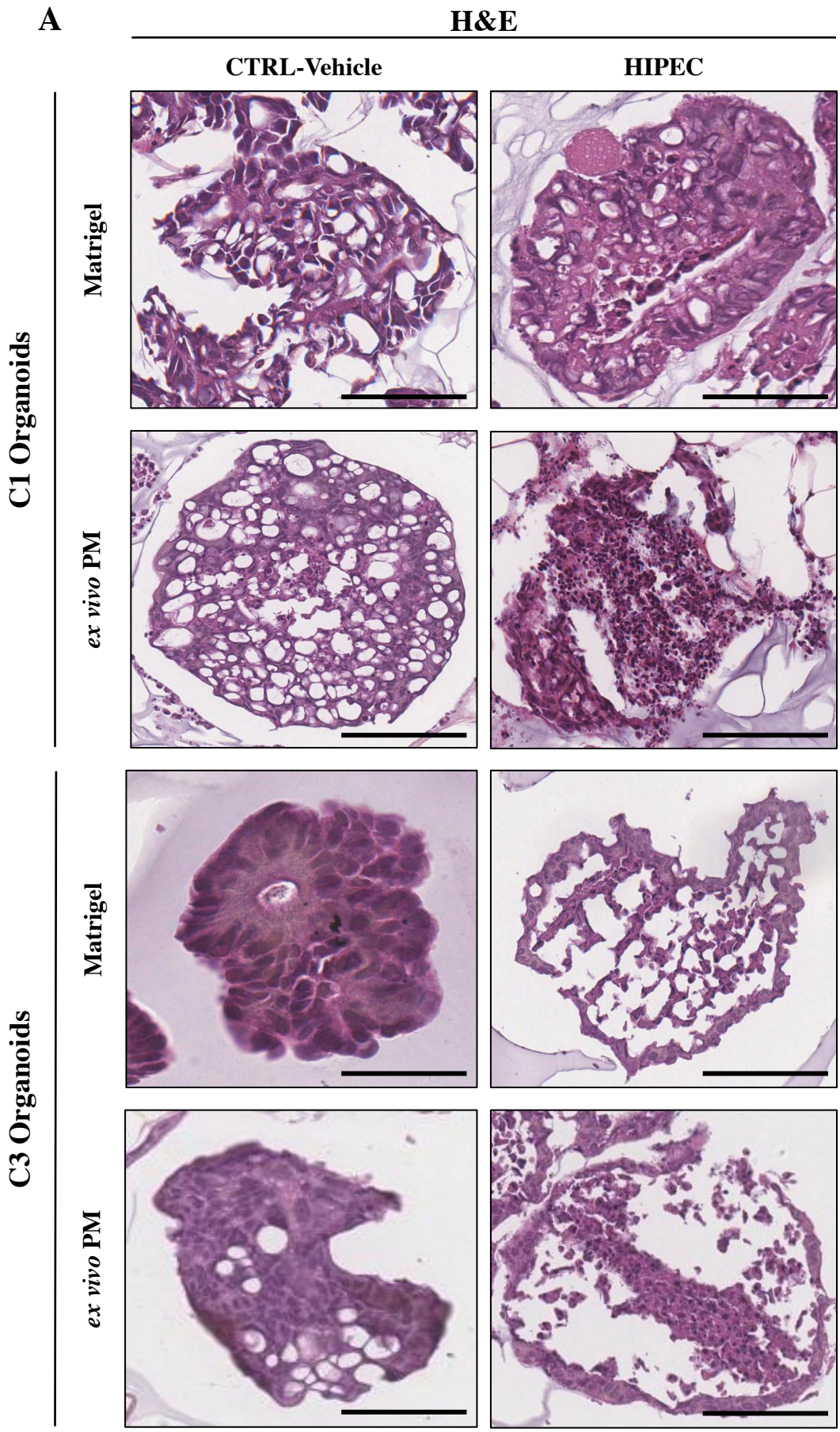

Supplementary Fig. S6. (A) H&E staining of C1 and C3 organoids cultured in Matrigel and on neoplastic-derived peritoneal 3D-dECMs after *in vitro* HIPEC treatments. Scale bar: 50 µm.

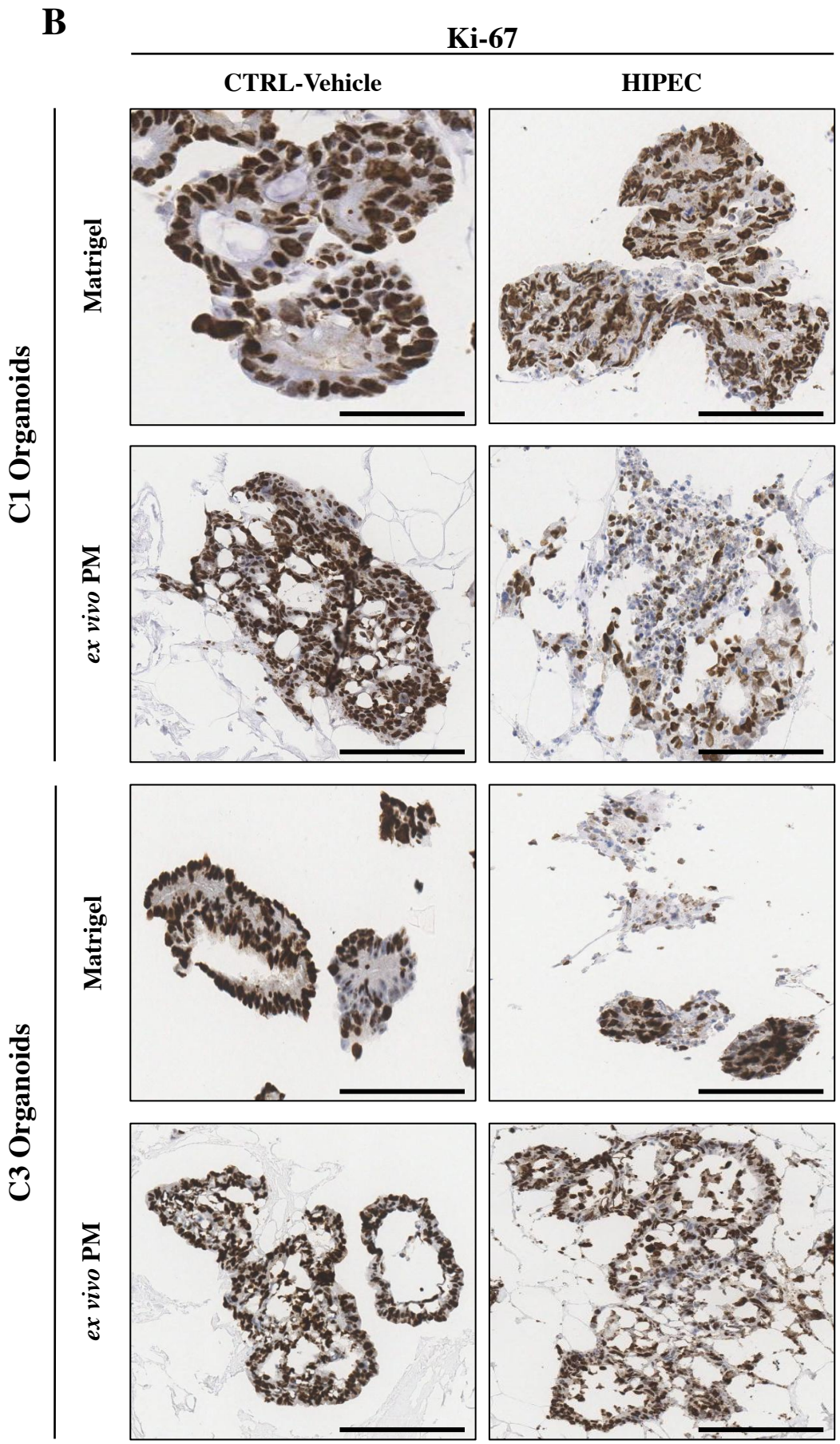

Supplementary Fig. S6. (B) Ki-67 immunostaining of C1 and C3 organoids cultured in Matrigel and on neoplastic-derived peritoneal 3D-dECMs after *in vitro* HIPEC treatments. Scale bar: 50 µm.

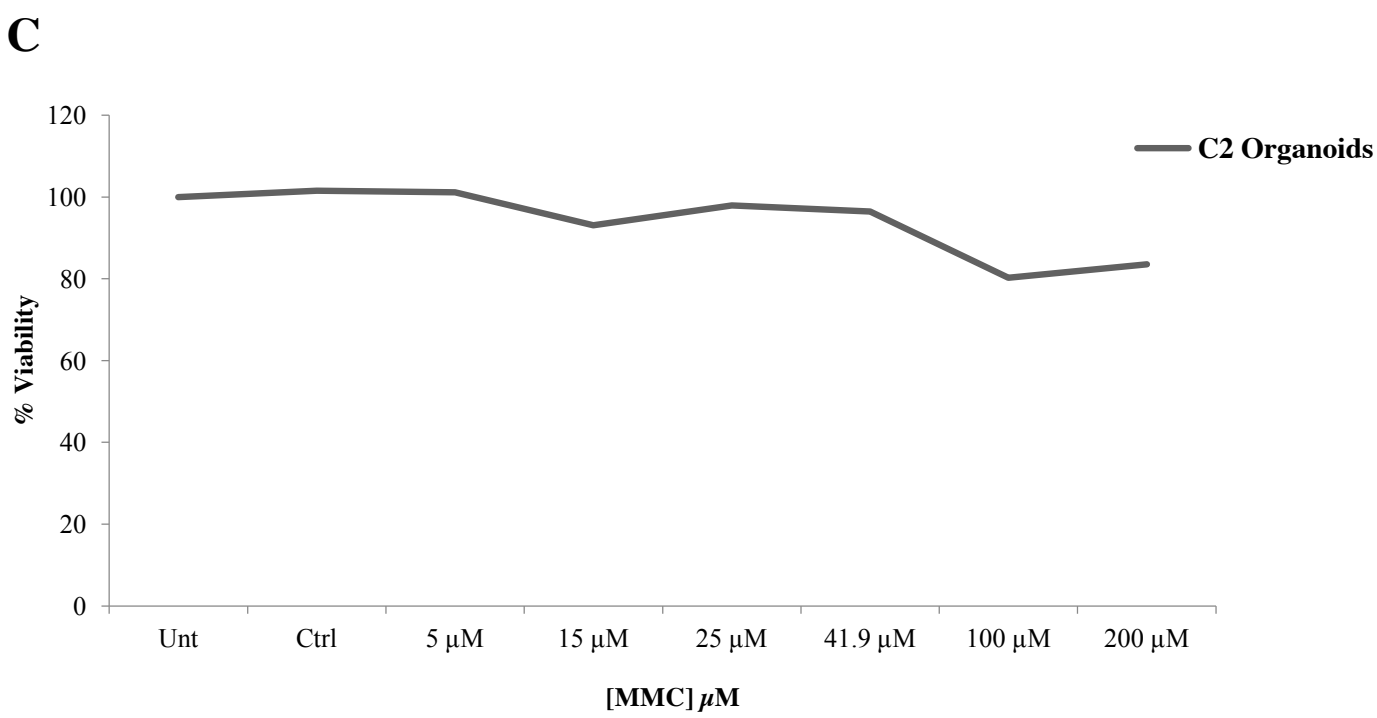

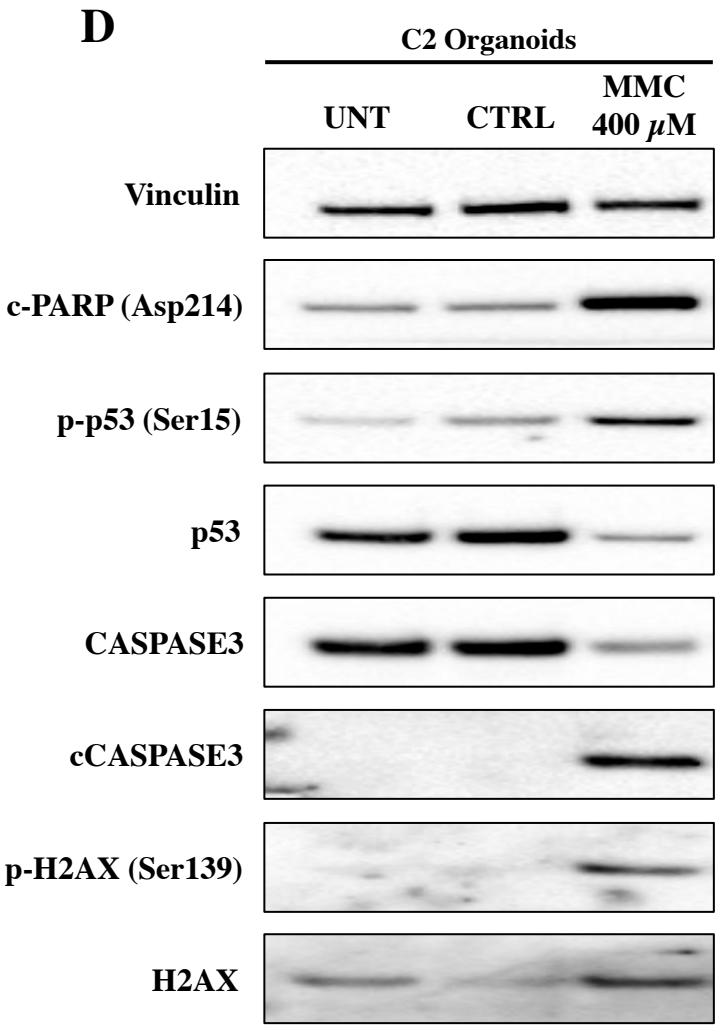

Supplementary Fig. S6. (C) Dose response curve of C2 PM-derived organoids cultured in Matrigel and treated with MMC at different concentrations at 42.5 °C for 1 h. **(D)** Immunoblots of cPARP, p-p53, p53, CASPASE3, cCASPASE3, p-H2AX and H2AX in C2 PM-derived organoids treated with MMC 400 µM. Vinculin was used as loading control.

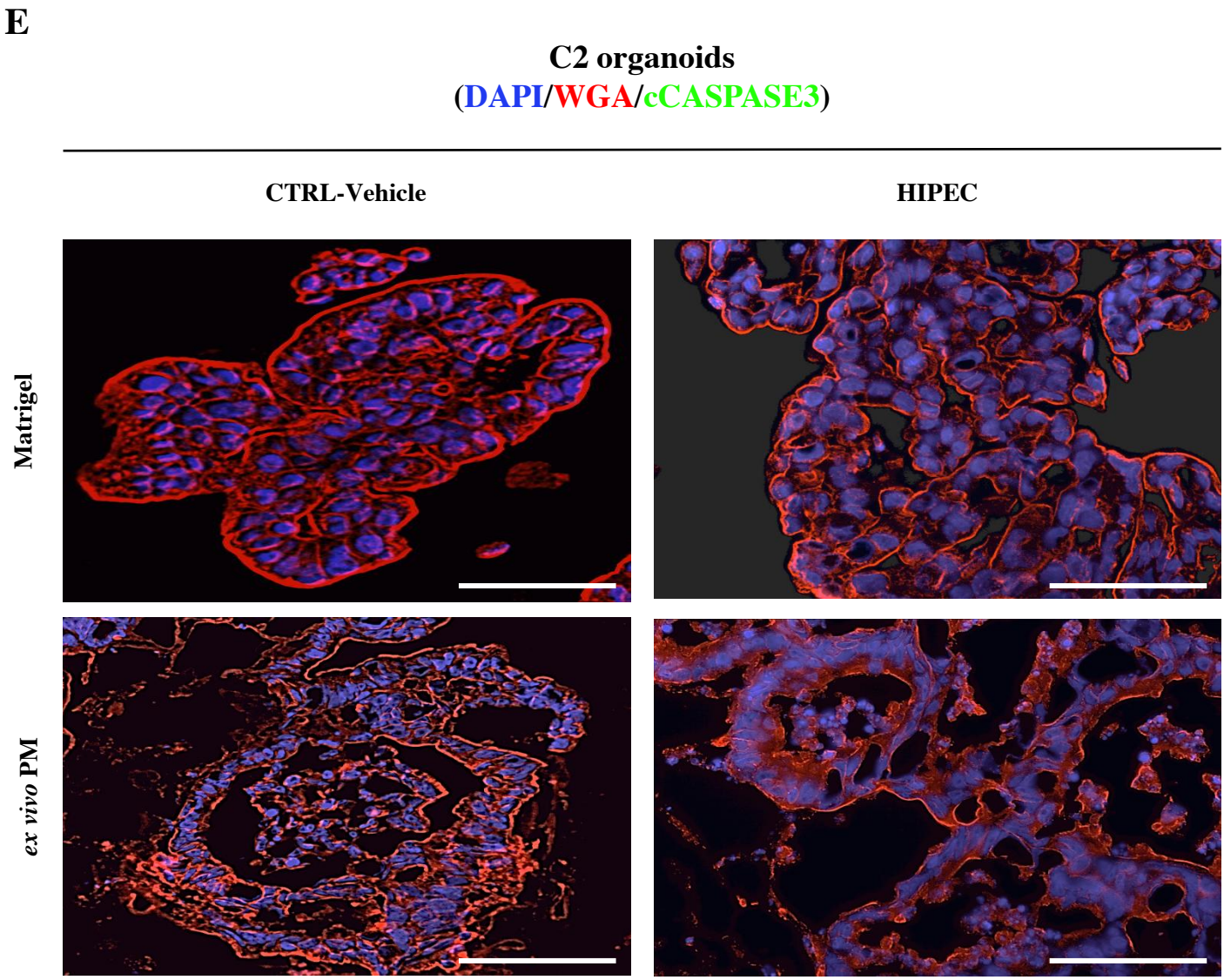

Supplementary Fig. S6 (E) IF analysis of C2 PM-derived organoids cultured in Matrigel and on neoplastic-derived peritoneal 3D-dECMs after *in vitro* HIPEC treatments, using cCASPASE3 (green) antibody. The samples were counterstained with WGA (red) and DAPI (blue). Scale bar: 50 µm.

F

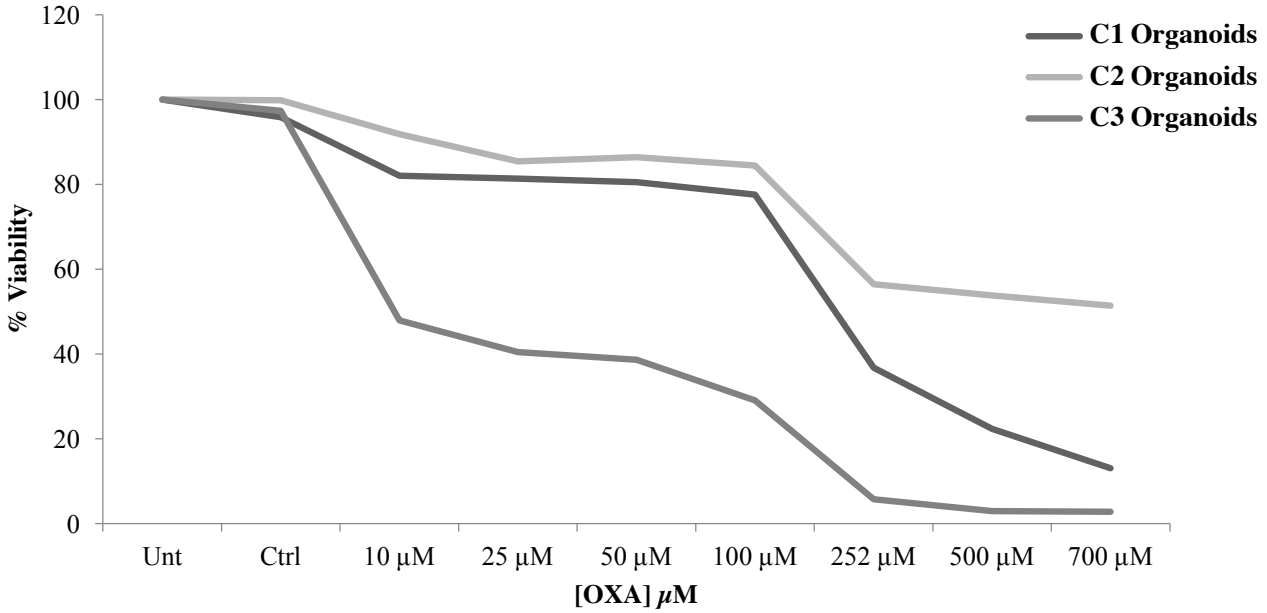

G

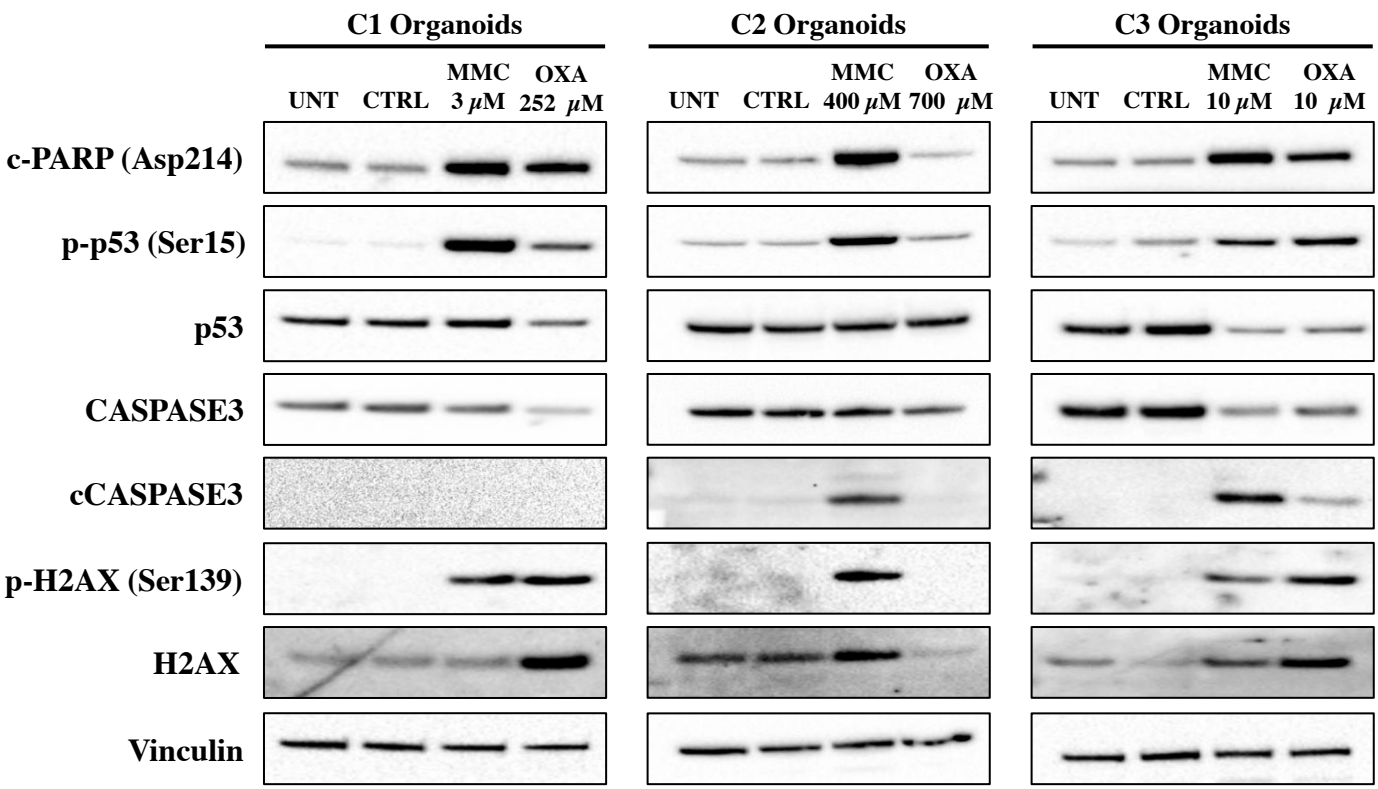

Supplementary Fig. S6. (**F**) Dose response curve of C1, C2 and C3 PM-derived organoids cultured in Matrigel and treated with OXA at different concentrations at 42.5 °C for 90 min. **(G)** Immunoblots of cPARP, p-p53, p53, CASPASE3, cCASPASE3, p-H2AX and H2AX in C1, C2 and C3 PM-derived organoids treated with MMC and OXA at the respective IC_{50} concentrations. Vinculin was used as loading control. Ki-67 immunostaining of C2 PM-derived organoids cultured in Matrigel and on neoplastic-derived peritoneal 3D-dECMs after *in vitro* HIPEC treatments.

H

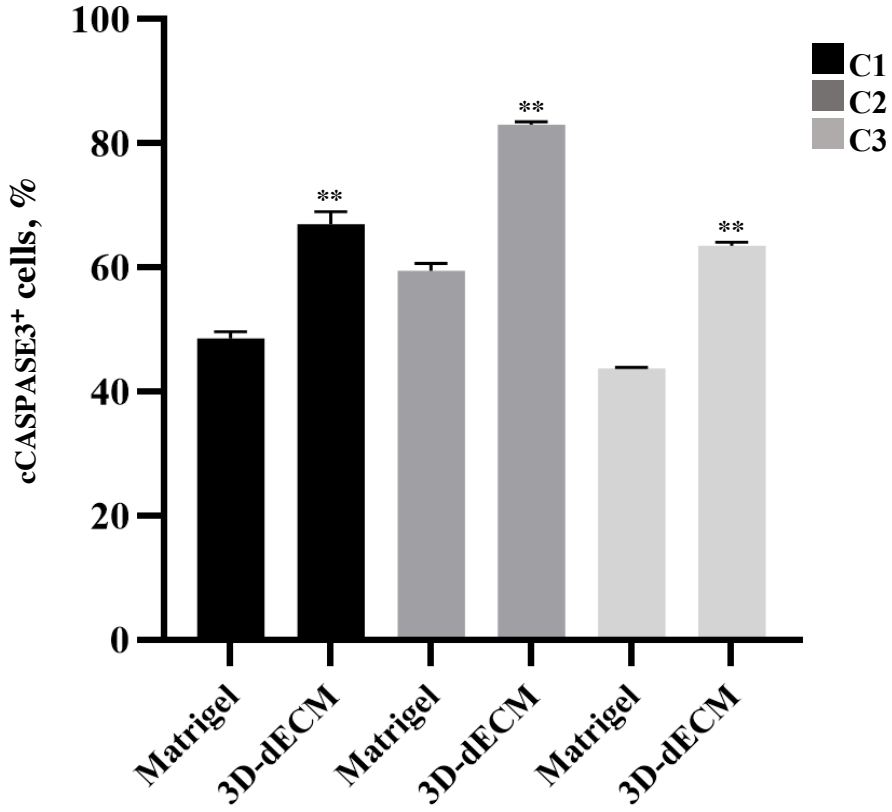

Supplementary Fig. S6. (**H**) Percentage of apoptotic TDO treated with OXA, measured as the percentage of cCASPASE-3^+ cells present in selected fields. Five fields per experiment (40X magnification) were counted. Data are presented as median and SD . One-way ANOVA (**p<0.01).